# Extending the search for cosmic point sources of neutrinos with IceCube beyond PeV energies and above the horizon

DISSERTATION

zur Erlangung des akademischen Grades

doctor rerum naturalium
(Dr. rer. nat.)
im Fach Physik

eingereicht an der
Mathematisch-Naturwissenschaftlichen Fakultät I
Humboldt-Universität zu Berlin

von
**Dipl.-Phys. Robert Johannes Lauer**
geboren am 01.10.1981 in Aachen

Präsident der Humboldt-Universität zu Berlin:
Prof. Dr. Dr. h.c. Christoph Markschies

Dekan der Mathematisch-Naturwissenschaftlichen Fakultät I:
Prof. Dr. Lutz-Helmut Schön

Gutachter:
1. Dr. Elisa Bernardini
2. Prof. Dr. Hermann Kolanoski
3. Prof. Dr. Thomas K. Gaisser

eingereicht am: 15.01.2010
Tag der mündlichen Prüfung: 15.04.2010

## Abstract

Neutrinos are expected to be produced in hadronic interactions in the environment of astrophysical particle accelerators. Searching for point-like neutrino signals provides a chance of identifying such sites as sources of cosmic rays. An established approach to realise high energy neutrino astronomy is the observation of Cherenkov radiation from induced muon tracks in subsurface detectors. The IceCube Observatory is currently the largest of these neutrino telescopes. Presented here is an analysis based on data taken with IceCube between 2007 and 2008 in its preliminary configuration of 22 strings.

Neutrino point source searches had been so far restricted to one hemisphere, due to the exclusive selection of upward going events as a way of rejecting the atmospheric muon background. This work demonstrates that the region above the horizon can be included by suppressing the background through an energy-sensitive event selection. The approach improves the sensitivity above PeV energies, previously not accessible at all for declinations of more than a few degrees below the horizon due to the absorption of neutrinos in Earth.

A scan of both celestial hemispheres was performed in this work to identify neutrino fluxes via excesses of events in individual directions. For a separate test, a list of specific neutrino source candidates was compiled, based on model predictions for Active Galactic Nuclei. In an additional study, data on variable photon fluxes from the blazar 3C279 were used to define a time-dependent search for short neutrino flares. No significant excesses above the atmospheric background were found in any of the analysis parts. The resulting upper limits on neutrino fluxes are the first that cover point sources in the southern sky up to the EeV energy range. For certain source candidates, these limits provide the best constraints on models predicting neutrinos above PeV energies.

Based on the same event sample, a search for correlations between neutrinos and the most energetic charged cosmic rays was performed. The arrival directions of air showers with energies of tens of EeV, reported by the HiRes experiment and the Pierre Auger Observatory, were used to count coincidences with IceCube data. The result of this study is again compatible with the background hypothesis.

**Keywords:**
neutrinos, point sources, IceCube, cosmic rays

## Zusammenfassung

In Modellen astrophysikalischer Teilchenbeschleuniger werden Neutrinoemissionen vorhergesagt. Die Suche nach Neutrino-Punktquellen bietet eine Möglichkeit, solche Orte als Quellen der Kosmischen Strahlung zu identifizieren. Eine etablierte Methode in der Neutrinoastronomie ist die Messung der Cherenkov-Strahlung induzierter Myonen in unterirdischen Detektoren. Das IceCube-Observatorium ist zur Zeit das größte Neutrinoteleskop dieser Art. Die hier vorgestellte Analyse basiert auf Daten, die mit IceCube in der Konfiguration von 22 Trossen zwischen 2007 und 2008 gesammelt wurden.

Bisherige Neutrino-Punktquellensuchen waren auf eine Hemisphäre beschränkt gewesen, da nur aufwärts laufende Ereignisse betrachtet wurden, um den atmosphärischen Myon-Untergrund zu eliminieren. Hier wird gezeigt, dass der Bereich über dem Horizont durch eine energieabhängige Selektion miteinbezogen werden kann. Dies erhöht die Sensitivität für Energien oberhalb einiger PeV, die bisher aufgrund von Neutrinoabsorption ab einigen Grad unterhalb des Horizonts vollkommen unzugänglich waren.

Zum Nachweis von Neutrinosignalen durch richtungsabhängige Ereignisüberschüsse wurde eine Musterung beider Himmelshälften durchgeführt. Für einen separaten Test wurde eine Liste von Quellkandidaten anhand von Modellvorhersagen für Aktive Galaktische Kerne erstellt. Außerdem dienten Daten über den Blazar 3C279 als Grundlage für eine zeitabhängige Suche nach kurzen Neutrinoemissionen. Es konnten keine signifikanten Ereignisüberschüsse über dem Untergrund beobachtet werden. Daraus leiten sich die ersten oberen Neutrino-Flussgrenzen für Punktquellen am Südhimmel bei Energien bis in den EeV Bereich ab. Für bestimmte Quellkandidaten sind es die besten Einschränkungen für Neutrinovorhersagen bei PeV Energien.

Mit den gleichen Ereignissen wurde eine Suche nach Korrelationen zwischen Neutrinos und den höchstenergetischen geladenen Teilchen der Kosmischen Strahlung durchgeführt. Die Ursprungsrichtungen von Luftschauern, veröffentlicht durch das HiRes Experiment und das Pierre Auger Observatorium, wurden zur Bestimmung von Koinzidenzen mit IceCube-Ereignissen benutzt. Das Ergebnis ist im Einklang mit den Untergrunderwartungen.

**Schlagwörter:**
Neutrinos, Punktquellen, IceCube, Kosmische Strahlung

# Contents

# Chapter 1.

# Introduction

Past and present endeavours in astronomy are continuing to highlight the enormous diversity of cosmic phenomena and lead to the discovery of new and unforeseen astrophysical processes. Such observations have often given rise to questions about their explanations and thus inspired whole new areas of research, the quest for dark energy being a recent example. These interplays between astronomy and research in fundamental physics have been very fruitful in the past. They paved the way for a deeper understanding of the fundamental physical laws and forces behind the structures in the universe. This search for knowledge in the depths of space is a basic motivation for continuously improving and extending astronomical efforts.

Until recently, nearly all the insights into astrophysical objects and processes have been obtained based on the observation of photons. Astronomy has profited from, and itself inspired, many advancements in photon detection. Instruments are stationed on ground or in space and cover a spectral range from radio waves to gamma-rays.

Now, after a century of unravelling the physics of elementary particles and their interactions, another cosmic messenger becomes available: the neutrino. Neutrino astronomy currently knows only two extra-terrestrial sources, the sun and, flaring for a short time, supernova 1987A. The pioneering experimental work behind these discoveries has been recognised with the Nobel Prize in 2002.

With the exception of another nearby supernova, any other astrophysical neutrino source is expected to be very faint. Only by looking at very high energies above $10^{12}$ eV (1 TeV), where the background flux of particles produced in the atmosphere is low, can one expect to observe new neutrino emitters.

Searches for neutrino signals with point-like origins are a particularly promising way to identify the origins of the enigmatic cosmic rays at the highest energies. The study of this astrophysical particle flux over the last century has uncovered a spectrum of ionised nuclei that extends beyond $10^{20}$ eV, but the sources remain unknown. At the moment, some of the best hints for solving this puzzle come from gamma-ray astronomy, probing the sky at GeV to TeV energies and providing us with images of various types of cosmic accelerators. Nevertheless, it seems that for an unambiguous identification of sources of hadronic cosmic rays it is required to combine the results from different observation channels. A complementary approach, not only at various photon wavelengths but with multiple messengers will be necessary to judge which of the proposed models actually describe the most energetic processes in the Universe.

Astrophysical high energy neutrinos can provide substantially new information in cosmic ray research, since they are a clear indication of hadronic decays. Compared to protons or other ionised nuclei, they are not deflected on their way to Earth by magnetic fields. And while for example photons at PeV energies interact with the cosmic microwave background in $e^+e^-$ pair production processes, neutrinos suffer basically no absorption in astrophysical environments. Thus, neutrinos even allow to probe the inside of regions opaque to photons and sources up to large cosmic distances, opening new horizons.

In the search for high energy neutrino sources, the so-called *next generation neutrino telescopes* have begun to take data. They are based on the optical Cherenkov detection technique that allows observing neutrino-induced charged leptons and reconstructing their arrival directions. Improvements over the first pioneering experiments are primarily achieved by making things bigger: IceCube, the largest neutrino telescope to date, has an instrumented volume of 1 km$^3$ when completed, approximately 60 times that of its predecessor AMANDA. The resulting increase in event rates is crucial for the detection of faint neutrino signals.

One also aims to extend the accessible energy range to obtain a more comprehensive picture of the neutrino sky. In this respect, the work presented here introduces a new methodology for neutrino point source searches. By including events coming from above the horizon, a previously excluded region of increased background fluxes, a search can cover higher energies up to about an EeV. The new approach also overcomes the past limitation of observing only half of the sky.

This thesis gives a full account of the steps taken to perform such an analysis, based on data collected with the IceCube Observatory in its preliminary configuration operating from May 2007 to April 2008. The results provide new information and constraints for the discussion of astrophysical source scenarios for neutrinos and the relation to charged cosmic rays.

Chapter 2 provides a brief overview of the status of cosmic ray studies and the expectations for neutrino emission in astrophysical environments. Active Galactic Nuclei are introduced as a promising potential source class. The adjacent chapter discusses neutrino propagation and interactions and the techniques to detect them via the optical channel. This is followed by a description of the IceCube Observatory, its detection medium, geometry and framework for performing a neutrino analysis. In chapter 5, the methods and algorithms for reconstructing neutrino events in IceCube are explained, focusing on the directions of induced muon tracks. This includes a discussion of the performance with respect to angular resolution, a critical parameter in point source searches. Of fundamental importance in any neutrino analysis is the background suppression. Chapter 6 gives a detailed account of the selection of events from above and below the horizon for a unified point source search in both hemispheres, which has never before been realised.

The search methods and their application to the sample of neutrino candidates are the topic of chapter 7. In this context, the discussion on Active Galactic Nuclei is continued, leading to a theoretically motivated selection of individual source candidates for dedicated tests of their neutrino emissions. Chapter 8 provides the results from these point source searches. After accounting for the systematic uncertainties, the new flux limits are discussed in relation to neutrino source models. A search for directional correlations between the neutrino candidates from this analysis and data on charged cosmic rays at ultra-high energies is introduced in chapter 9. This is the first study of this kind performed on large event samples from neutrino telescopes and air shower detectors. The thesis concludes with a summary and outlook on high energy neutrino point source searches below and above the horizon.

# Chapter 2.

# High energy neutrino astrophysics

This introductory chapter provides an overview of the motivations and expectations for the search for high energy neutrinos from cosmic sources. Observations of charged cosmic rays and the question of their origin are introduced as the basic incentive for neutrino point source searches. Experimental results and general models of astrophysical particle acceleration and interaction are also summarised. The second part of this chapter focuses on Active Galactic Nuclei as promising source candidates and possible scenarios of neutrino emission from them.

## 2.1. Cosmic rays

### 2.1.1. Charged particle spectrum

Since the discovery of increasing ionising radiation with rising altitude above the ground by Victor Hess [Hes12], the flux of particles called *cosmic rays* has been studied in detail over an enormous range of energies. An overview of the spectrum is presented in Fig. 2.1 illustrating the power law characteristics of the differential flux $dN/dE \propto E^{\gamma}$, falling steeply as a function of energy. Due to this behaviour it is only possible in the lower energy part of the spectrum to detect the primary particles directly with experiments on satellites or balloons, by which means the flux rate and composition of cosmic rays has been successfully probed up to approximately one PeV ($10^{15}$ eV). The flux is composed of ionised atomic nuclei with relative amounts similar to those found in the solar system, but accelerated to very high energies. At energies above $\sim 100$ TeV ($10^{14}$ eV), the flux is reduced too much to be observable with experiments above the atmosphere and indirect methods have to be used. These rely on the detection of extensive air showers, initiated by cosmic rays interacting in the atmosphere. For a review of measurements and analysis techniques see [HRR03].

The overall spectrum appears featureless, but detailed fits reveal localised changes in the spectral shape. The so-called *knee*, see Fig. 2.1, is a kink at an energy of several PeV, where the power law index steepens from $\gamma \approx -2.7$ to $\gamma \approx -3.1$.

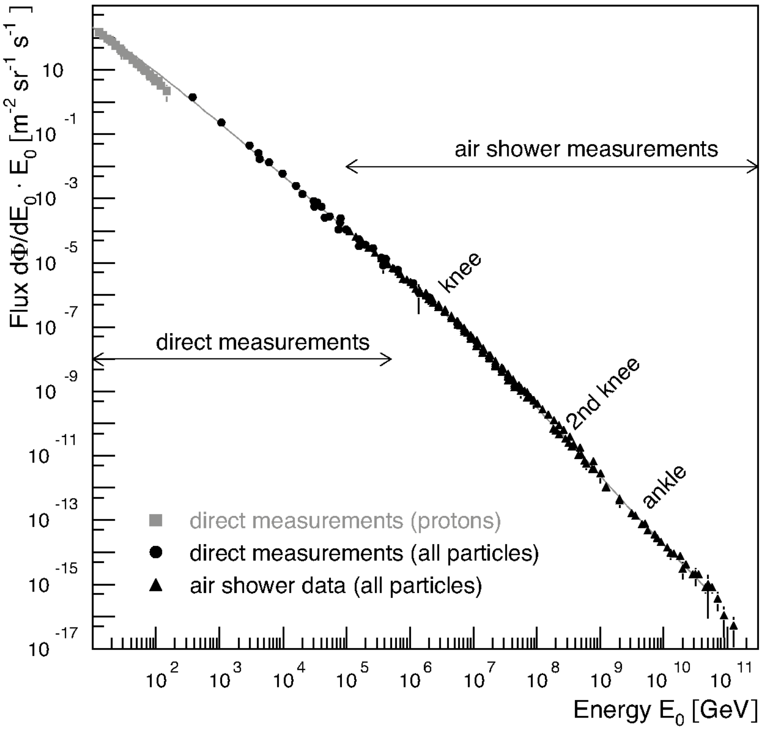

Figure 2.1.: All-particle energy spectrum of cosmic rays, measured directly with detectors above the atmosphere and indirectly with air shower experiments. Plot taken from [BEH09].

A further steepening at the *second knee* and a flattening at the *ankle* are also observed. Recent experimental results for energies above that of the knee and possible explanations on the nature of these features are reviewed in [BEH09]. In most theories it is assumed that a reduced contribution of cosmic rays produced inside the galaxy is a major reason for the changes starting at the knee. Proposed reasons are the limitations of acceleration processes and an increased escape rate. The ankle could indicate the changeover to a flux dominated by extra-galactic cosmic rays.

At the highest particle energies above $6 \times 10^{19}$ eV, a suppression of the flux compared to power law extrapolations has been observed by air shower experiments [A$^+$08a, A$^+$08e]. This can be interpreted as the onset of efficient interactions of cosmic rays with photons from the cosmic microwave background, termed *Greisen-Zatsepin-Kuzmin* (GZK) cut-off after authors who first discussed this effect in [Gre66, ZK66]. The few detected events from particles at these highest energies might be only slightly effected by galactic magnetic fields, so that their arrival directions point to the source regions. This possibility and the relevant observations are discussed in chapter 9.

There exists wide agreement that the origin of cosmic rays up to PeV energies can be mostly attributed to electro-magnetic acceleration processes in certain environments inside our galaxy, some details of which are discussed in the following sections. For part of the spectrum at greater energies up to the highest measured values around $10^{20}$ eV, explanations are separated into top-down and bottom-up approaches. The former comprise theories with a wide variety of super-heavy exotic particles that decay into cosmic rays of highest energies, an overview can be found for example in [BS00]. Limits on photon fluxes at similarly high energy, compiled in [A$^{+}$08f], strongly disfavour these top-down scenarios and they are not discussed further in this work, since they would not be observable as neutrino point sources.

The bottom-up explanations postulate extra-galactic objects with acceleration processes that are based on the same principles as those expected for cosmic ray production inside our galaxy, but leading to much higher particle energies. The basic physics behind such scenarios and the possible source candidates are reviewed in the following sections. Neutrinos at very high energies, produced as secondaries in interactions of charged cosmic rays near their sources, would be an ideal observation channel to identify and study these origins. The relevant models and predictions are the focus of the rest of this chapter.

## 2.1.2. Astrophysical particle acceleration

### Fermi acceleration

A central idea for cosmic ray acceleration in astrophysical environments was introduced by Fermi in [Fer49]. One assumes a particle encounters a region of moving plasma in the interstellar medium and enters it with the initial energy $E_0$. Through collisionless scattering on magnetic field inhomogeneities inside this region, stochastic changes of the direction of the particle occur until it leaves the region again. Due to the velocity $v$ of the moving environment, there is a gain in the energy of the particle $\Delta E = \xi E_0$. In certain configurations, this only appears as a net gain after several such encounters, $E_n = E_0(1+\xi)^n$. It is shown in [Gai90], following the derivation in [Bel78], that this acceleration model in general leads to a power law spectrum, with the number of particles $N$ with energies larger than $E$ determined by the proportionality:

$$N(\geq E) \propto \frac{1}{P_{\mathrm{esc}}} \left( \frac{E}{E_0} \right)^{-\alpha} \quad \text{with } \alpha \approx \frac{P_{\mathrm{esc}}}{\xi}. \tag{2.1}$$

$P_{\mathrm{esc}}$ is the probability for escape from the region of moving inhomogeneities in each encounter. The spectral index $\alpha$ also depends on this probability and thus on the ratio between the time for one cycle and that of the average time before escape, which could be the limited lifetime of the accelerating systems.

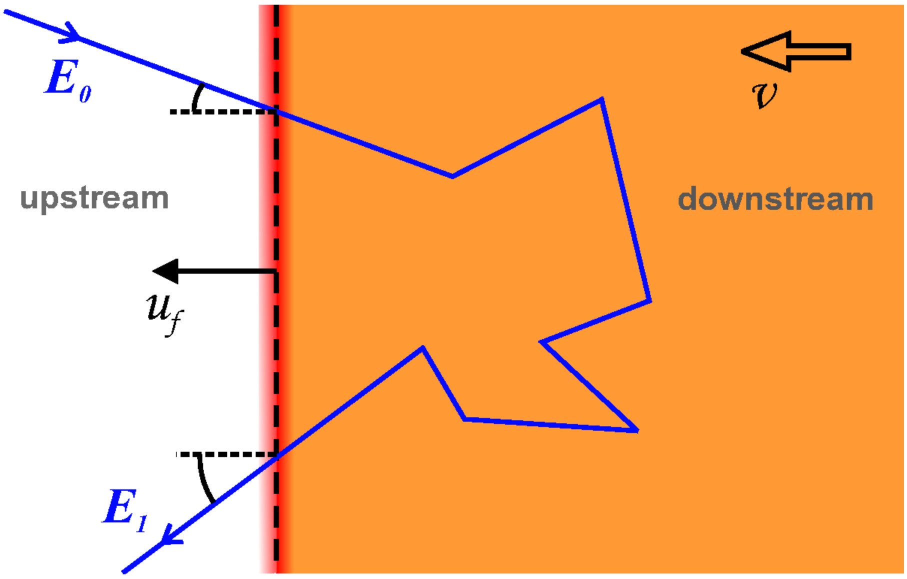

Figure 2.2.: Schematic view of first order Fermi acceleration at a plane shock front for one encounter.

In the original publication, Fermi considered moving clouds of plasma as accelerators. Particles can enter and leave these on any side. The resulting average energy gain is proportional to the square of the cloud's velocity as a fraction of the speed of light $c$, $\xi \propto (v/c)^2$, and thus called *second order Fermi acceleration*. A more efficient setup is that of a shock front moving at several times the speed of sound in the medium. If its extension is large compared to the typical cycle length of a particle, given by its gyroradius in the magnetic field of the medium, the shock front can be approximated as a plane as illustrated in Fig. 2.2. Particles are scattered on magnetic inhomogeneities on both sides of the front and can only escape from this acceleration environment on the *downstream* side with a probability $P_{\text{esc}} = 4u_d/c$, where $u_d = u_f - v$ is the difference between the (non-relativistic) velocity of the shock front $u_f$ and that of the shocked gas $v$. Following the calculation in [Gai90] and averaging over all injection and ejection angles of particles from the *upstream* region, their relative energy gain per encounter depends only on $v$:

$$\frac{\Delta E}{E_0} = \xi \approx \frac{4}{3}\frac{v}{c} \; . \tag{2.2}$$

This is called *first order Fermi acceleration* due to its linearity.

Inserting these approximations for an infinite plane shock into equation (2.1) yields the spectral index:

$$\alpha = \frac{3}{u_f/u_d - 1} \approx 1 + 4\frac{c_s}{u_f} \; . \tag{2.3}$$

The final approximation here is based on kinetic gas theory and valid for velocities $u_f$ that are at least several times as large as the sound speed $c_s$ in the plasma. With these considerations, the stochastic shock acceleration leads to a spectral index $\gamma = -\alpha - 1 \approx -2$ for the differential energy spectrum $dN/dE$ of cosmic rays. Since this value for the source region is steepened due to leakage of higher energy particles from the galaxy, it can naturally explain the observed value of 2.7 at energies below the knee.

#### Acceleration power

Prime candidates for the origin of shock acceleration processes in our galaxy are supernova remnants. As has been first discussed in [GS64], the energy output from supernovae well fits the power needed to replenish losses from cosmic rays escaping from the galactic disk. The required acceleration efficiency is not larger than $\sim 10\%$. The maximum energy of particles with charge number $Z$ for this scenario has been estimated in [LC83] to be around $E_{\text{max}} \leq Z \times 3 \times 10^4$ GeV, and in a more recent calculation to a larger value of $Z \times 5 \times 10^5$ GeV [Ber96].

The mechanism of shock acceleration can also lead to much higher particle energies. Prerequisites are for example larger magnetic fields, compared to a few $\mu$G for galactic supernovae environments, or much longer acceleration times, compared to $\sim 10^3$ years for supernovae. Extra-galactic environments could feature such extreme shock processes that would lead to the production of cosmic rays up to the highest energies observed.

### 2.1.3. Astrophysical neutrino production

Systems where cosmic ray protons or nuclei are produced are expected to emit also other high energy particles. These emerge as secondaries from interactions of the primary hadrons with the surrounding medium. If the matter density in a source region is relatively high, a beam dump in a particle accelerator is a good analogy for the interaction scenario, especially since astrophysical acceleration processes might be limited to a certain opening angle, for example in plasma jets. In such a configuration, the dominant proton-proton ($pp$) channels are:

$$p + p \rightarrow \left\{ \begin{array}{c} \pi^0 + 2p \\ \pi^+ + n + p \end{array} \right. . \tag{2.4}$$

For source candidates larger than the stellar scale, low matter densities might prohibit efficient $pp$ interactions. In this case, photons, either co-produced in acceleration processes or from external, for example stellar, photon fields, are also possible targets for protons. The $\Delta$-resonance is then the main $p\gamma$ interaction channel:

$$p + \gamma \rightarrow \Delta^+ \rightarrow \left\{ \begin{array}{c} \pi^+ + n \\ \pi^0 + p \end{array} \right. . \tag{2.5}$$

In both interaction scenarios, the corresponding processes with neutrons as incident particles also lead to the formation of $\pi^-$ mesons. A production of heavier mesons like $K^\pm$ and $K^0$ is possible, but occurs only at very high energies and is thus negligible compared to the pion channels.

In basically all astrophysical environments, pions decay before they can interact with other particles and in this way produce leptons and photons:

$$\begin{array}{ccccc} \pi^+ & \rightarrow & \mu^+ + \nu_\mu & \rightarrow & e^+ + \nu_e + \bar{\nu}_\mu + \nu_\mu \\ \pi^- & \rightarrow & \mu^- + \bar{\nu}_\mu & \rightarrow & e^- + \bar{\nu}_e + \nu_\mu + \bar{\nu}_\mu \\ \pi^0 & \rightarrow & \gamma\gamma\ . & & \end{array} \tag{2.6}$$

Under the assumption that positively and negatively charged pions occur in equal amounts the decay chains directly yield the flavour ratio of neutrinos at the site of origin:[1]

$$\nu_e : \nu_\mu : \nu_\tau = \bar{\nu}_e : \bar{\nu}_\mu : \bar{\nu}_\tau = 1 : 2 : 0\ . \tag{2.7}$$

Assuming that neutral pions occur as often as both of the charged types, a calculation of relative energy distribution between the particles was worked out for example in [Sta04]. The equal partition of energy between the final products in each of the three decay chains leads to approximately the same amount of energy deposited in electromagnetic particles as in neutrinos. The precise photon to neutrino ratio depends on the details of the interaction setup, but the general correlation suggests that promising neutrino sources are also bright photon emitters. This makes it possible to use gamma-ray measurements to identify neutrino source candidates, as discussed in chapter 7.

The resulting energy spectra of photons and neutrinos are still likely to exhibit different shapes. On the one hand, there are more neutrinos generated per pion than photons or electrons. Consequently, neutrino distributions are shifted to slightly lower energies. On the other hand, photons and in particular electrons are strongly affected by further interactions and absorption and thus often exhibit a softened spectrum compared that of the initial hadronic processes. Astrophysical neutrinos carry this original energy signature since they usually leave the sources without interference. The assumed underlying proton energy distribution is therefore a reasonable benchmark for expectations on neutrino spectra, yielding a power law $dN/dE \propto E^\gamma$ with $\gamma \approx -2$ as discussed in section 2.1.2. However, the distributions and spectra of target photons or nucleons can still change the details of the spectral shape of neutrino fluxes, producing cut-offs and softer or harder spectral indices.

---

[1] Based on this symmetrical situation for particles and anti-particles, no differentiation between the two types is being made for discussing source scenarios in this work.

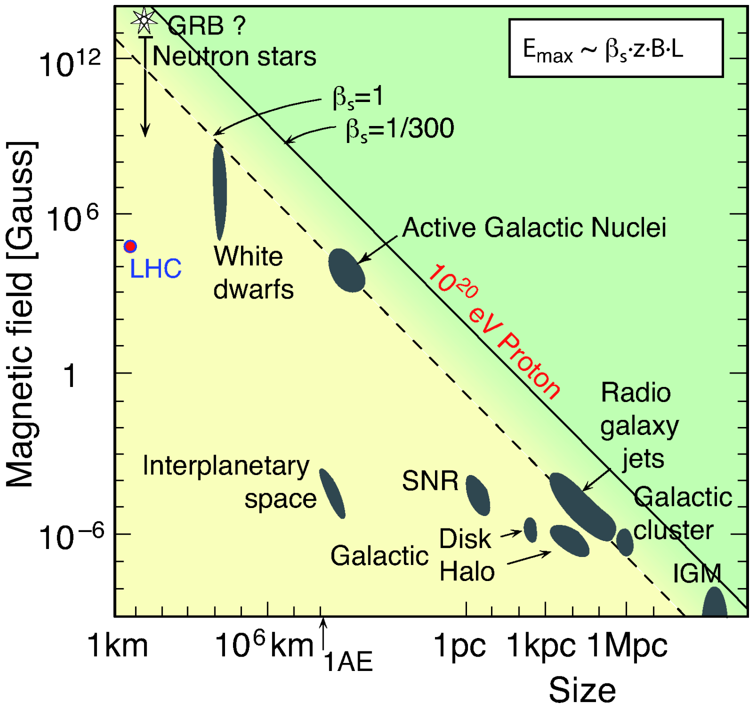

Figure 2.3.: Hillas plot, showing the relation between size and magnetic field strength for astrophysical objects in which cosmic rays could be accelerated. Plot taken from [BEH09].

## 2.1.4. Galactic and extra-galactic source candidates

As well as supernovae remnants, there are several other galactic objects that are of interest as potential cosmic ray sources, see for example [Bec08]. Rotating neutron stars that are observed as pulsars form a class of prominent candidates, primarily because they have very strong magnetic fields on the order of $10^{12}$ G. Other possible sources are binary systems that contain a neutron star or a black hole as one of the stellar partners. X-ray emissions from such constellations hint at non-thermal acceleration processes. A particular subclass of such binaries are microquasars, defined by their visible jets, an overview is given in [Mir07].

In general, the inherent magnetic field strength in a source limits the maximum energy to which particles can be accelerated. If the gyroradius exceeds the extension of the object the particles escape, leading to an energy cut-off. This relation was presented in [Hil84] and is shown in the diagram in Fig. 2.3, called Hillas plot. It demonstrates that the cosmic rays with the highest observed energies of up to $10^{20}$ eV are likely to originate from extra-galactic objects. In particular, Active Galactic Nuclei (AGN) with super-massive black holes as central engines and their kilo-parsec scale jets, the basis for a classification as radio galaxies, are prime candidates, discussed in the following section.

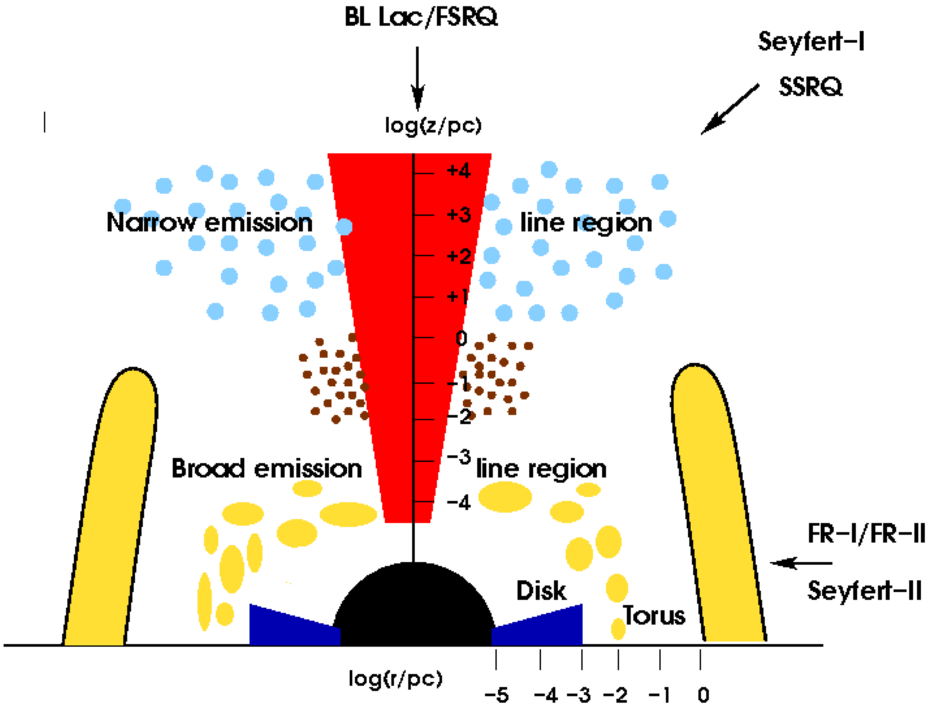

Figure 2.4.: Scheme of the generic, cylindrically symmetric AGN structure in the r-z-plane. Both axes are logarithmic and show length scaled to 1 pc. Different classifications in dependence of the viewing angle are indicated, with more details given in [ZB02]. Plot taken from [Bec08]

Gamma-ray bursts (GRB) might also feature the conditions for cosmic ray acceleration to the highest energies. For details on models of neutrino emission see for example [Bec08]. Due to their transient nature with gamma-ray flux periods on the order of seconds up to minutes, GRBs require different approaches than the search method for steady neutrino sources presented in this thesis. For this reason, GRBs are not discussed here, but recent neutrino flux limits can be found in [A$^+$10a, A$^+$09e].

## 2.2. Neutrinos from Active Galactic Nuclei

### 2.2.1. Generic AGN model

The structure and components that define the generic class of AGN are shown schematically in Fig. 2.4. A rotating super-massive black hole with a mass $M > 10^8 M_\odot$ forms the centre and is surrounded by an accretion disk. This nucleus is embedded in a host galaxy, separated by a dust torus which feeds the accretion disk. Two jets emerge upward and downward along the symmetry axis perpendicular to the disk and transport matter at relativistic velocities through lobes extending over kilo-parsecs and are the source of radio emission. These jets are believed to be formed by magnetic fields near the central black hole, powered by its rotation.

This axisymmetric model was used in [UP95] to describe a unified picture of active galaxies featuring various observational signatures in dependence of the inclination angles under which they are viewed. Apart from the appearance of the jets themselves, such signatures stem for example from regions of broad and narrow emission lines produced in different environments along the jet. Also the accretion disk can be obscured by the torus or visible as a bright source of optical radiation. These and other aspects are the basis of a detailed classification of AGN, originally developed before the unified picture emerged. A good overview over these types is provided in [A$^+$06a], adopting a threefold distinction scheme based on the host galaxy, the luminosity and the inclination angle.

## 2.2.2. Blazars

### Morphology

Concerning high energy neutrino production in AGN, theoretical and observational interest concentrates on a sub class of objects called *blazars*. A blazar is characterised by its orientation with the symmetry axis pointing towards the observer. In consequence, the jet itself has only a small apparent length, if it can be identified at all as an extended structure. The relativistic flow of plasma accumulations, so-called knots, inside the jet leads to apparently superluminal motion from the point of view of the observer. This signature makes it possible to identify blazars, see [Sta04] for details. The moving knots inside the magnetically contained plasma provide a promising setup for effective shock acceleration as introduced in section 2.1.2. Furthermore, the emitted particles would be strongly boosted by the relativistic motion of the plasma with typical Lorentz factors $\Gamma \sim 10$, increasing the observed luminosity.

Blazars are subdivided into two classes based on their radio luminosity. A higher luminosity object with a small opening angle between jet and line of sight is called *Flat Spectrum Radio Quasar* (FSRQ). The name refers to the dominating radio spectrum from the inner, boosted part of the jet which is flatter than that from the outer lobes, see [A$^+$06a] and references therein for details. Blazars with lower luminosities are classified as *BL Lac objects*, named after the first such galaxy that was regarded as a separate type.

### Spectral energy distribution

Blazars have been studied extensively with photon data at various wavelengths, so-called *multi-wavelength* observations. Based on measurements reaching from the radio to the gamma-ray regime, a generic behaviour of spectral energy distri-

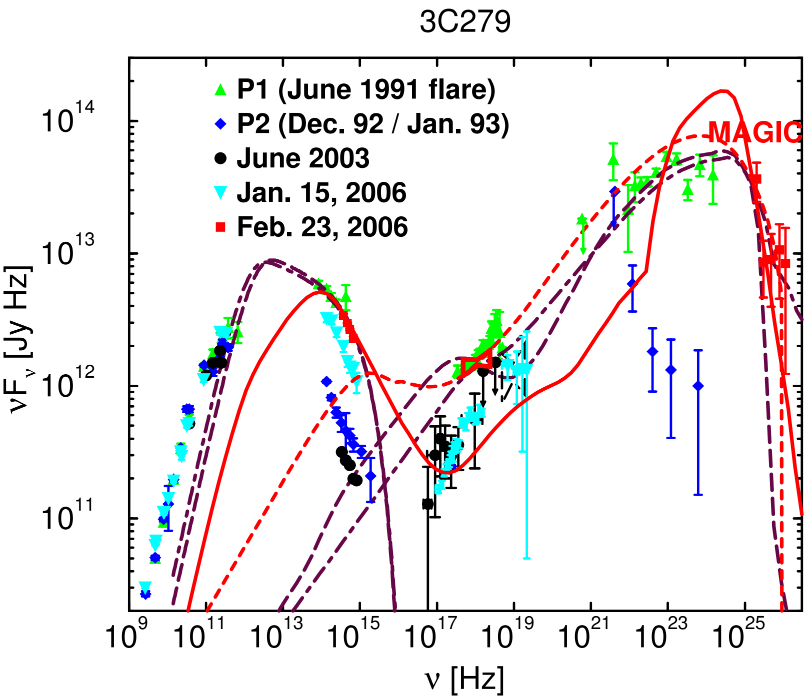

Figure 2.5.: The SED of the blazar 3C279 as an example for the two-peak structure. Data points are based on measurements at various dates from different experiments, with those at highest energies from Magic [A$^+$08h]. The red lines are fits based on leptonic models, the moron lines are related to hadronic acceleration scenarios. The plot stems from [BRM09], where details of measurements and fits are discussed.

butions (SEDs) for this class of objects was shown and discussed in [FMC$^+$98]. Irrespective of certain characteristic differences between FSRQs and BL Lac objects, AGN from both classes were used to derive average empirical SEDs for blazars. These spectra feature a typical structure of two peaks, one at lower photon frequencies up to the X-ray regime and one in the higher energy part. The latter extends into the gamma-ray range and can be studied by satellite experiments or, at TeV energies, with *Imaging Air Cherenkov Telescopes* (IACTs) like Hess [Hin04], Magic [Fer05] or Veritas [W$^+$02]. Figure 2.5 shows the example of the FSRQ 3C279, discussed in section 7.3.

The statistical analysis revealed that the two peak positions are correlated and both shift to higher frequencies for decreasing total luminosities of the objects. Furthermore, the luminosity ratio between the high and low energy component changes from a dominance of the former towards equal amplitudes for peaks at higher frequencies.

The lower peak is supposed to stem from synchrotron radiation from accelerated electrons. A classification originating from [PG95] divides BL Lac objects into two classes, *Low Peaked BL Lac objects* (LBL) with a synchrotron maximum in the low to high infra-red (IR) range and *High Peaked BL Lac objects* (HBL) with this peak at ultra-violet (UV) to low X-ray frequencies. A detailed modelling of individual blazar spectra in [GCF$^+$98] extends this ansatz to provide a full explanation of the SED shape. It is based on a scenario of accelerated electrons, which not only produce the synchrotron radiation in the first peak, but also up-scatter these synchrotron photons via the inverse Compton effect and thus generate the second peak. This picture is abbreviated as *Synchrotron Self-Compton (SSC)* model.

It can explain the data from many multi-wavelengths observations of blazars, but it would suggest that the major part of the energy emitted by such AGN is not connected to the acceleration of particles other than electrons. This explanation severely limits their potential as cosmic ray or neutrino sources. In contrast to this *leptonic acceleration* scenario, the following section provides examples for alternative AGN models that account also for *hadronic acceleration* of protons or heavier nuclei, thus providing a framework for the production of neutrinos.

## 2.2.3. Neutrino production

### Hadronic acceleration

The synchrotron emission from accelerated electrons is widely accepted as the explanation for the peak at lower frequencies in generic blazar spectra. However, there is no consensus on the question of wether the higher energy peak is also generally dominated by the contributions from leptonic processes. Hadronic acceleration could play a major role and models accounting for this produce good fits to the photon SEDs. Often though, they are more dependent on properties of the environment of the host galaxy, for example radiation fields. The reason is that the interactions that produce gamma-rays and neutrinos via pion decay require a target medium, in contrast to the closed system of SSC models. This dependence is reflected in the fact that a large variety of model approaches focuses on neutrino production in individual sources.

Here it is not possible to provide a comprehensive overview over all scenarios, hence only a few general models are presented in the following. Some details on individual source predictions are discussed in the context of selecting promising candidate objects in chapter 7 and the interpretation of the neutrino point source search results in chapter 8.

### Neutrinos from AGN cores

In a generic AGN, the regions considered for hadronic interaction processes stretch from the very core near the accretion disk up to the outer lobes of the plasma jets. In case of models that focus on the core, the first calculations of individual and diffuse neutrino emissions from AGN were presented in [SDSS91][2]. There it is assumed that protons are accelerated in accretion shocks of matter falling into the black hole as described in [KE86]. UV photons, stemming from a characteristic thermal disk radiation observed in many AGN, serve as seeds for $p\gamma$ interactions which lead to neutrinos according to equation (2.6).

Other models assume beamed hadronic acceleration in the emerging jets, still inside the core region. There, matter densities might be high enough to allow neutrino production in $pp$ interactions of accelerated particles scattered back towards the accretion region, as discussed in [NMB93].

The model from [NSAK02] also relies on proton acceleration at the base of the jet but predicts neutrino emission from $p\gamma$ processes in the ambient photon field, dominated by 'soft' optical or UV radiation from the disk. In a study of the resulting secondary gamma-ray fluxes in relation to the required photon densities and the jet orientation, basic conditions for increased neutrino output are derived in [NS02]. In particular, blazars with large TeV gamma-ray fluxes as those detected by IACTs are disfavoured in this framework. The escape of these high energy photons hints at low optical depths and thus reduced proton interaction rates. The list of the most promising objects for neutrino emission compiled in [NS02] is discussed in the context of point source search results in chapter 8.

A similar approach deals specifically with FSRQs as a blazar subclass that exhibits bright photon fields. These could serve as external targets for protons accelerated in rather compact jets inside the inner host galaxy [AD04]. The so-called broad line regions observed in certain AGN, assumed to originate in fast moving gas clouds within a parsec of the black hole, would provide such photons.

### Neutrinos from AGN jets

Apart from the dense core region, the full length of the plasma jet can be considered as a possible neutrino production site in AGN. Relativistically boosted inhomogeneities move through a jet and produce shocks which then cause Fermi acceleration of electrons and protons. This inclusion of hadronic processes can also explain the typical synchrotron radiation features of AGN [BS87] and several detailed approaches to understand the properties of such high energy processes are reviewed in [Man97].

A generalised attempt to explain the two-peak structure in BL Lac objects in a hadronic framework is discussed in [MP01, MPE$^{+}$03], called the synchrotron proton blazar model. Assuming larger magnetic field strengths than necessary in purely leptonic models, protons in the jet are accelerated to sufficiently high energies to generate synchrotron radiation. This component provides a major

---

[2] The quantitative predictions of neutrino fluxes proved to be too optimistic and were revised in an update in [Ste05].

contribution to the SED at energies from GeV to TeV and can explain the higher frequency peak in HBL spectra. Given the low overall luminosities observed for this BL Lac subclass, $p\gamma$ interactions would be suppressed due to insufficient photon targets and consequently not produce large neutrino fluxes. For LBLs, on the other hand, the synchrotron proton blazar model predicts a significant gamma-ray component in the SED that stems from the decays of $\pi_0$, generated in in $p\gamma$ photo-production. The charged pions from the same processes would not only lead to further synchrotron contributions from the emerging muons and electrons, but also yield a flux of neutrinos.

A general caveat to hadronic models is the typical time scale necessary to guarantee acceleration of the heavy protons to high energies. This is in contrast to the fact that very short periods of variability, on the order of hours or even less, have been observed in AGN. However, as argued in [Sta04], a more complex scenario than only one zone of shock acceleration could generate such fluctuations, for example several plasma knots overtaking each other at different velocities.

# Chapter 3.

# Neutrino astronomy

This chapter provides an overview of the physics concepts and detection methods of very high energy neutrinos. The first section deals with the propagation and interaction of neutrinos between source and detector. It also covers the production of induced muons and their optical detection. In the second part, the past and current efforts of high energy neutrino astronomy are briefly summarised, followed by an overview of important concepts and point source search strategies. A new approach to extend the reach of such searches is introduced in the final section.

## 3.1. Neutrino propagation and detection

### 3.1.1. Neutrino oscillations

The phenomenology of neutrino oscillations has been studied in experiments with neutrinos produced in the sun, the atmosphere, fission reactors and accelerators, for a review see for example [STV08]. The $3 \times 3$ Maki-Nakagawa-Sakata-Pontecorvo (MNSP) matrix $U$ [MNS62, GP69] allows expressing the flavour eigenstates $\nu_\alpha$ $(\alpha = e, \mu, \tau)$ as a superposition of mass eigenstates $\nu_i$:

$$|\nu_\alpha\rangle = \sum_{i=0}^{3} U_{\alpha i} |\nu_i\rangle \; . \tag{3.1}$$

For propagation over a distance $L$ in vacuum, the resulting probability to observe flavour $\beta$ as a final state of a neutrino with initial flavour $\alpha$ and energy $E$ is:

$$\begin{aligned} P(\nu_\alpha \to \nu_\beta, L) &= |\langle \nu_\beta | \nu_\alpha(L) \rangle|^2 \\ &= \sum_{j,k} U^*_{\alpha j} U_{\beta j} U_{\alpha k} U^*_{\beta k} \exp\left(-i \frac{\Delta m^2_{jk} L c^3}{2E\hbar}\right) \; . \end{aligned} \tag{3.2}$$

Here, $\Delta m^2_{jk}$ are the differences between the squared neutrino masses.

To calculate oscillation effects for neutrinos from distant astrophysical objects, one can assume propagation through the vacuum. Matter effects leading to enhanced flavour oscillations for neutrinos have been excluded to play a significant role for the environments surrounding source candidates like AGN and GRBs as well as for propagation through our galactic halo [LS00].

When we extract the length of one oscillation period from (3.2),

$$L_{jk}(E) = \frac{4\pi E\hbar}{\Delta m_{jk}^2 c^3} = 2.48\mathrm{m}\left(\frac{E}{\mathrm{MeV}}\right)\left(\frac{\mathrm{eV}^2}{\Delta m_{jk}^2}\right) , \tag{3.3}$$

it becomes apparent that it is small compared to astronomical distances between source and detector. Even at EeV energies, intergalactic space provides a baseline much longer than $L_{jk}$. Thus it is possible to average over rapid oscillations, simplifying equation (3.2) as in [AJY00] to:

$$P(\nu_\alpha \to \nu_\beta; L \to \infty) = \sum_j |U_{\alpha j}|^2 |U_{\beta j}|^2 . \tag{3.4}$$

The neutrino flavour ratio at a generic source was motivated in section 2.1.3 to be $\nu_e : \nu_\mu : \nu_\tau = 1 : 2 : 0$. The calculation in [AJY00] makes use of basic experimental knowledge about the properties of the MNSP matrix to show that the probability for individual flavour transformations, equation (3.4), then leads to a cosmic neutrino flux at Earth with a flavour ratio 1 : 1 : 1. It is crucial to consider this change in the composition of a cosmic neutrino flux when one wants to study the relation between measured or excluded neutrino emissions from astrophysical sources.

A possible transition to a ratio 1 : 1.8 : 1.8 for very high energies due to a deviation in the initial composition at the source is proposed in [KW05]. For atmospheric neutrinos, discussed in section 3.1.4, flavour oscillations only play a role at lower energies than those relevant for the work presented here. At 10 TeV and above, the oscillations over lengths on the order of the Earth radius are suppressed in equation (3.2).

### 3.1.2. Neutrino interactions

#### Neutrino cross sections

Neutrinos in the Standard Model interact only via the weak force. Scattering processes involving a neutrino $\nu_l$ (with flavour $l$) and a nucleon $N$ (from the atoms in the detector medium and its surroundings) are discussed in the following to analyse the possible modes of detecting astrophysical neutrinos. If the interaction is mediated by the electrically charged boson $W^\pm$, one speaks of a charged current (CC) interaction, if mediated by the $Z^0$ boson it is called a neutral current (NC) interaction. Lepton number conservation leads to the production of a charged lepton $l$ in the former and a neutrino in the latter process, keeping the original flavour:

$$\begin{array}{llll} \nu_l + N & \xrightarrow{W^\pm} & l + X & \text{(CC)} \\ \nu_l + N & \xrightarrow{Z^0} & \nu_l + X & \text{(NC)} \end{array} \quad .$$

This thesis deals with the search for point sources, relying on an accurate reconstruction of the neutrino arrival direction. Muons from charged current interactions provide the best opportunity for this, since their tracks can be observed and reconstructed with the optical Cherenkov technique described in the next section.

The remnant $X$ of an initial nucleon in a neutrino interaction produces a hadronic shower. This cascade-like energy release can in principle be observed with the same optical instruments that are used for muon track detection. However, compared to the typical spacing of tens of meters between detector components in neutrino telescopes, this energy release is locally confined and thus makes it difficult to extract any direction information. In consequence, only charged current interactions are considered for neutrino detection in the analysis presented here.

The cross sections for the deep inelastic scattering processes of neutrinos can be calculated by making use of the parton distribution functions for nucleons. These are derived from collider experiments, requiring an extrapolation to describe the highest energies accessible with neutrino telescopes. A detailed description is given in [GQRS96], with updated results in [GQRS98] based on tabulated parton distribution functions from [LHK$^+$97]. Using more recent information on the nucleon structure from the ZEUS collaboration [C$^+$03], improved results for the charged current cross sections are provided in [CSS08].

The cross section for neutrino scattering rises with energy, as depicted in Fig.3.1. Anti-neutrinos interactions have reduced cross sections at low energies, an effect of the contribution of valence quarks as opposed to the dominance of sea quarks, explained in [GQRS98]. Neutrino telescopes of the type described below cannot distinguish between neutrinos and anti-neutrinos and are sensitive to both contributions. In the following, *neutrino* always refers to both particles and antiparticles.

In charged current interactions, the angle between an incoming muon neutrino and the observable induced muon track is limited to small values due to strong relativistic boosting of very high energy neutrinos. In an approximate parametrisation, the mean scattering angle is given by

$$\langle \Delta\psi_{\nu\mu} \rangle = \frac{0.7}{(E_\nu/\mathrm{TeV})^{0.7}} \tag{3.5}$$

in [LM00]. Already at energies around 20 TeV, the deflection is $\leq 0.1°$. Compared to the limited track reconstruction accuracy on the order of 1°, discussed in chapter 5, this inherent uncertainty is negligible for a high energy neutrino search.

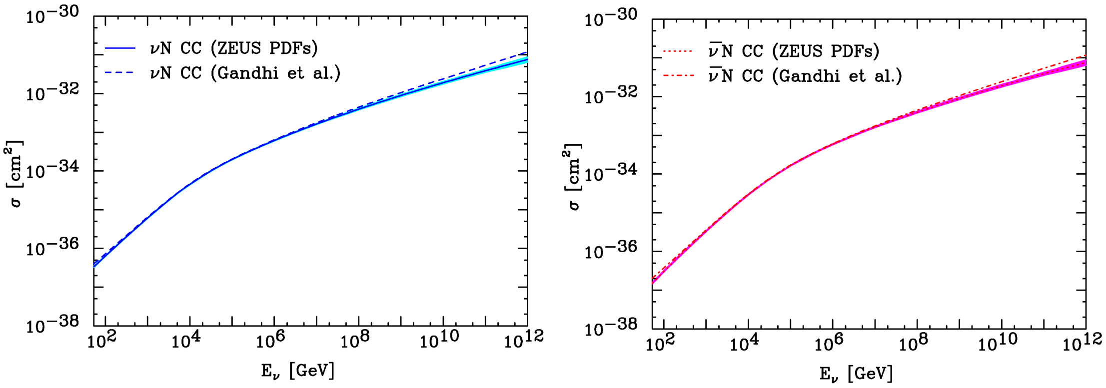

Figure 3.1.: Total CC cross sections for neutrinos (left) and anti-neutrinos (right) scattering off nucleons. The dashed lines show older results from [GQRS98] while the solid lines (with $1\sigma$ uncertainty bands) are based on ZEUS structure functions. Plots taken from [CSS08].

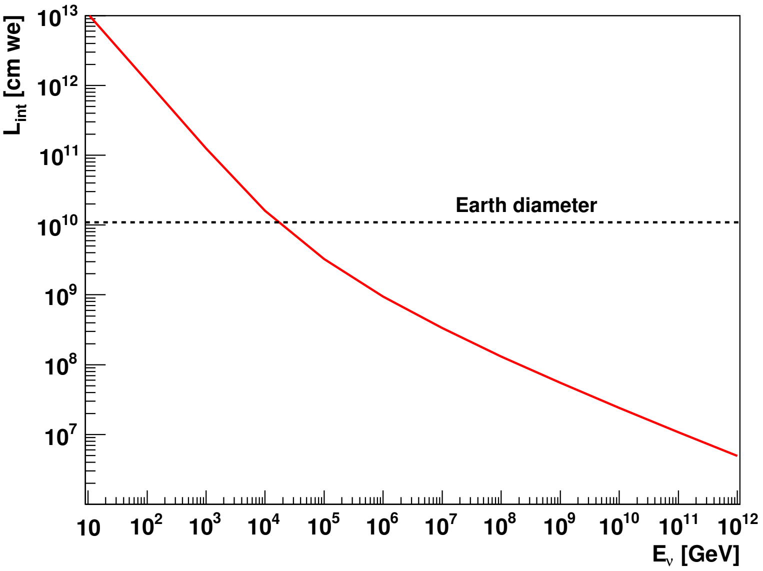

Figure 3.2.: Neutrino interaction length $L_{int}$ in matter as a function of energy, taking into account CC and NC cross sections. The length is given for a water equivalent (we) medium and the dashed line corresponds to the diameter of Earth in these units, i.e. the column depth for a vertically upward going (*up-going*) neutrino. Based on data from [GQRS98].

Neutrino-electron scattering can normally be neglected compared to interactions with nucleons due to the small mass of the electron. An important contribution for a narrow energy range occurs however around 6.3 PeV, were the mediating $W^-$ boson is resonantly produced in $\bar{\nu}_e e^-$ scattering [Gla60]. With respect to the addition to the muon flux through $\bar{\nu}_e e^- \to W^- \to \bar{\nu}_\mu \mu$, the cross section at this Glashow resonance is nearly a factor 40 greater than the $\nu_\mu N$ contribution, but drops below the latter within one decade in energy, see [GQRS96] for details.

### Neutrino absorption inside Earth

For neutrinos below the TeV scale, even a body as large as Earth is basically transparent, but this is not true at higher energies. The reason is the rise of the cross section with energy for charged current interactions, as shown in Fig. 3.1. The neutral current cross section has a very similar behaviour, though with absolute values reduced by a factor of approximately 0.4 or smaller [GQRS98].

It is necessary to study absorption of neutrinos in Earth before they reach the detector, since a standard approach to neutrino searches is looking for tracks from below the horizon, using Earth as a filter against other high energy particles. A measure for the mean distance a neutrino travels before it scatters on a nucleon is the water equivalent (we) interaction length

$$L_{int} = \frac{1}{n_A \cdot \sigma_{\nu N}(E_\nu)} , \tag{3.6}$$

where Avogadro's number $N_A = 6.022 \times 10^{23}\mathrm{mol}^{-1}$ gives the number density of $n_A = 6.022 \times 10^{23}\mathrm{cm}^{-3}$ for nucleons in water. The resulting interaction length is shown in Fig. 3.2, together with the Earth radius which equals a column depth of $1.1 \times 10^{10}$ cm we. The fact that the interaction length becomes smaller than this radius for energies exceeding 50 TeV severely limits the search for very high energy neutrinos from below the horizon.

To compare the chances for so-called up-going neutrinos to reach a detector, Fig. 3.3 shows survival probabilities, defined as

$$P_\nu = \exp\left(-\frac{x(\theta)}{L_{int}(E)}\right) , \tag{3.7}$$

for several energies and track zenith angles $\theta$ leading to different column depths $x(\theta)$. An angle of $\theta = 90°$ describes a neutrino approaching from the horizon, while a track with $\theta = 180°$ runs vertically through Earth from the opposite hemisphere of the detector's location, which is chosen to lie 2 km below the surface. The shape of the curves in Fig. 3.3 is determined by the inner structure of Earth, modeled as spherically symmetric based on the Preliminary Earth Model [Jam89] as presented in [GQRS96]. The steepening above $\sim 145°$ stems from the passage of the tracks through the high density core region. Already at particle energies of

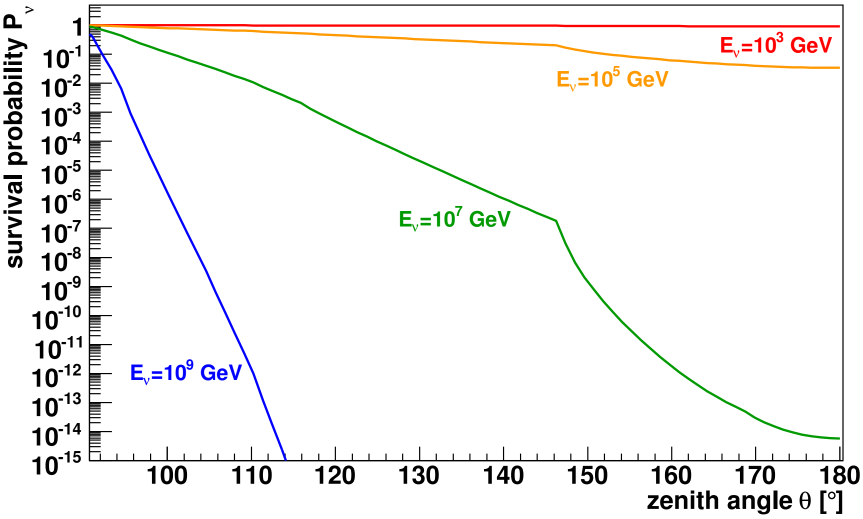

Figure 3.3.: Neutrino survival probabilities $P_\nu$ for reaching a detector, located 2 km below the surface, from below the horizon as a function of zenith angle $\theta$. The four lines represent different initial neutrino energies $E_\nu$. Clearly visible are the increase of absorption with energy due to the rising cross section as well as the suppression effect of the dense core of Earth for steeply up-going tracks. Based on data from [GQRS98].

100 TeV, steeply up-going neutrinos have a probability of less than 10% to reach the detector site without being absorbed. Consequences of the shadowing of high energy neutrinos by Earth for the search for astrophysical neutrinos are discussed in section 3.3.

It has to be remarked that an up-going flux of tau neutrinos does not suffer from absorption in the same way as a flux of muon or electron neutrinos. A tau lepton, produced in a charged current interaction by a tau neutrino, generally decays before it can be absorbed, thus producing another tau neutrino of lower energy [HS98]. These prompt decays also lead to a secondary neutrino flux, with a branching ratio of 18% for the process $\tau \to \nu_\tau \mu \bar{\nu}_\mu$. The maximum contribution to the muon neutrino flux from this process is calculated in [BCK02] to be 20% of the tau neutrino flux. Additionally, muons produced directly in the tau decay can be registered inside the detector if the process occurs close enough.

Due to tau regeneration, the addition to the muon flux is constant over the full angular range below the horizon, contrary to the energy dependent absorption of muon neutrinos. Given improved energy reconstruction and better statistics, it might be worthwhile to search for such a component, but this is not within the scope of this thesis.

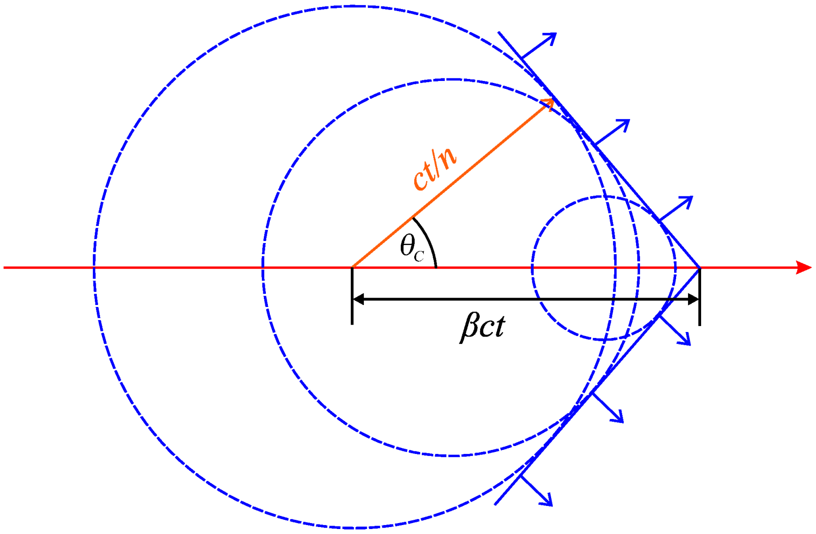

Figure 3.4.: Schematic illustration of the emission of Cherenkov radiation. The circles represent examples for the continuous emission of photons from the ionisation path which interfere and form the Cherenkov cone. See text for further description.

### 3.1.3. Optical detection of neutrino-induced muons

#### Cherenkov radiation

Current approaches to high energy neutrino astronomy rely on the optical Cherenkov technique to detect and reconstruct muon tracks, which stem from neutrino interactions inside or near the detector. When a charged particle in a dielectric medium moves faster than the local phase velocity of light, photons emitted due to the polarisation and relaxation of atoms along the path interfere coherently, thus producing a light cone called Cherenkov radiation. Explained schematically in Fig. 3.4, the angle of emission between coherent photons and the track is a function of the velocity $\beta = v/c$ and the index of refraction $n$:

$$\cos(\theta_C) = \frac{1}{n\beta}\,. \tag{3.8}$$

Considering the deep ice properties at the South Pole relevant in IceCube, discussed in section 4.1.1, an index of refraction of $n \approx 1.31$ at a wavelength of $\lambda = 589$ nm leads to $\theta_C \approx 40°$ for particles with $\beta \approx 1$. To calculate the total Cherenkov emission for a particle of charge $z \cdot e$, the differential expression for the number of photons per unit length $x$ and wavelength $\lambda$ is given by the

Frank-Tamm formula [Jac96],

$$\frac{d^2N}{dxd\lambda} = \frac{2\pi\alpha z}{\lambda^2}\left(1 - \frac{1}{\beta^2 n(\lambda)^2}\right) , \tag{3.9}$$

with the fine structure constant $\alpha = 1/137$. Using this formula with an approximately constant index of refraction for the range of 300 to 600 nm, corresponding to IceCube photomultiplier sensitivities, one obtains $\sim 3 \times 10^4$ photons/m from a highly relativistic muon. Fixing the velocity at $\beta = 1$ is a reasonable approximation for high energy muon tracks to be studied in a neutrino telescope. The number of Cherenkov photons per track length is therefore basically independent of energy.

This Cherenkov emission from a TeV muon itself represents only a fraction on the order of $10^{-5}$ of the total energy loss [LM00], due to other processes summarised in he following section. Nevertheless, the total yield of Cherenkov light is much higher, due to secondary particles produced along the track. These induce electro-magnetic or hadronic showers with photon emission from all particles with energies above the Cherenkov threshold defined by $\beta \geq 1/n$, translating into an energy threshold,

$$E_C \geq mc^2 \frac{1}{\sqrt{1 - 1/n^2}} , \tag{3.10}$$

for a particle of mass $m$. A parametrisation for the number of emitted Cherenkov photons can be found in [Wie95], predicting a shower from a GeV particle to emit several times the light yield which the primary muon radiates per meter track length.

In contrast to the direct Cherenkov emission from the track, the total light yield increases with the muon energy since a larger number of secondaries is generated. This dependence can be used for an approximate energy reconstruction, outlined in section 5.4.

### Muon propagation in matter

The techniques to reconstruct the direction and energy of muon tracks are introduced in chapter 5. Here, the physics determining the track lengths in matter are discussed in order to estimate the typical scales. For muons travelling through matter, the energy loss from ionisation of the surrounding medium is constant and dominates up to GeV energies over other processes, including the loss from the final decay. Detailed studies in [RC01] show that above a muon energy of 1 TeV other processes surpass ionisation as the major channels of energy loss, namely bremsstrahlung, photo-nuclear interactions and $e^+e^-$-pair production. While ionisation can be treated as quasi-continuous, the other interactions happen in discrete events of a stochastic nature and are thus subject to major fluctuations. The resulting distribution of survival probabilities and average muon ranges in rock

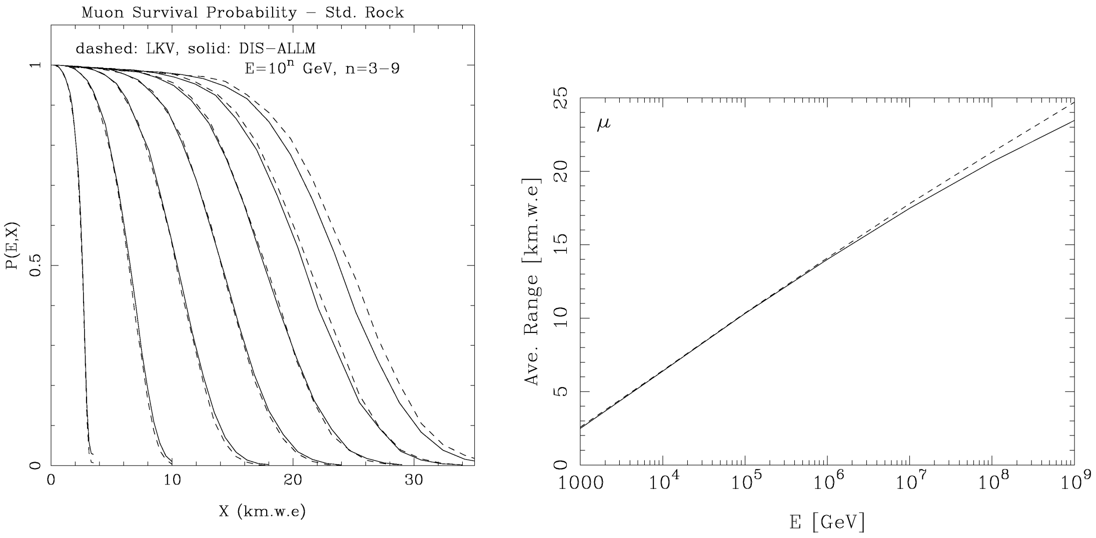

Figure 3.5.: Survival probabilities (left) and average range (right, final energy ≥1 GeV) for muons in rock. The solid and dashed lines refer to different structure function parametrisations. Both plots are taken from [DRSS01].

based on Monte Carlo simulations in [DRSS01] are shown in Fig. 3.5.

One can approximate the total energy loss per track length $x$ with a linear function,

$$\frac{dE}{dx} = -a - bE\,, \tag{3.11}$$

where the parameter $a$ quantifies ionisation losses and $b$ encompasses all other processes. Maximum muon ranges can be obtained by solving equation (3.11) with:

$$R(E_\mu, E_\mu^{min}) = \frac{1}{b}\ln\frac{a + bE_\mu}{a + bE_\mu^{min}}\,. \tag{3.12}$$

For a fixed minimum energy threshold, the maximum track length rises logarithmically with energy. Therefore, the volume of neutrino interactions from which muons can be detected gets larger for higher energies. With $E_\mu^{min} = 10$ GeV in (3.12) and coefficients $a$ and $b$ from a detailed Monte Carlo approach in [CR04], water equivalent muon ranges were calculated in [Fra07] which vary from ∼10 km for 10 TeV to ∼70 km for 1 EeV.

In a neutrino point source source search one reconstructs muon tracks passing through the detector, without the necessity of knowing the location of the interaction vertex. While this approach allows only to set lower limits on the energy of the original neutrino, it has the advantage of increasing the chances of muon detection at higher energies due to the larger volume for interactions outside the detector.

Apart from inelastic processes, elastic scattering of muons off nucleons from the surrounding matter can affect the direction of propagation. As has been checked in [Ack06], the average deviation turns out to be significantly smaller than the uncertainty due to the emission angle in the neutrino interaction vertex, equation (3.5). Elastic scattering can thus be regarded as irrelevant in the following discussion of point source searches.

### 3.1.4. Atmospheric muons and neutrinos

In the search for an astrophysical flux of neutrinos, and more precisely in a point source search based on neutrino induced muon track reconstruction, one is faced with two background components. They are referred to as atmospheric muons and atmospheric neutrinos. Both fluxes originate in extended particle showers due to interactions of charged cosmic rays in the atmosphere.

Atmospheric muons are dominantly produced in decays of pions and penetrate the surface to be detected as a downward going (*down-going*) flux in an underground Cherenkov detector array, with hundreds or thousands of muons arriving in narrow bunches called *muon bundles*. If the spatial resolution of a detector is too low to resolve the components of these bundles, they have a signature very similar to a bright single muon as produced by a very high energy neutrino. Atmospheric muon rates surpass expected astrophysical fluxes by at least six orders of magnitude and form the major background, in particular for studies of down-going events.

For IceCube, located at a depth larger than 1.5 km below the surface, atmospheric muons with zenith angles $\theta \gtrsim 85°$ are absorbed on their way through Earth. However, due to a non-perfect direction reconstruction efficiency, a large number of these events appears as upward going (*up-going*). Suppression of this background is a major challenge even in analyses focusing exclusively on up-going muon tracks, as discussed in chapter 5 and 6.

In the same air shower interactions that produce muons, neutrinos are also generated, mostly in decay chains like the one for pions in equation (2.6). The neutrinos reach a detector from all sides and are not distinguishable from cosmic neutrinos of the same energy. The spectrum of atmospheric neutrinos close to and above the critical energy is softened compared to the incoming primary flux with $d\Phi/dE \propto E^{-2.7}$ (see section 2.1.1), due to the interaction and decay processes of the multiple particles involved. A simplified description of the atmospheric neutrino flux above $E \geq 100$ GeV is a power law $\sim E^{-3.7}$. An analytic form of the conventional flux, including more features, is given in [Vol80] and a more recent table of flux values for a wide range of energies is presented in [HKK$^+$07]. Figure 3.6 shows the spectrum at very high energies measured with the AMANDA-II experiment.

Atmospheric neutrinos above an energy of 100 GeV stem mostly from kaon decays [Gai07]. At the critical energy of $\epsilon_{K^\pm} = 850$ GeV [Ack06], the interaction

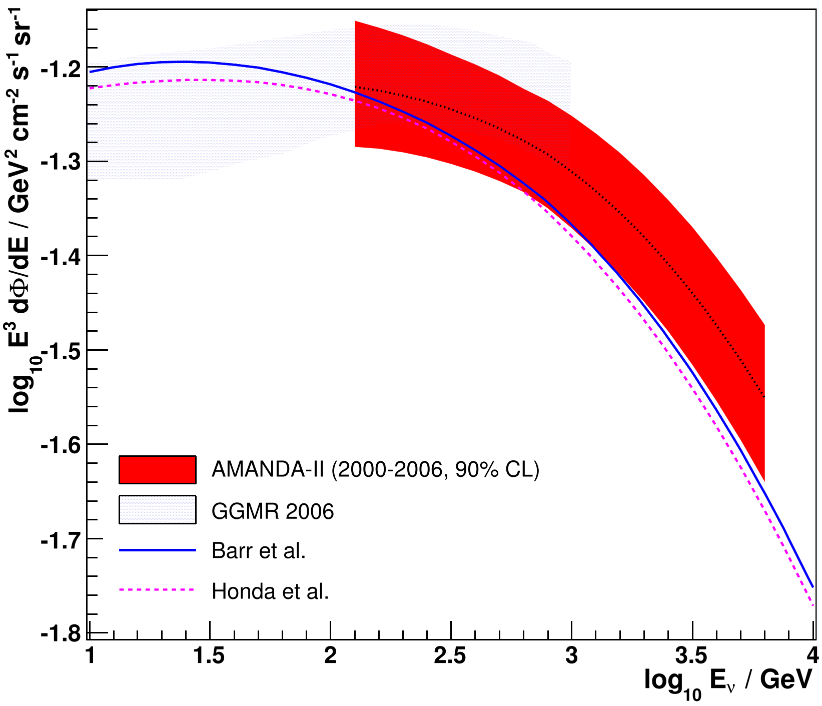

Figure 3.6.: Angle averaged spectrum of atmospheric muon neutrinos ($\nu_\mu + \bar{\nu}_\mu$) in a 90% confidence level belt with the central best fit given as the dotted line. A result from Super-Kamiolkande [GGMR06] as well as predictions from Barr et al. [BGL+04] and Honda et al. [HKK+07] are also shown. Plot taken from [A+09a].

length for kaons in the atmosphere drops below their decay length. It is therefore expected that at even higher energies a small fraction of short-lived particles from these interactions dominates the neutrino production through semileptonic decays of heavy hadrons containing charm quarks. Predictions for these prompt neutrino fluxes differ by almost 2 orders of magnitude, see for example [GGV03].

The steep spectrum of atmospheric muons and neutrinos allows a reduction of this flux component by selecting only events of sufficiently high energy. These are more likely to stem from astrophysical acceleration processes with their harder primary spectra, see section 2.1.3. For this reason, neutrino telescopes are designed to have optimal performance at TeV energies and above. Due to limited statistics and energy resolution of current neutrino telescopes, the discovery potential for point source searches is improved by suppressing the background only to a certain degree, avoiding a too strong impact on the signal efficiency. A search for excesses of events from individual directions can then be achieved by comparing spatial clustering of neutrino candidates with averaged background rates. The techniques will be introduced in the following section and discussed in detail in chapter 7.

## 3.2. Instruments and methods of high energy neutrino astronomy

### 3.2.1. Neutrino telescopes

Neutrino astronomy in general has to deal with very small event rates due to the weak interaction cross sections. Solar neutrinos in the MeV energy range are studied by various experiments and are observed on a level allowing to constrain parameters of the model for fusion processes in the sun [McD04]. For GeV to low TeV energies, the MAKRO [A+01] and SUPER-KAMIOKANDE [Thr09] collaborations performed point source searches.

At very high energies above the GeV range, the power law behaviour of expected astrophysical fluxes leads to a situation in which it is necessary to consider detection volumes of the order of a cubic kilometer, exceeding any artificial structure. Natural environments which are transparent enough to allow optical detection of Cherenkov light from muons produced in charged current interactions are water, in deep lakes or the ocean, and ice, in large glaciers. The attenuation of light is similarly good in both media. This is due to different properties, though, as for ocean water the very large scattering length of $\sim 200$ m dominates over an absorption length of 50 to 60 m, while in ice the short scattering length of 10 to 20 m is compensated by an absorption length of $\sim 100$ m or greater[1], see [LM00].

After the first aborted attempts of the DUMAND collaboration [B+90] to install a neutrino telescope in ocean water close to Hawaii, the first under-water high energy atmospheric neutrinos where detected with the BAIKAL experiment [B+00]. It is operated since April 1998 in Lake Baikal, Siberia, at a depth of 1.1 km and was extended from the original 144 to 200 photo-multiplier tubes (PMTs), with current plans aiming for considerably larger arrays [HH02].

In the Mediterranean sea, three experiments with different approaches to optical Cherenkov detector setups are operated. The NEMO initiative has finished a series of site explorations in the sea near Sicily, Italy [M+08]. The NESTOR collaboration started to deploy a detector with several instrumented *floors* at a depth of 2 km off the coast of Southern Greece [A+06c]. The ANTARES collaboration [A+06d] has finished the installation of their detector, consisting of 12 lines equipped with photomultipliers, in 2008. It is located at the bottom of the sea south of Toulon, France, and has presented first results for different neutrino analyses [S+09].

In the deep ice between 1.5 and 2 km below the surface at the geographical South Pole, the AMANDA collaboration began taking data with a first detector, called AMANDA-B10, in 1997 [A+00]. It was extended to the final AMANDA-II

---

[1] Contrary to laboratory measurements, absorption lengths in deep polar ice were found to exceed 200 m in the violet optical band [A+06b]. Optical properties of the South Pole ice are discussed in section 4.1.1.

configuration of 677 PMTs on 19 strings and operated successfully as the largest neutrino telescope since 2000. After serving partially as a testbed for technologies to be used in its successor, the detector ran as an integrated part of the growing IceCube Observatory since 2007, until AMANDA was finally decomissioned in May 2009. Results from AMANDA are still advancing the field of high energy neutrino astronomy, for example through atmospheric flux measurements [A+09a]. Currently, IceCube is the largest neutrino telescope, described in detail in section 4.1.

At supra-EeV energies, another window for neutrino astronomy opens via the observation of extensive air showers. Due to the rising cross section, neutrinos at these energies can induce large showers inside the atmosphere. With air shower arrays, it is possible to observe and reconstruct these events if they occur in a narrow band around the horizon. The HIRES experiment [A+08b] and the PIERRE AUGER OBSERVATORY [A+09i] have published the best flux limits obtained with this approach. Such extremely high energies are also covered by searches for radio emissions from neutrino showers, with recent limits presented by the RICE [K+06] and ANITA [G+09] collaborations.

## 3.2.2. Effective areas and point source sensitivity

### Neutrino effective area

To compare the capabilities for neutrino searches between different experiments and also separate analyses within the same experimental framework, it is useful to introduce the concept of *neutrino effective areas*. As discussed in section 3.1.3, searches for neutrinos induced muon tracks require only a certain part of the particle track to go through the instrumented volume. This region can thus be much smaller than the space of observable interactions defined by muon ranges in the medium. For point source searches it is therefore more appropriate to compare the number of detections not per volume but per area. The efficiency depends on the incoming angle, due to effects of detector geometry, and the energy, defining muon range and brightness.

The effective area is the equivalent area over which the same number of neutrinos from a given flux strength would be counted as the one measured in a fixed analysis or event selection. This definition combines the physics constraints of weak interactions with detector and cut efficiencies in one parameter. The number of detected neutrino events $N_D$ over a time $t$ for a given flux $\Phi_\nu$ (in units of particles per time, area and steradians) from an observable solid angle $\Omega$ and for an infinitesimal interval $\Delta E$ around the energy $E$ can then be expressed via the effective area $A_{eff}$:

$$N_D = \int dt \int d\Omega \int dE \; \Phi_\nu(t, \Omega, E) \, A_{eff}(\Omega, E) \,. \tag{3.13}$$

In Monte Carlo simulations for an isotropic flux or a limited angular region, i.e. after integration over $d\Omega$, the effective area can be calculated by comparing the detected number of events $N_D$ with the number of generated incoming neutrinos $N_G$ for the true (angle dependent) detection area $A_{true}$ via:

$$A_{eff} = \frac{N_D}{N_G} A_{true} \,. \tag{3.14}$$

Typical neutrino effective areas for a search based on muon tracks in a cubic kilometer array are around 0.1 $\mathrm{m}^2$ for a neutrino energy of 1 TeV. The effective area rises above $10^3$ $\mathrm{m}^2$ for particle energies of 10 to 100 PeV, motivating the extension of analyses to this range as outlined in section 3.3.

### Point source searches

A point source search for astrophysical neutrinos relies primarily on the identification of spatial clustering of track directions. A source can then be detected as a significant excess of events at a given location compared to the surrounding region dominated by an isotropic background of atmospheric neutrinos or muons. The sensitivity depends on the suppression of the background to a level at which event accumulations for expected source fluxes are visible over statistical background fluctuations, see chapter 6. Another crucial factor is the experimental angular resolution discussed in section 5.3.

With an assumption on the spectral shape of a given source or class of candidates, it is possible to use estimated event energies as a parameter to separate signal from background, since in general the signal spectrum is expected to be harder than the atmospheric background. In the case of atmospheric muons, also other qualifiers are used to distinguish events which are induced by a neutrino. In chapter 6 it is described how cuts on different event characteristics were employed in this work to reduce the data to an optimised selection. For neutrino candidates in the resulting final sample only spatial information, and in one dedicated test also the arrival time, is used to derive significances for event clusters.

In a different approach, a search can rely on a likelihood formalism. At a given location, the probability for a signal contribution from a neutrino source is evaluated. All events in the vicinity of the chosen location are weighted according to individual direction uncertainty, energies and possibly other variables. A detailed descriptions is given in [Neu03, NK06] and a recent study in [BDdP$^+$08], but this method is not applied in the work presented here.

In a binned point source search as the one central to this work (see chapter 7), the spatial clustering of events in a given direction is determined by counting events in a small solid angle around the point of reference. This number is compared to the expected average background value. The latter depends not only on the size of the angular bin, but also on the zenith angle, due to the absorption effects described in section 3.1.2.[2]

The average number of background events is obtained directly from measured data in the same zenith band to avoid relying on background simulation with its inherent uncertainties. The probability of an excess of events in a given bin to be a signal contribution on top of the background can be calculated via Binomial statistics. Detection probabilities have also to include so-called *trial factors* to account for the statistical implications of repeating a test for signal excesses for many directions in the sky. The details for a scan of the sky with spherical angular bins are presented in section 7.1.

### Flux limits and sensitivity

Only if the probability for a given excess of events to be caused by a background fluctuation is below a pre-defined threshold[3] the result is considered to be a discovery, i.e. a point source of neutrinos. If this is not the case, it is possible to derive an upper limit on the observable flux from the tested direction. This is done by constructing confidence belts which comprise the possible outcomes of a statistical test, here the number $n$ of observed events, in a defined range of probabilities with respect to all possible outcomes.

In the case of searching for signal neutrinos on a uniform background, event counts are simulated with a fixed mean background $b$ per bin plus the contribution of a given point source flux. These signal neutrinos are added as discrete events following a Poisson distribution [Poi37] with the mean $s$. For a confidence level (CL) between 0 and 1, the smallest interval of integer event counts $n$ with the boundaries $[n_l, n_u]$ is then determined by the sum of probabilities $P(n|s+b)$:

$$\mathrm{CL} \leq \sum_{n=n_l}^{n_u} P(n|s+b)\,. \tag{3.15}$$

The experimental result for the number of observed events $n_e$ is used to determine the maximum signal contribution for which this outcome falls into the confidence interval. This maximum contribution is the mean number of simulated neutrino signals for which the given observation coincides with the lower boundary of the confidence interval, see Figure 3.7.

There is no unique prescription in what order the interval is filled with the simulated outcomes, hence also no universal definition of the precise upper and lower boundaries $n_{l/u}$. Many experiments follow the prescription of [FC98] based on likelihood ratios $R_n$. Values for for the number of detected events $n$ are added

---

[2] Typical neutrino telescopes are symmetric in their azimuthal layout, but not with respect to the zenith angle, hence also the acceptance and angular resolution depend, to a certain extent, on the zenith angle.

[3] A widely used convention is a threshold of five standard deviations from the peak of a one-sided Gaussian function, equivalent to a probability of $\sim 2.9 \times 10^{-7}$.

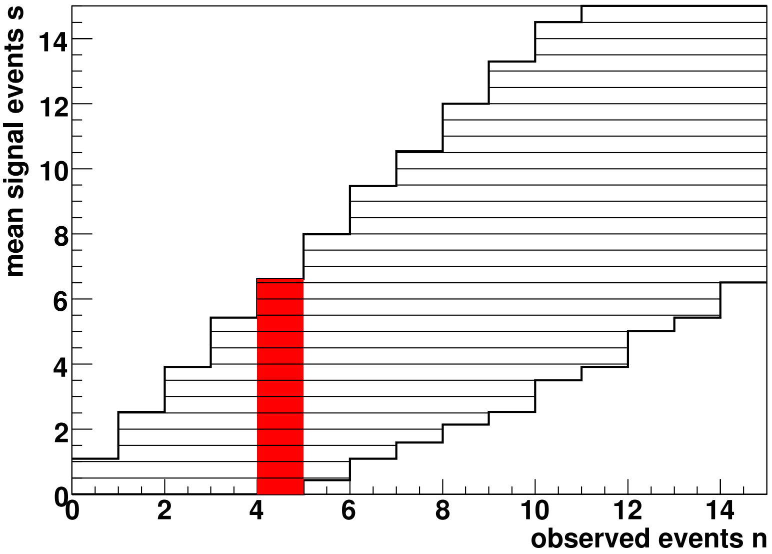

Figure 3.7.: Illustration of the derivation of upper limits from a construction according to [FC98]. Horizontal lines indicate the 90% confidence intervals of observed events $n$ for a given mean number of signal events $s$ according to the Poisson distribution with a background of $b = 2$ events. The enveloping lines represent the upper and lower limits on $s$ for each observable event number value, with the one for $n = 4$ highlighted in red.

to an interval in the order determined by the probability quotient:

$$R_n = \frac{P(n|s+b)}{P(n|s_{max}+b)} \,. \tag{3.16}$$

$P(n|s+b)$ is the probability of this outcome to occur for the simulated signal strength, while the denominator describes the probability of the same outcome given a (physically allowed) signal strength $s_{max}$ that maximises $P$. A full description and examples are provided in [SL04].

With the confidence belt method one obtains the maximum number of signal events $\mu_{CL}$ that could be hidden in a given observation, while being considered not significant as a source discovery. Within the defined confidence level, chosen to be 90% in this work, it is therefore excluded that a neutrino flux from the tested direction is larger then the one equivalent to this event limit $\mu_{90}$.

To calculate the excluded flux value, the number of observed events $N_{\Phi_0}$ in the detector for a given reference flux $\Phi_0$, summed over the time period of the analysis, is obtained from a full simulation of the experiment. This includes all physical effects of neutrino propagation and interaction as well as the detector efficiency and event selection choices. The flux limit $\Phi_{lim}$ is then derived by scaling the reference flux with the measured event limit $\mu_{90}$:

$$\Phi_{lim} = \frac{\mu_{90}}{N_{\Phi_0}} \Phi_0 \,. \tag{3.17}$$

The flux limits obtained within the analysis presented in this thesis are discussed in chapter 8.

To define a point source sensitivity for comparison between different searches, and also as a parameter on which to optimise an analysis, an average upper limit $\langle \mu_{90} \rangle$ is calculated. It is based on the probabilities $P(n|b)$ of many individual outcomes for searches on simulated background-only samples:

$$\langle \mu_{90} \rangle = \sum_n \mu_{90}(n, b) P(n|b) \,. \tag{3.18}$$

This average upper limit does not depend on a specific experimental result. It scales with the signal to background ratio. Due to detector acceptance and neutrino absorption effects it is generally a function of the zenith angle. In the same way as for an individual flux limit, equation (3.17) can be used to transform the average event number limit into a flux limit called sensitivity.

### 3.2.3. Multi-messenger approaches

Neutrino astronomy makes use of a unique messenger that can propagate without significant absorption or deflection from the inner regions of cosmic sources to the detectors. It can therefore substantially increase the knowledge about highly energetic acceleration processes in the Universe. Nevertheless, information from other observation channels has to be used to form a complete picture and allow conclusions about the complex underlying physics.

In a direct multi-messenger approach, measurements with photons or cosmic rays can help to design neutrino searches that test dedicated neutrino flux predictions. A good example is the search for neutrinos from gamma-ray bursts, in which the observed time and location of a burst makes it possible to define a narrow search window for neutrino excesses, thus reducing the background dramatically. In steady source searches, for example data from IACTs are used to determine promising locations of particle acceleration to TeV energies. The significance of neutrino observations from these directions would be boosted due to the a priori hypothesis.

From the perspective of neutrino telescopes, such approaches involving multiple messengers are *passive*, since only previously available data is used. In most AMANDA and IceCube point source analyses, this idea was used to arrive at a source list, based on photon observation a various wavelengths. It was determined before the observations, i.e. event counts or likelihood scans, were made. Chapter 7 presents passive multi-messenger concepts of this kind. A direct correlation study based on charged cosmic rays and independent of information on astronomical objects is the topic of a follow-up analysis in chapter 9.

A different possibility to perform multi-messenger astronomy is to use neutrino searches on the *active* side as triggers for other observations. Within the IceCube experiment, one completed and two on-going projects are searches of this kind. The first was a setup involving the observation of neutrino events from pre-defined source candidates, which lead to triggers being sent to the MAGIC telescope. Results of this so-called *gamma-ray target of opportunity* are published in [A$^+$07c]. Still in the preparatory phase is a more elaborate successor of this project, with a recent status report given in [FB09].

The Optical Follow-Up [F$^+$09] programme is currently running and has been collecting data since April 2008. Observations of two coincident neutrino candidates are used to trigger automatic optical telescopes in the search for supernova signals.

## 3.3. Extending point source searches above the horizon

Neutrino point source searches with the AMANDA detector, and now also with the growing IceCube Observatory and the recently completed ANTARES experiment were based on the approach of using Earth as a filter for atmospheric muons. Samples of events reconstructed as up-going can be reduced to the level of atmospheric neutrinos coming from below the horizon, among which a scan for clusters of cosmic neutrinos is possible. The absorption effects discussed in section 3.1.2 limit possible neutrino energies to the TeV or low PeV range.

Predictions for astrophysical neutrino production, discussed in chapter 2, make this energy regime a promising area of study, but in particular AGN models suggest a strong contribution of neutrinos at and above PeV energies. And the most energetic charged cosmic rays seem to guarantee hadronic acceleration processes up to EeV energies. The expected power law behaviour with an $\sim E^{-2}$ slope of neutrino fluxes suppresses event rates at these very high energies, but with the starting era of cubic kilometer scale arrays, at least the PeV range becomes accessible.

A point source search at such energies has to be focused on the zenith angle regime at or above the horizon. Only there is the shadowing effect of neutrino absorption in matter along the path through Earth small enough to permit a significant signal rate. A particular challenge in this approach are atmospheric muons from above which can penetrate through several kilometers of water or ice to the detector, thus increasing the background by several orders of magnitude. To retain sensitivity to a neutrino signal flux, it is thus necessary to boost the rejection power. This can be achieved by using energy-sensitive selection methods.

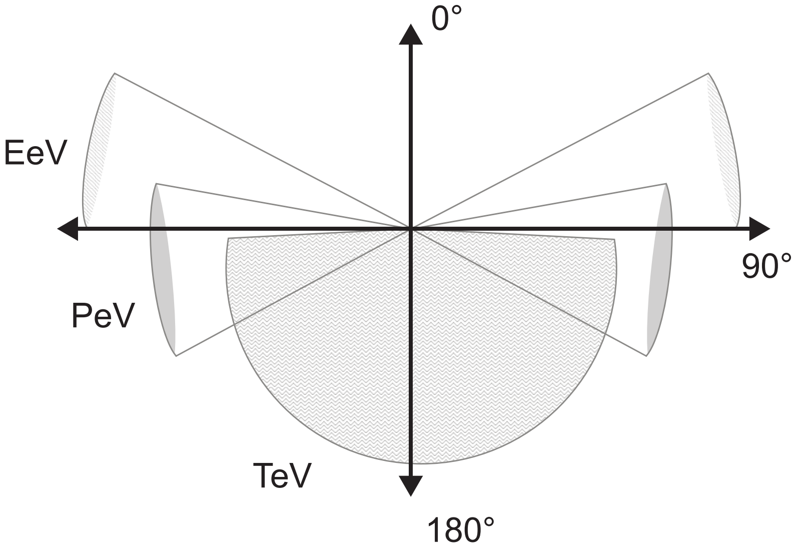

Figure 3.8.: Schematic view of approximate zenith angle regions of acceptance for muon-neutrinos in a kilometer-scale neutrino telescope. Limitations due to background suppression are taken into account, see text for explanations.

When applying a zenith-dependent threshold on event energy estimators, a cosmic flux component with an $E^{-2}$ (or even harder) spectrum could still be observable above the down-going muon flux. The atmospheric muons are suppressed since they follow a steep $\sim E^{-3.7}$ power law discussed in section 3.1.4. However, bright events with the accumulated light of multiple muons travelling in close proximity in a muon bundle constitute a background with a fake high energy appearance. This makes a simple energy cut less effective than expectations based on the primary spectra would suggest. Here, the event selection described in chapter 6 demonstrates a way of efficiently separating the down-going muon background on the basis of characteristic event signatures.

It has to be remarked that, in a study of down-going events, a signal component might not only stem from neutrinos, but also from very high energy gamma-rays. An atmospheric shower induced by multi-TeV photons in the atmosphere can produce a muon that is detected and reconstructed in the same way as neutrino-induced muons would be. A sufficiently strong photon flux would also be visible as an excess in the direction of the gamma-ray source, which is discussed for the case of IceCube in [HH03]. In the case of objects for which an accompanying gamma-ray flux is possible, flux limits derived solely under the assumption of neutrino contributions to the atmospheric background have thus to be considered as conservative estimates. Nevertheless, gamma-rays at PeV energies would be absorbed through interactions like pair production in photon fields near the source or in interstellar space. Especially fluxes from extra-galactic objects are therefore expected to be strongly suppressed.

Although neutrinos at PeV or higher energies can only be detected as down-going events, it is sensible to prepare a point source analysis in a continuous way, including both hemispheres. By defining zenith dependent selection criteria, it is possible to cover the full range of accessible particle energies from the TeV regime for up-going events to the EeV range for steeply down-going neutrinos. Figure 3.8 depicts the different angular regions of acceptance for a cubic kilometer scale experiment at a depth of several kilometers. The upper region near the zenith is only barely accessible even at the highest energies. Here, the relatively small amount of matter above the detector does not provide enough interaction volume for a sufficient number of muons to be induced and detected.

A first study of a neutrino point source search extending above the horizon was presented in [Fra07, FLBA07], concluding with a sensitivity estimate for the AMANDA-II detector. The first full point source analysis which includes the down-going regime is the core of this work and was performed with IceCube data as described in chapters 6 – 8.

# Chapter 4.

# The IceCube Observatory

The focus of this chapter lies on the IceCube experiment, currently the largest operating neutrino telescope. After a discussion of its detection medium, the deep ice in central Antarctica, the layout of the different detector components is presented. Basic electronic systems and the data taking chain are briefly discussed. The final section of this chapter provides an overview of the generation and processing of neutrinos in IceCube Monte Carlo simulations.

## 4.1. The detector

### 4.1.1. The South Pole glacier

#### Overview

The IceCube Observatory is situated at the geographical South Pole in Antarctica. The natural glacier is used as the detection medium, primarily for Cherenkov light from charged leptons and their secondaries, produced in neutrino-nucleon interactions. At this location, the ice shield is approximately 2.7 km thick with its surface at an altitude of 2.8 km, moving with a horizontal velocity of $\sim 9$ m/year towards North [PWC00].

The relevant particle physics processes with a focus on muon generation and propagation have been discussed in sections 3.1.2 and 3.1.3. Crucial for the reconstruction of direction and energy of these particles is how accurately photons can be observed and traced in the ice over distances of tens or hundreds of meters. For wavelengths between $\sim 200$ and $\sim 400$ nm, ice is the most transparent solid known [A$^{+}$95, A$^{+}$97b], but the polar cap in Antarctica is not a homogeneous medium. It is interspersed with air bubbles in the shallower regions and layered dust concentrations in greater depths.

The optical properties of polar ice were measured in detail with the help of steady and pulsed light sources deployed together with detector components by the Amanda collaboration. The techniques and results are comprehensively described in [A$^{+}$06b] and a brief overview over optical properties relevant for neutrino searches with IceCube is given in the following paragraphs.

### Scattering

Photon scattering is the dominant complication for muon track reconstruction based on measurements with photo-multipliers in ice. The geometric scattering length, referred to on page 30, is defined as the mean distance between two photon scatters. Early measurements at the South Pole in a depth of 0.8 to 1 km showed it to be very small (around 10 to 20 cm) due to residual air trapped in bubbles [A$^+$97a]. The increasing pressure at greater depths, though, transforms these bubbles into non-scattering air hydrates, resulting in bubble-free ice below $\sim 1.5$ km [PWC00].

Due to these findings, IceCube extends from a depth of 1.5 km downward, where scattering occurs primarily at micron-sized dust grains. Here, light is not scattered isotropically but predominantly in the forward direction. Based on dust compositions from Antarctic ice core measurements, Mie theory was used in [A$^+$06b] to derive the mean cosine of the scattering angle: $\langle\cos\theta\rangle = 0.94$. The equality between the mean cosine after $k$ scatterings with angle $\theta$ each and the mean of one scattering to the power of $k$,

$$\langle\cos\theta\rangle_k = \langle\cos\theta\rangle^k \, , \tag{4.1}$$

is stated in [Kir99] as a general relation. Based on this an effective scattering length $\lambda_e$ can be defined. Considering many successive steps $n$ of light transport without absorption over the scattering length $\lambda_s$, the sum over the projection of each step onto the initial direction is given by

$$\lambda_e = \lambda_s \sum_{i=0}^{n} \langle\cos\theta\rangle^i \, , \tag{4.2}$$

which for large $n$ leads to

$$\lambda_e = \frac{\lambda_s}{1 - \langle\cos\theta\rangle} \, . \tag{4.3}$$

The effective scattering coefficient is the inverse of $\lambda_e$. As shown in the left plot in Fig. 4.1, its wavelength dependence is rather small and can be neglected when compared to the strong depth dependence. A device called *dust logger* was lowered into some IceCube deployment holes, to measure the scattering length with a spatial resolution of $< 1$ cm [BBW$^+$05]. The comparison to AMANDA measurements in Fig. 4.2 shows excellent agreement between the two approaches and identifies four major peaks of dust concentration below 1.5 km. The strongest scattering occurs between 2.0 and 2.1 km in dust layer 'D'. It has a major impact on Cherenkov light detection at this depth, visible for example in Fig. 6.15 on page 88. Below this layer, the average amount of impurities is much lower than above it and the scattering lengths reaches values around 50 m.

IceCube photo-multipliers are deployed by using hot water to melt holes of

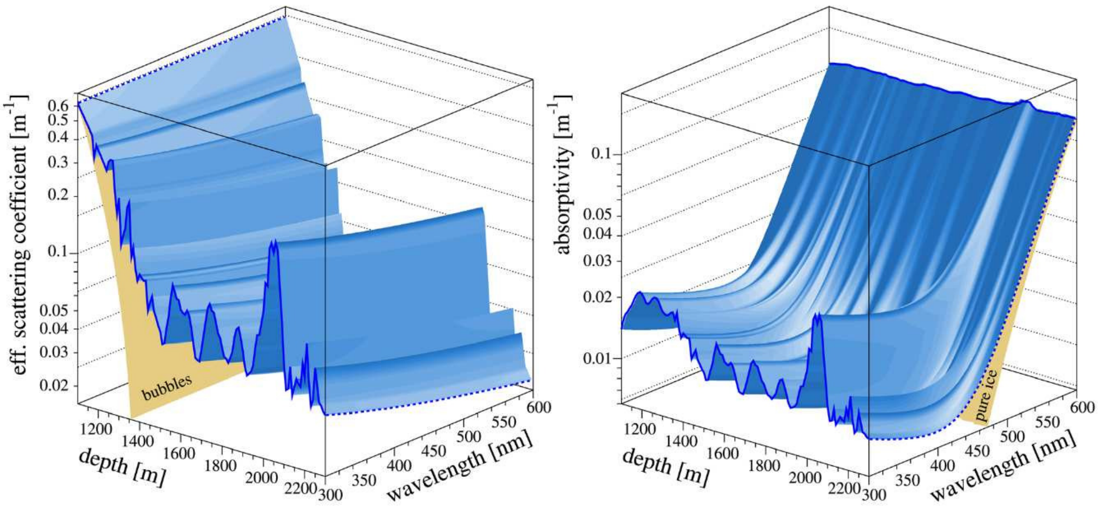

Figure 4.1.: Optical scattering and absorption properties of the ice deep inside the South Pole glacier, in dependence of depth and wavelength. Plot taken from [A$^+$06b].

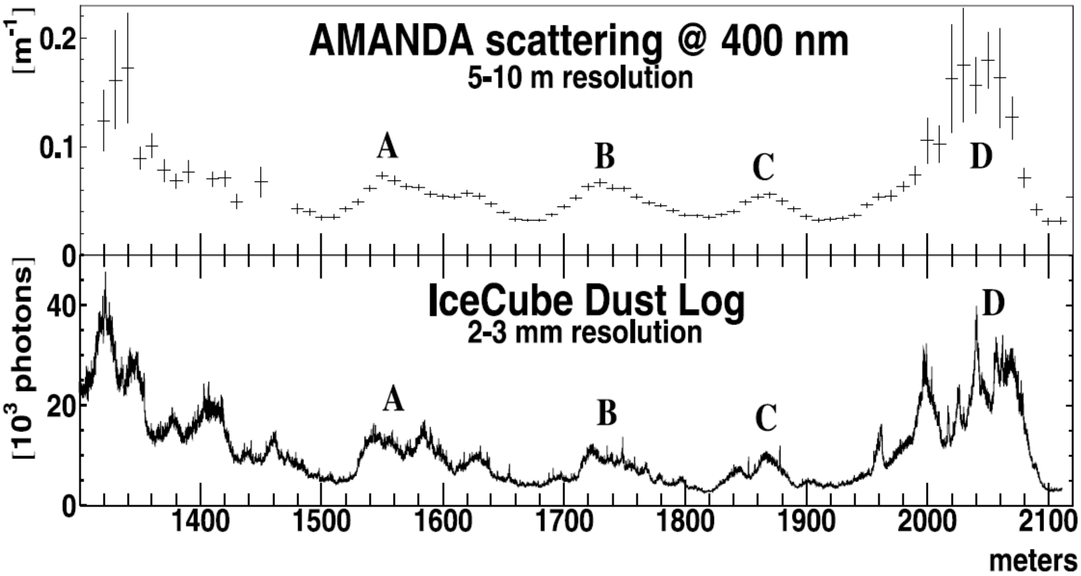

Figure 4.2.: Effective scattering coefficients (upper graph) in the South Pole ice in comparison to dust concentrations measured with the *dust logger* (lower graph) in dependence of depth. Plot taken from [BBW$^+$05].

2.4 km depth. The refreezing causes conditions inside these holes which are probably not as good as in the surrounding medium, for example due to bubbles that solidify only slowly. To allow further studies with artificial light emitters, IceCube optical modules are equipped with flasher-boards, see section 4.1.3. A calibrated light source called *standard candle* has also been deployed [K$^+$07].

### Absorption

The absorption length $\lambda_a$ is defined as the distance over which the survival probability of a photon travelling through matter is reduced to $1/e$. Its reciprocal, the absorption coefficient or absorptivity, is shown in the right plot of Fig. 4.1 for measurements in the deep polar ice.

In [A$^+$06b], a three-component parametrisation identifies three wavelength regimes. Below 200 nm, an exponential decrease of absorptivity is caused by an electronic band gap in ice crystals, while excitation of the molecules leads to an exponential rise above 500 nm. Absorption in the intermediate regime is very low and dominated by impurities from dust. Consequently, the depth dependence of absorptivity follows very closely that of the scattering coefficient, highlighting the same dust layers. The rise with bubble concentration towards the surface is not observed since the enclosed air does not absorb but only scatter photons.

## 4.1.2. Detector structure

### IceCube

IceCube is a high energy energy neutrino Observatory, extending over a volume of one cubic kilometer when completed. It is currently under construction near the Amundsen-Scott South Pole station in Antarctica. The main detector component is called Digital Optical Module (DOM) and houses a photo-multiplier for the detection of Cherenkov light. DOMs are arranged on vertical strings and deployed at depths between 1450 and 2450 m that are reached by using hot pressurised water to drill holes. These remain unfrozen long enough to lower the equipment. Each string holds 60 DOMs with a uniform vertical separation of 17 m. A total of 80 strings is planned, arranged on a hexagonal pattern, see Fig. 4.3, with a grid point separation of 125 m in the horizontal direction.

With an energy threshold of 100 GeV, the IceCube experiment is optimised to detect neutrinos of cosmological origin within the TeV to PeV energy range [A$^+$06f]. Primary search channels rely on the identification of muon tracks produced by neutrinos in charged-current interactions and the detection of cascade-like events from neutrino-induced particle showers. The study of atmospheric muon and neutrino fluxes is crucial, both for understanding the background of other analyses and to search for effects of new physics. Various other research topics related to particle physics include the detection of a muon flux produced

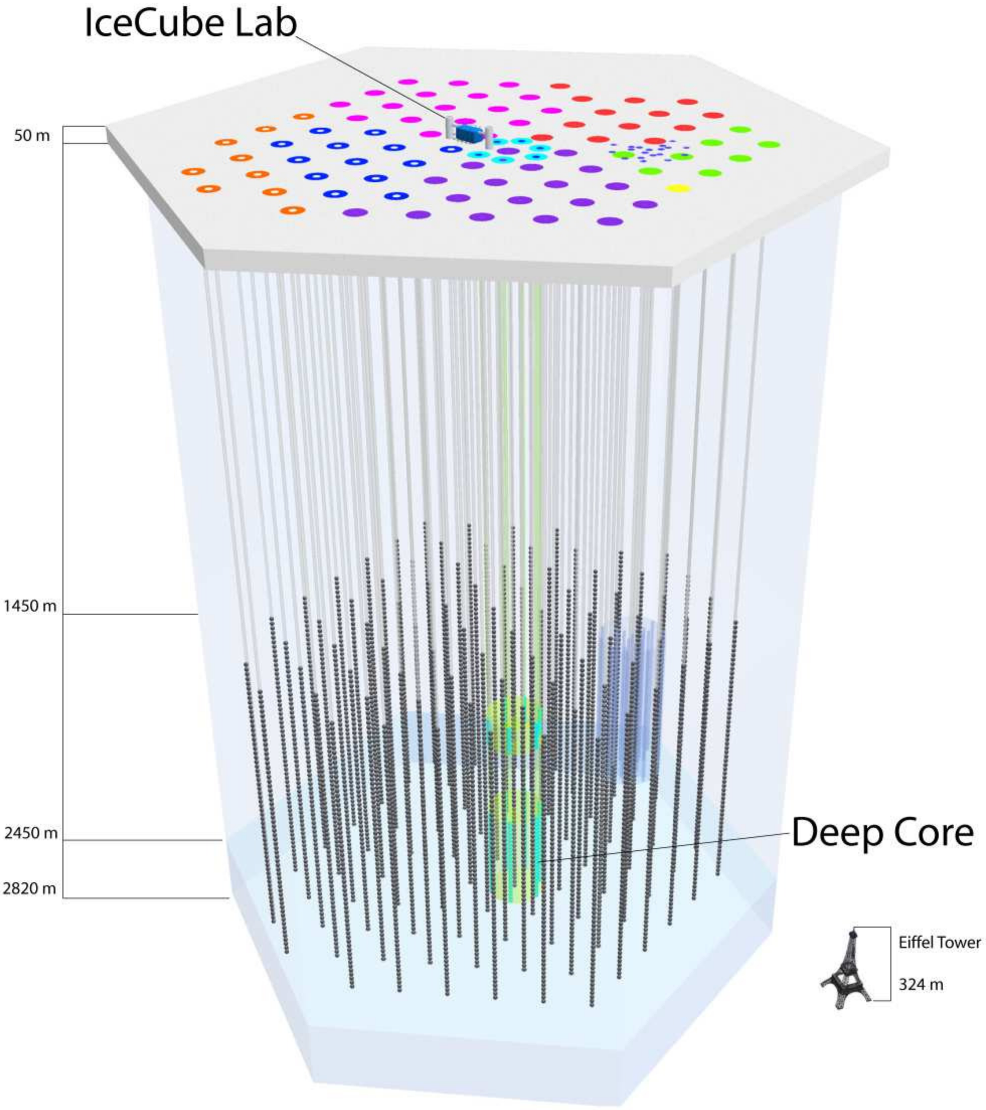

Figure 4.3.: Schematic view of the IceCube Observatory, including in-ice strings, the Deep Core sub-array and the IceTop stations. Colours indicate the (planned) times of deployment. The 59 strings and IceTop stations installed until and including the polar season 2008/2009 comprise, in chronological order, the spots marked in yellow, green, red, magenta and violet.

by dark matter annihilations inside the Sun or Earth or the detection of exotic particles like magnetic monopoles.

### Deep Core

A sub-array with denser DOM spacing called Deep Core was designed to replace Amanda as an embedded detector with a lower energy threshold [Wie09]. It consists of six additional strings, arranged around the central IceCube string in a hexagon with a horizontal spacing of 72 m. The Deep Core strings hold 60 DOMs, of which ten are located in depths between 1750 and 1850 m to serve as veto layer against down-going atmospheric muons. The major dust layer and the clearer ice below it, described in section 4.1.1, motivated the positioning of the other 50 DOMs at greater depths between 2100 and 2450 m with a vertical spacing of 7 m.

Deep Core will make it possible to observe neutrinos from sources in the Southern hemisphere at lower energies than the analysis discussed in this thesis. This is achieved by employing IceCube DOMs as a veto, reducing the need for suppressing atmospheric events through hard energy cuts. Furthermore, WIMP searches and the study of neutrino oscillations profit from the lower energy threshold related to the short inter-DOM distances.

### IceTop

Located in the snow just below the surface above the IceCube neutrino telescope is the IceTop air shower array. The detector components are arranged in tanks of 1.8 m diameter, filled with ice which is frozen in a process that avoids the formation of air bubbles. Each tank is instrumented with two DOMs, operated at different gains to increase the dynamic range. Two tanks with a separation of 10 m form a station, which is located next to each IceCube string.

IceTop is designed to detect secondary particles from extended air showers initiated by charged cosmic rays in the upper atmosphere. Coincident measurements of the particles at the surface and highly energetic muons penetrating to the IceCube DOMs in the deep ice allow conclusions about the primary cosmic ray composition. In particular the part of the spectrum around the knee, see section 2.1.1, with the assumed transition from galactic to extra-galactic origins is covered by the IceTop range of sensitivity from approximately 300 TeV to 1 EeV.

### Construction Progress

Before the beginning of the 09/10 deployment season, the in-ice part of IceCube consisted of 58 standard strings and one Deep Core string, comprising a total of 3540 DOMs. 59 IceTop stations were installed at the surface. The IceCube Laboratory was completed in 2007, a building at the surface in the centre of the IceCube area where all cables from the three sub-detectors converge and which houses the computing equipment. The deployment of new strings and tanks is only possible during the austral summer months. Completion of the full array of 86 strings and 80 surface stations is foreseen for early 2011.

### 4.1.3. Data acquisition

#### Overview

The IceCube data acquisition (DAQ) can be characterised as a system to capture and timestamp, with high accuracy, an optical signal registered with a PMT. Listed below are the components which are part of the chain to generate time-calibrated digital event records, as described in [A$^+$09f] and [Voi08]:

- The DOMs, situated in the ice to record and digitise light pulses.
- The DOMHub, a computer in the IceCube Laboratory that communicates with all DOMs.
- The Cable Network, connecting DOMs with each other and with the DOMHub.
- The Master Clock, which distributes a time signal derived from a GPS receiver.
- The Stringhub, a software that sorts the signals from DOMs on the same string and synchronises their clocks with the universal time.
- The trigger subsystems, grouping the signals according to time and different trigger conditions.
- The event builder and filter software, which combines signals to coherent events and sorts these according to various filter settings.

In the following paragraphs, only some central aspects of the above components that are relevant for the discussion of data analysis in this thesis are described in more detail.

#### Digital Optical Modules

A DOM, depicted schematically in Fig. 4.4, contains a HAMAMATSU R7081-02 PMT with a spherical photocathode, 25 cm in diameter, and 10 dynodes. At -40° C, the noise rate is only 200-300 Hz and the maximum quantum efficiency approximately 25%[1]. The PMT fills the lower part of the 13 mm thick glass sphere and is embedded in a Room Temperature Vulcanisation (RTV) gel for optical coupling and mechanical support. A mu-metal wire cage provides shielding

---

[1] The PMTs in the DOMs deployed on the Deep Core strings are the same type, except for a modified cathode material which improves the quantum efficiency to $\sim 33\%$ [Wie09].

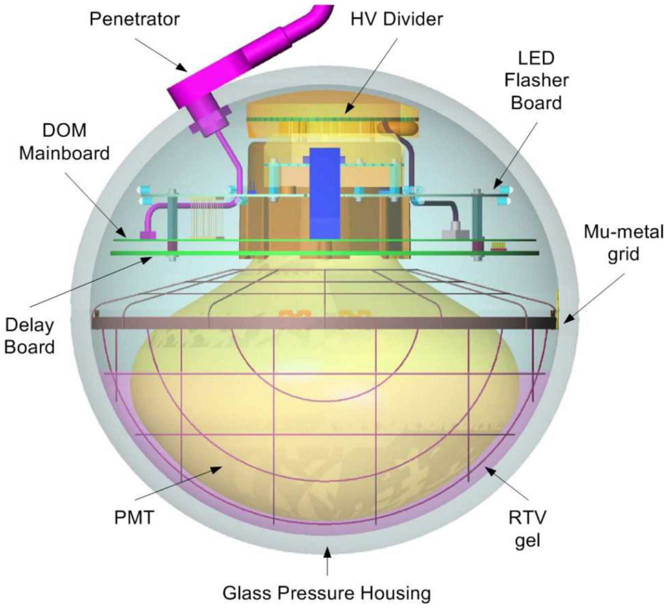

Figure 4.4.: Schematic view of a Digital Optical Module (DOM) with its main components.

against the magnetic field of the Earth. Surrounding the upper part of the PMT are a delay board and the DOM mainboard. The flasher board on top of it houses twelve powerful Light Emitting Diodes (LED), which can produce light pulses with $10^9$ photons per pulse and are arranged in a way to simulate the Cherenkov light pattern of cascade-like showers. A 2 kV high voltage generator and a passive base for distribution of the voltage to anode and dynodes are situated on top of the PMT.

The analog signal, a waveform of registered photon pulses, is directed into three paths on the DOM mainboard. The first leads to a discriminator which is responsible for the self-triggering of the readout, given a signal which has a pre-defined strength. This threshold is set to 0.25 photo-electrons (pe), with 1 pe corresponding to the average charge produced by a single photon in the PMT.

The second path is fed into the main digitisation components, two Analog Transient Waveform Digitisers (ATWDs). Each has three channels, operated at different amplifications. An ATWD is a switched capacitor array with an analog memory for 128 samples. The sampling rate is currently set to 3.3 ns/sample, thus providing in total 420 ns of memory for which the charges are digitised by 128 ADCs. Both ATWDs operate together in a way that during readout, which can take up to 100 $\mu$s, the inactive one can react to a new trigger to minimise dead time. To allow for longer recording times, the third signal path is fed into a (fast) ADC (fADC) with a sampling rate of 25 ns/sample over a time of up to 6.4 $\mu$s.

DOMs can communicate with their adjacent neighbours (up and down) by sending digital signals in case of a trigger. Receivers on the mainboard feed these signals into the trigger logic and relay them further to the next DOM. The system can be configured to forward recorded waveforms only to the DOMHub if a certain coincidence requirement is met, called *local coincidence*. With the settings in place during data taking for the analysis in this work, at least one of the two next neighbours up and down[2] is required to have photon hits within a time window of 1 $\mu$s. This requirement is meant to favour causally connected photon signals, thus reducing noise hits which occur randomly in individual DOMs. If the local coincidence condition is fulfilled, the digitised signal is sent to the surface via a direct connection with the DOMHub. The local clock of the DOM provides a timestamp and is calibrated through a timing packet exchange with the Master Clock.

### Trigger and Filter

Currently, several trigger settings are used simultaneously in IceCube, designed for various types of analyses which rely on different energy regimes and event topologies. For the analyses described in this thesis, only data from the main Simple Multiplicity Trigger (SMT) were considered. This trigger requires that at least 8 in-ice DOMs have detected photon hits within 10 $\mu$s, taking into account the local coincidence condition mentioned above.

The full data of all triggered events is stored at South Pole and becomes only available for analysis after data tapes have been transported via ship to the North. However, for most analyses it is sufficient to use data which has been reduced through on-line filters running at pole and is transmitted daily via satellites to the North. The requirements for events to pass the individual filters are very different and often depend on multiple variables, designed according to various analysis goals. The total data volume grew from ~35 Gigabytes (GB) per day in 2008 to ~48 GB/day in 2009. The filter conditions for data from 2007/2008, used in this work, are discussed in chapter 6.

## 4.2. Neutrino event simulation

The accurate simulation of neutrino signals and their detection signatures in the IceCube neutrino telescope is crucial for a point source analysis. Tests of reconstruction algorithms, like those presented in chapter 5, often rely on the possibility to compare the processed results with the original event parameters, stored during generation. Furthermore, final event rates in the detector can be converted to neutrino fluxes based on the known relations for injected fluxes of simulated

---

[2] The logic recognises cases where the upper or lower end of a string are within this span and excludes dead or malfunctioning DOMs, if they are registered in the system.

neutrinos. In chapter 6, the selection of a suitable event sample is discussed and the optimisation of the efficiency relies also on a simulated signal flux.

Neutrino simulations used in this work were produced in a centralised effort by the IceCube collaboration. The production can be divided into several parts, implemented as separate software projects:

1. Monte Carlo generation of neutrinos (of all flavours) and their propagation and interaction within the programme *Neutrino Generator*;
2. Propagation of muons (or taus) through matter by the programme *MMC*;
3. Photon tracking from a light source through the ice with the programme *Photonics*;
4. Simulation of the full detector response from the PMT to the resulting digital signals and finally the trigger implementation.

### Neutrino Generation

The programme *Neutrino Generator* provides the incoming muon flux and the simulation of interactions in the ice or the bedrock near the detector. It is based on the programme *Anis* [KA03]. Relevant for this work is the simulation of muon neutrino primaries, which are generated with energy values according to an $E^{-1}$ power law spectrum. In the standard Monte Carlo production, neutrinos are injected from directions that are isotropic in the azimuth angle and can be limited to a certain zenith angle range. The tracks start at the surface of Earth and are propagated towards the detector.

In view of the small neutrino cross sections, an interaction in a certain volume around the detector is enforced in the simulation. Every neutrino produces either a neutral or a charged current interaction. These do not necessarily lead to a triggered event, though. This strong oversampling of interaction rates is accounted for by assigning an interaction weight to each event, following the cross sections discussed in section 3.1.2. The stored weights allow to rescale the number of detected events. The interaction volume for the simulated neutrino data used in this analysis is a cylinder spanning 1.7 km in height and 1.2 km in radius, centred around the core of the 22-strings configuration. Its zenith angle orientation is rotated according to the generated incoming angle of a neutrino to provide always the same injection area, see Fig. 4.5.

All weights which are required to normalise simulated event counts to a given flux value and spectrum are combined in a single parameter for each event. This value called *OneWeight* represents an incoming flux of one neutrino per GeV, second, $\mathrm{cm}^2$ and steradian, taking into account the generated spectrum, track orientation and injection area. By multiplying it with a desired spectrum, for example an $E^{-\gamma}$ power law, flux normalisation factor and observation time and

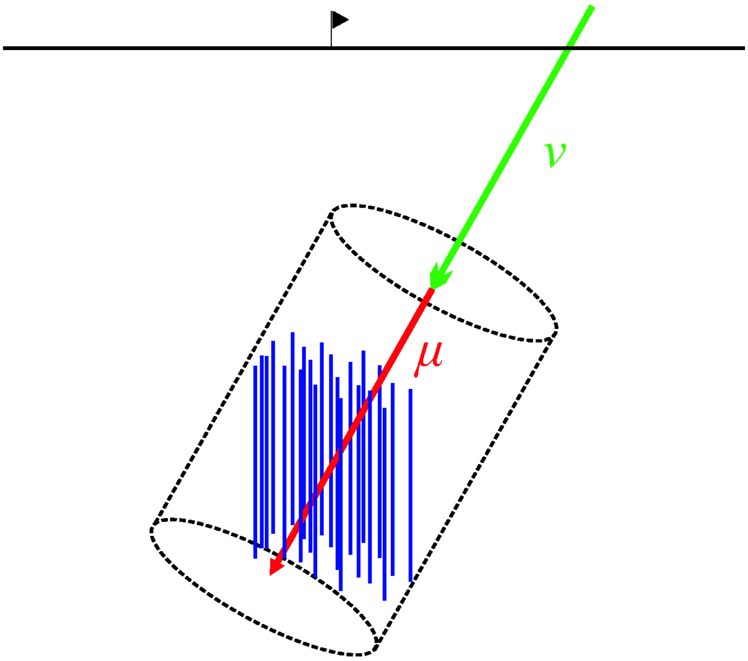

Figure 4.5.: Illustration of the interaction volume simulated in *Neutrino Generator* around IceCube.

dividing it by the total number of injected neutrinos in the sample, one obtains the absolute weight for the event.

### Muon propagation

The muon path through the ice or bedrock is implemented in the propagation code *MMC* [CR04]. Energy loss and light emission occur through the various effects described in section 3.1.3. These processes are stochastic in nature and can be treated as such by making use of Monte Carlo methods in *MMC*. Since the probability for separate energy loss events diverges when the muon energy approaches zero, a lower cut is implemented, below which energy losses are simulated in a continuous way. The full electro-magnetic or hadronic shower components and their Cherenkov emissions are only simulated if the muon, or a secondary particle, has an energy above this threshold when the energy loss occurs.

### Photon propagation in the ice

In section 4.1.1, the inhomogeneous ice structure and the depth- and wavelength-dependent scattering and absorption features of the polar glacier were introduced. It is impossible to individually trace the more than $10^7$ photons from a bright muon track within the range of the detector through a model of this medium as a regular processing step, due to computing limitations. Instead, IceCube simulations use pre-calculated tables for the mean number of photons per track length and the arrival time distribution in the DOM for a given Cherenkov light source.

These tables are generated with the programme *Photonics* [L$^+$07]. Since the ice structure can be described as a system of layers with different absorption and scattering properties, it is implemented as a model with constant parameters in the x-y-plane, featuring only a depth-dependence. The parametrisation for photon tracing between a given source location (on a muon track) and a DOM is defined by the track zenith angle, three parameters to describe the position of the DOM relative to the track origin and the depth of the DOM. Following a Poisson distribution, the expected number of photons at each DOM is calculated as a function of these parameters. The arrival time distribution for the hits depends, in addition to the geometrical parametrisation, on the residual time. This is defined as the difference between the expected time of arrival without scattering and the true delayed time and is provided as a pre-calculated distribution.

The *Photonics* simulation furthermore accounts for the hole ice properties by an increased scattering coefficient. Included are also the absorption effects of the glass and gel layers of the DOM and the quantum efficiency of the PMT, all depending on the incoming angle of the photons.

### Detector simulation

The simulation of the IceCube detector hardware and software is designed to translate the photon pulses in a DOM into an event readout with the same format as that of a real event record. The process is divided into separate modules within the simulation project of the IceCube software framework. The photon pattern from *Photonics* is first translated into a series of hits in the PMT and noise hits are added. The PMT response is simulated and passed on to a software module which accurately reproduces the effects of digitisation and processing of signals on the DOM mainboard. Finally, a trigger simulation produces an event output that can be processed further with the same filter and analysis software as used for actual data.

# Chapter 5.

# Reconstruction of neutrino events

Any neutrino analysis in IceCube relies on the possibility to reconstruct the event properties from the Cherenkov photon distribution, recorded with the detector modules. For a point source search, the quality of the direction reconstruction is a crucial measure. Both the reconstruction techniques and the performance with respect to an analysis dedicated to energies at the PeV scale form the central topic of this chapter. The section at the end of the chapter introduces an approach to muon energy reconstruction.

## 5.1. Basic event characteristics

### 5.1.1. Waveform pulse extraction

A digitised waveform, produced in each DOM for a detected event, is the record of the charge and arrival time of at least one photon hit. In general it includes a series of many, possibly overlapping, pulses with individual charges. To allow an interpretation and reconstruction of these waveforms, a standardised but flexible software for extracting information on charges and leading edge times of pulses is used in IceCube. The programme *FeatureExtractor* performs this task by determining a baseline in each waveform, fitting pulses to the binned charge distribution and merging the records from ATWD and fADC, see section 4.1.3. *FeatureExtractor* depends on the output of a preceding programme, the *DOM-Calibrator*, which performs the combination of the three ATWD channels with their different gains into a single, calibrated waveform. It relies on a database of calibration records for the individual DOM responses.

Implemented in *FeatureExtractor* are several options and algorithms for fitting a single pulse or multiple pulses per waveform. In the following, only settings relevant for the analysis described in the next chapters are presented.

The baseline of a of a DOM output is estimated from the mean charge of the first three of the 128 ATWD bins. Ideally it should be zero after the calibration, but it may be affected by transient phenomena in the recording circuit that could lead to problems with the definition of a leading edge time and are thus corrected. In addition, *FeatureExtractor* has an ADC threshold setting which is expressed in

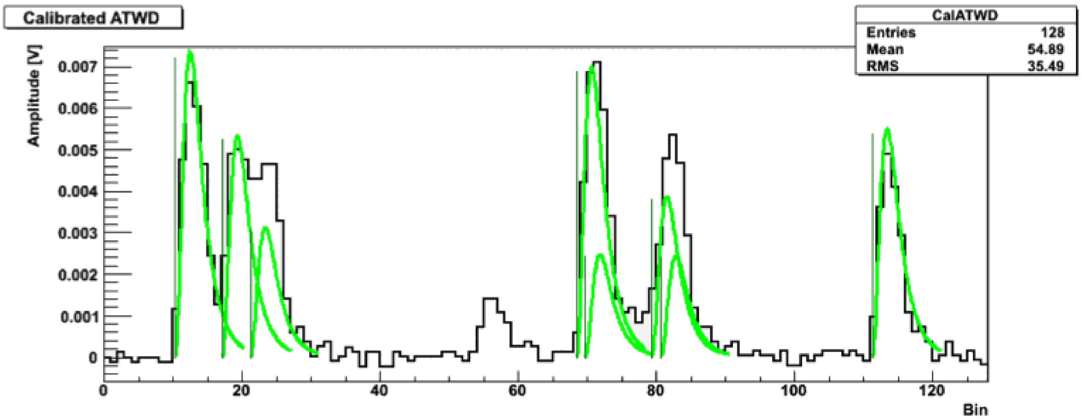

Figure 5.1.: Example of an ATWD waveform with *FeatureExtractor* pulse fits indicated in green.

units of the discriminator threshold to adapt to differences between the DOMs. Only charges above this threshold are counted, and waveform fluctuations with lower amplitudes are not fitted as pulses. For the data taking with 22 strings (IC-22, 2007/2008), the on-line feature-extraction at South Pole was done with a threshold of 0.4, but then raised to 1.0 for the processing of all filtered data in the North. The larger value removes more small pulses, mostly related to noise, and provides more stable results for high energy track reconstructions.

Due to the limited CPU time for on-line processing, only one pulse per waveform was extracted at pole for the IC-22 runs. A pulse is determined by the first waveform maximum with a charge above the threshold. Its leading edge time is defined by finding the maximum slope between two bins before this peak and then extrapolating linearly backwards to the intersection with the baseline.

In the off-line processing of all transmitted data from the various filters, *FeatureExtractor* is set to fit multiple pulses per waveform. The method is based on a pulse template function that is used to iteratively fit each waveform peak with a procedure called Bayesian unfolding [D'A95, Cow02]. The final feature-extracted pulse series is a combination of these often overlapping template pulses with their individual leading edge times, see Fig 5.1 for an example. The pulses have individual amplitudes, and the summed charge over the full waveform is distributed according to these amplitudes to obtain a charge for each pulse.

Feature extraction in the coarser binned fADC is treated in a simplified way. Basically, the single pulse extraction described above is performed for all successive peaks in the fADC record, with a higher threshold set to 5.0 times the discriminator value of the DOM. The combined output for ATWD and fADC is a series of pulses, each with a leading edge time relative to the recorded trigger time and a charge measured in photo-electrons.

### 5.1.2. First guess track fit

The likelihood reconstruction algorithms discussed in the next section need a so-called seed with a first guess for the track direction to allow a fast convergence to the best fit. Furthermore, many filter implementations running at the pole rely on estimates of the event zenith angle to adapt cuts to the varying background flux mentioned in section 3.1.4. In both cases it is useful to have a simple and fast algorithm that provides a first track fit. Several approaches for this task have been developed for AMANDA and IceCube, see [A$^+$04c].

One of the simplest of these first guess reconstructions is called *linefit* and is the only one relevant for later discussions in this thesis. The method ignores the fact that photons from the track or close secondaries are emitted along a Cherenkov cone and neither does it take into account any ice properties. The track is simply fitted as a straight line along which light travels with a velocity $\vec{v}$. To determine the orientation, expressed in the vector $\vec{v}$, and a vertex point $\vec{r}$ at the beginning of the track, the $\chi^2$ of the distances to the $N$ DOM positions $\vec{r}_i$ at the times $t_i$ of first photon hits[1] has to be minimised:

$$\chi^2 = \sum_{i=1}^{N} (\vec{r}_i - \vec{r} - \vec{v} \cdot t_i)^2 \,. \tag{5.1}$$

The minimisation is performed by differentiation with respect to $\vec{r}$ and $\vec{v}$ as the free parameters. The analytic solution is given in [A$^+$04c]. The normalised velocity $\vec{v}/|\vec{v}|$ yields the orientation of the track and thus the zenith angle:

$$\theta_{LF} = -\arccos\left(\frac{v_z}{|\vec{v}|}\right) \,. \tag{5.2}$$

The absolute value $|\vec{v}|$ of the *linefit* velocity is a mean speed of light signals projected onto the 1-dimensional track. It is small for cascade-like events (spherical) or high energy muon tracks (with many showers along the track) but large for low energy single muons.

## 5.2. Likelihood reconstruction

### 5.2.1. Parametrisation

#### Track parameters

The reconstructions described in the following are based on the simplified assumption of an infinitely long muon track with velocity $\beta = v/c = 1$, emitting photons

---

[1] In the on-line processing, the leading edge time of the single pulse fit from *FeatureExtractor* is used, see section 5.1.1.

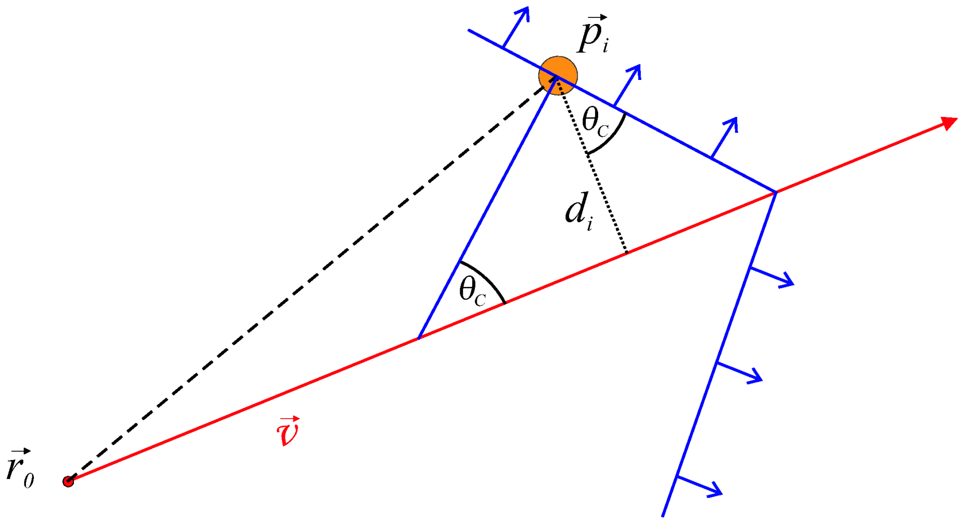

Figure 5.2.: Illustration of track parameters with respect to a muon, travelling in the direction of $\vec{v}$ and emitting photons in a Cherenkov cone. A DOM is located at $\vec{p}_i$.

that form a Cherenkov cone. The geometrical parameters required to describe the position of a DOM relative to such a track are illustrated in Figure 5.2. Since the velocity is fixed, a total of five variables suffices: Three for the muon position $\vec{r}$ at a given time $t_0$ and two for the track orientation, normally expressed via the angles $\theta$ (zenith) and $\phi$ (azimuth) of the velocity vector $\vec{v}$. Depending on the implementation, it might be convenient to use another set of parameters, for example including the perpendicular distance $d_i$ from the track to a DOM at position $\vec{p}_i$. In the following, any such set of track parameters is represented by the 5-dimensional vector $\vec{a}$.

A reconstruction algorithm can find a track fit by maximising the likelihood function

$$\mathcal{L}(\vec{x}|\vec{a}) = \prod_i p(\vec{x}_i|\vec{a}) \,, \tag{5.3}$$

with respect to the parameters $\vec{a}$. The probability density function (p.d.f.) $p(\vec{x}_i|\vec{a})$ describes the probability for a given observation $\vec{x}_i$, i.e. photon hits in DOM $i$, to occur under the track hypothesis $\vec{a}$.

A detailed discussion of likelihood reconstruction in Amanda is presented in [A$^+$04c]. The following sections provide an overview over the relevant details, which are implemented for application in IceCube within the *Gulliver* module as part of the IceCube software framework.

### Residual time

In a simple ansatz, one observation $\vec{x}_i$ is only characterised by the arrival time of one photon in a DOM and the position $\vec{p}_i$ of the latter. To compare this to a simple geometrical expectation, the parameters from Fig. 5.2 can be used to express the detection time at $\vec{p}_i$ for a Cherenkov emission from a muon track as:

$$t_{geo,i} = t_0 + \frac{(\vec{v}/v) \cdot (\vec{p}_i - \vec{r}_0) + d_i \tan(\theta_C)}{c} . \tag{5.4}$$

The muon is at position $\vec{r}_0$ at time $t_0$ and travels along the normalised direction vector $\vec{v}/v$. It is convenient to define the residual time $t_{res}$ as the difference between the measured arrival time $t_{hit}$ and the expectation,

$$t_{res} = t_{hit} - t_{geo} , \tag{5.5}$$

since scattering in the ice delays photons with respect to the Cherenkov cone assumption. Related to this, the DOM orientation relative to the track has also to be taken into account, due to the fact that a photomultiplier fills only the lower half of a DOM. It is possible to modify the definition of the distance $d_i$ of closest approach between track and DOM to incorporate this angular dependence of the acceptance, transforming it into an effective length. The parametrisation is given in [Ack06].

In general, many additional photons do not follow the Cherenkov cone but originate in particle showers along the track and thus arrive later. Noise hits, deviations from the track topology, as in the case of a bundle of multiple muons, and the PMT jitter can lead to negative residual times. In the time likelihood,

$$\mathcal{L}_{time}(x|\vec{a}) = \prod_i p(t_{res,i}, d_i|\vec{a}) , \tag{5.6}$$

the residual time values closest to zero must have the largest weight for the optimal track fit, based on the assumption that they are the least scattered and hence form a Cherenkov cone.

## 5.2.2. Probability density functions

### Pandel function

An analytic expression used for the p.d.f. with respect to residual time $t_{res}$ and distance to the track $d$, called Pandel function, was developed in [Pan96]:

$$p(t_{res}, d) = \frac{1}{N(d)} \frac{\tau^{-d/\lambda} \cdot t_{res}^{d/\lambda - 1}}{\Gamma(d/\lambda)} \cdot \exp - \left( t_{res} \cdot \left( \frac{1}{\tau} + \frac{c_{med}}{\lambda_a} \right) + \frac{d}{\lambda_a} \right) . \tag{5.7}$$

The normalisation is given by

$$N(d) = e^{-d/\lambda} \cdot \left(1 + \frac{\tau \cdot c_{med}}{\lambda_a}\right)^{-d/\lambda} . \tag{5.8}$$

The free parameters $\tau$ and $\lambda$ were determined empirically with Monte Carlo simulations, incorporating the average ice properties in a constant way. The absorption length $\lambda_a$ is kept at an average value in the IceCube reconstructions discussed here. $c_{med} = c/n$ is the phase velocity of light in ice.

The Pandel function is normalised and easy to compute, but it has the disadvantage that it is not defined for negative residual times and features a pole at zero which can lead to numerical problems. One solution is to convolute it with a Gaussian function around zero, representing the PMT jitter. The width of this Gaussian was set to 15 ns for the processing of IC-22 data. This is larger than the average jitter value of $\sim 4$ ns, but it is a reasonable conservative estimate considering other effects like noise hits and deviations from the fixed Pandel parameters for the ice.

While originally developed for the case of an isotropic, monochromatic and point-like light source, the Pandel function, with adapted parameters, performs well for track reconstructions in IceCube. Although depth- and wavelength-dependence of scattering and absorption are not taken into account, the achieved angular resolution is already very good, as discussed in section 5.3.

### Single- and Multi-photoelectron approach

The Pandel function (5.7) can be used directly as a p.d.f. in the time likelihood (5.6) for the case of a single photon per DOM. The direction reconstruction based on this likelihood formulation is called *single-photoelectron* (SPE) and relies only on the first feature-extracted photon pulse, discussed in section 5.1.1, in each waveform. It is used as a robust reconstruction algorithm in AMANDA as well as IceCube analyses.

The SPE approach becomes increasingly inaccurate if the average number of photon hits per DOM is significantly larger then one. In particular at TeV and higher energies, the radiative processes and muon interactions described on page 27 produce a large number of photons. It is therefore more likely that some of these photons arrive after less scatterings and therefore produce an earlier first hit than the average single photon described by the Pandel function.

A slightly more elaborate probability description presented in [A$^+$04c] derives the arrival time distribution of the first of $N$ photons as:

$$p_N^1(t_{res}, d|\vec{a}) = N \cdot p_1(t_{res}, d|\vec{a}) \cdot \left(\int_{t_{res}}^{\infty} p_1(t, d|\vec{a}) dt\right)^{N-1} \tag{5.9}$$

The p.d.f. $p_1$ of a single photon is multiplied with the probability that all other photons arrive at times larger than $t_{res}$, expressed by the integral. Due to individual scattering, each photon can be the one detected first, which results in the factor $N$ for all possible combinations. The approach is called *multi-photoelectron* (MPE) method.

Since feature-extracted pulses can also contain more than one photon hit, $N$ cannot simply be determined by a count of these pulses. In IceCube, $N$ is set equal to the charge in units of photo-electrons (pe), since a single photon pulse has an average charge of 1 pe.

The convolution of the Pandel function with a Gaussian function, the latter representing effects like the PMT jitter, leads to a significant increase of computing time for the integration over the arrival times in the MPE formula. To avoid this, processing of IC-22 data was performed with a simplified approach in which the integration was performed with an unconvoluted Pandel function. The full expression was only used for the function $p_1$ outside the integral in equation (5.9). A more recent implementation allows a faster numerical integration after a transformation of the convoluted Pandel function presented in [JR05] and was used starting with the processing of 40-strings data. Details about the performance of MPE compared to SPE are presented in section 5.3.

### 5.2.3. Iterative minimisation

In order to use standard fitting routines, it is easier to transform the likelihood ansatz from a maximisation problem into a minimisation of $-\log(\mathcal{L})$. In the case of the MPE fit, this leads to:

$$-\ln(\mathcal{L}_{MPE}) = -\sum_{\text{DOMs}} \ln\left( N_i \cdot p_1(t_{res}, d|\vec{a}) \cdot \left( \int_{t_{res}}^{\infty} p_1(t, d|\vec{a}) dt \right)^{N-1} \right) . \qquad (5.10)$$

Inside the IceCube reconstruction software *Gulliver*, the minimisation is performed with *Minuit* [J+94].

The likelihood space defined in this way often has several local minima, also for the SPE approach. An established technique to find the global minimum is the iterative minimisation with new starting conditions in each run. Since a scan of the full parameter space would consume too much CPU time, it is important to have a good first track assumption. This is provided by first guess algorithms like *linefit* from section 5.1.2 or, as was the case for the processing of IC-22 data, by running an SPE fit before the MPE reconstruction.

After the first minimisation, a new zenith-azimuth pair is generated randomly, and along this track orientation, a new starting point $r_0$ is chosen at the position closest to the centre of gravity of all DOMs with hits in the event. The reference time $t_0$ for this point is shifted to avoid negative residual times and thus better fit with the Cherenkov expectation. If the repeated minimisation with this new initial seed yields a better result than the one before, the newly fitted track parameters are stored. The procedure is repeated a pre-defined number of times to allow convergence to the global minimum.

### 5.2.4. Bayesian likelihood

The likelihood formulation discussed above can be extended by incorporating information about the zenith distribution of tracks from atmospheric muons, the dominating background introduced in section 3.1.4. This is achieved by making use of Bayes' Theorem,

$$P(A|B) = \frac{P(B|A)P(A)}{P(B)} \tag{5.11}$$

for the probability that $A$ occurs under condition $B$, see [A$^+$04c]. For the problem of likelihood reconstruction, $A$ represents the track parameter set $\vec{a}$ and $B$ is the observation of photon arrival times in a DOM denoted as $\vec{x}$. Consequently, the probability $P(\vec{a}|\vec{x})$ of a track hypothesis based on the observed photons is maximised by considering the product $P(\vec{x}|\vec{a}) \cdot P(\vec{a})$ .[2] The prior probability $P(\vec{a})$ of a track orientation $\vec{a}$ is given by the distribution of events, which are considered to be exclusively muons from above the horizon. Based on data from other underground experiments and an adaptation of parameters with the help of Monte Carlo simulations, a good description of this additional factor in the likelihood is achieved.

This so-called Bayesian likelihood fit dramatically reduces the number of background muons falsely reconstructed as up-going. The comparison of the negative logarithm of the Bayesian likelihood outcome, referred to as log-likelihood, with that of the standard SPE likelihood fit yields large differences for background muon tracks reconstructed as up-going and can be used to reject them.

### 5.2.5. Angular error estimation

Even if the global minimum is found by iterative maximisation of the negative logarithm of the time likelihood, it does not always correspond to the true track direction. It is therefore helpful to perform a selection of events based on quality parameters which are an estimate of the goodness of the fit. One important parameter of this kind is a measure of the shape near the likelihood minimum, or more precisely the size of the error ellipse in the azimuth-zenith subspace of reconstruction parameters.

A semianalytical method to derive this parameter was developed for AMANDA as described in [Neu06] and is used also in IceCube. From the five coordinates defining a track, only variations in the zenith ($\theta$) and azimuth ($\phi$) angles are

---

[2] $(P(\vec{x}))^{-1}$ is a normalisation factor which becomes irrelevant as a constant in the likelihood function.

relevant for an estimate of the error in orientation. Therefore, the description of the likelihood space around the minimum is reduced, by numerical means, to two parameters. Their correlation, stemming from the location of the reference point, is retained. In the Gaussian approximation for the behaviour of the likelihood, the reduced two-dimensional parameter space forms a paraboloid. An analytical fit is performed to obtain a description of this paraboloid and hence the two angular uncertainties, which define an error ellipse. Conveniently rotating the coordinate systems yields the size of the ellipse that represents a space angle uncertainty for the track fit. This reconstruction parameter is called paraboloid sigma and allows a quality event selection as discussed in section 6.3.2.

## 5.3. Direction reconstruction performance

The SPE and MPE likelihood reconstructions discussed above have to be performed in the North due to large CPU expenses. In the case of IC-22 processing, the less efficient implementation of the MPE-fit made it necessary to reduce the data before performing this reconstruction, which is the topic of section 6.3.1. By running 32 iterations of the SPE fit first and using the result as seed track for MPE, one iteration of minimisation for the latter reconstruction proved to be enough. Repeated fits did not improve the resolution.

The point spread function (PSF) for both SPE and MPE is discussed in the following, based on a configuration of 22 strings. To simplify the comparisons, the performance for a given parameter range is often reduced to one value: the median angular resolution. According to a convention in the IceCube collaboration, it is defined as the median of the distribution of the space angle difference between the true track of a simulated neutrino and the reconstructed muon direction. It thus includes the irreducible uncertainty due to the angle between neutrino and muon, see equation (3.5).

To understand the dependence of the angular resolution on different event parameters, the following study was performed with a sample of simulated neutrinos, selected according to high level criteria for a point source search. Muon neutrinos with energies between 10 to $10^{10}$ GeV were generated and weighted according to $E^{-2}$ and $E^{-1.5}$ spectra. Generally, the angular resolution depends strongly on the cuts applied on track quality parameters. To highlight this, two event selection steps for IC-22 point source searches are compared here. One is called *level 4* and explained in detail in section 6.3.1. Only limited cuts on the track quality were applied at this stage. In contrast, the final event selection, *level 5*, enforces strong requirements on several parameters described in section 6.3.2. A full discussion of these levels is provided in chapter 6 and all parameter thresholds are listed in appendix A. Here, the focus lies only on the general improvements of direction accuracy which are possible with quality cuts. Differences between SPE and MPE are highlighted, as well as their dependence on event topologies.

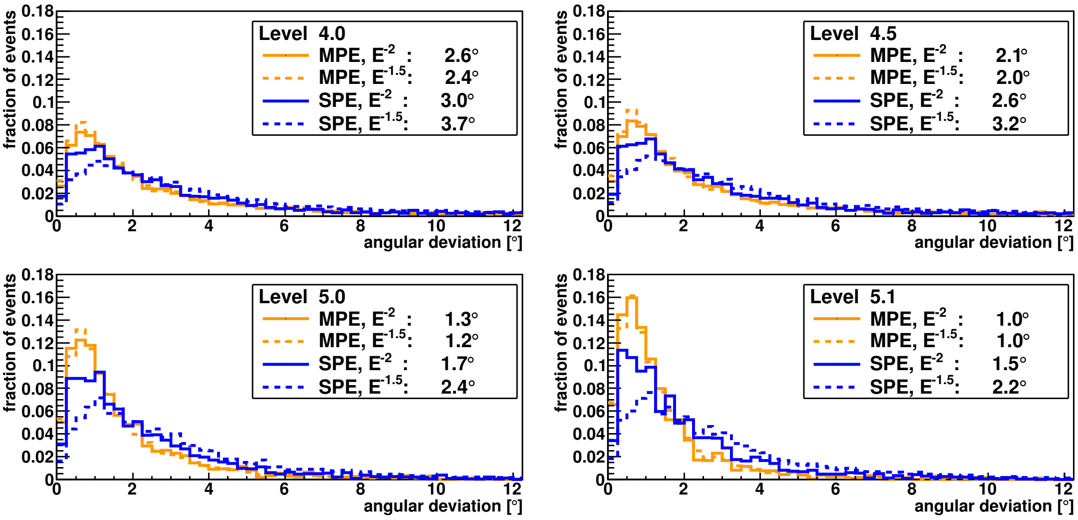

Figure 5.3.: The point spread function given as distributions of angular differences between true and reconstructed tracks for SPE and MPE algorithms with $E^{-2}$ and $E^{-1.5}$ spectra. The cut level rises from the upper left to the lower right panel with increasing quality parameter thresholds, where *level 5.0* is equivalent to the final event selection from chapter 6. In the legend, the angular resolution is given in the form of the median for each histogram.

In Fig. 5.3, the cuts are raised in four steps by linear scaling them from *level 4* to a setting stronger than the final level, denoted as *5.1*. Without considering the individual quality parameters here, the general improvement for both the SPE and MPE algorithm can be observed as a narrowing of the peak of angular differences between the true Monte Carlo track and the reconstructed direction. All histograms are averaged over energy and declination of the events. The lower right panel displays a cut strength which is higher than the one determined by the optimisation for a point source search, but still leads to an improved resolution. This demonstrates the full potential of the reconstructions employed here, but requires a quality selection that reduces the expected signal events too much.

Clearly visible in Fig. 5.3 is that the advantage of MPE over SPE reconstructions becomes more pronounced with stronger cuts, which is apparent when one compares the median angular resolutions given in the legends. The reason for this is that the SPE resolution worsens with energy, while MPE delivers a stable result, as shown in Fig. 5.4. Here the resolution versus energy is compared for levels *4* and *5*. This illustrates how the final level cuts significantly reduce the number of events with large angular deviations at the upper and lower end of the energy scale. The degrading resolution at the highest energies also explains the broadened SPE histograms for an $E^{-1.5}$ power law in Fig. 5.3, due to the larger

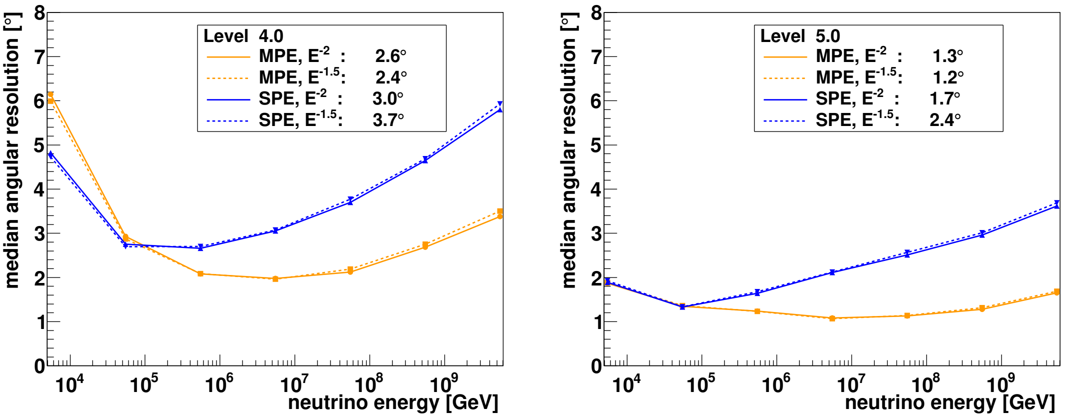

Figure 5.4.: Median angular resolution for SPE and MPE reconstructions as a function of neutrino energy. The event selection applied to the simulated tracks is equal to *level 4* (left) and *level 5* (right) of the IceCube 22-strings point source analysis, with cuts listed in appendix A.

number of these events in a hard spectrum. The PSFs for MPE, on the other hand, show nearly no spectral dependence.

It is of major importance for the point source analysis described in the following chapters that the MPE reconstruction delivers a very good angular resolution of 1.2° to 1.3°, staying flat over a wide range of energies. This makes it possible to search for directional event clustering over the full neutrino spectrum accessible with IceCube.

Related to the energy is the dependence of angular resolution on the number of hit DOMs in an event, called NChannel for number of readout channels. Figure 5.5 shows that the performance of MPE improves for events with larger NChannel values and does not saturate before $\sim 250$ hit DOMs. Other quality cuts at *level 5* lead to better angular resolutions also at lower NChannel values. In the case of SPE, an improvement of the resolution with the number of channels is not observed. The advantage of more degrees of freedom and longer leverages for bright events seems to be irrelevant when multiple hits per DOM are neglected.

The angular resolution as a function of declination[3] of the events is depicted in Fig. 5.6. In the left plot for *level 4*, a minimum around the horizon is visible. It is partially related to the fact that the vertical DOM spacing is only 17 m, compared to 125 m in the horizontal direction, which on average allows a better determination of the z-axis component of a Cherenkov light pattern. The dominance of very high energy events at negative declinations results in a much larger resolution value for down-going events, following the trend already seen in

---

[3] Due to the location of IceCube at South Pole, declination is equivalent to the local zenith angle shifted by $-\pi/2$.

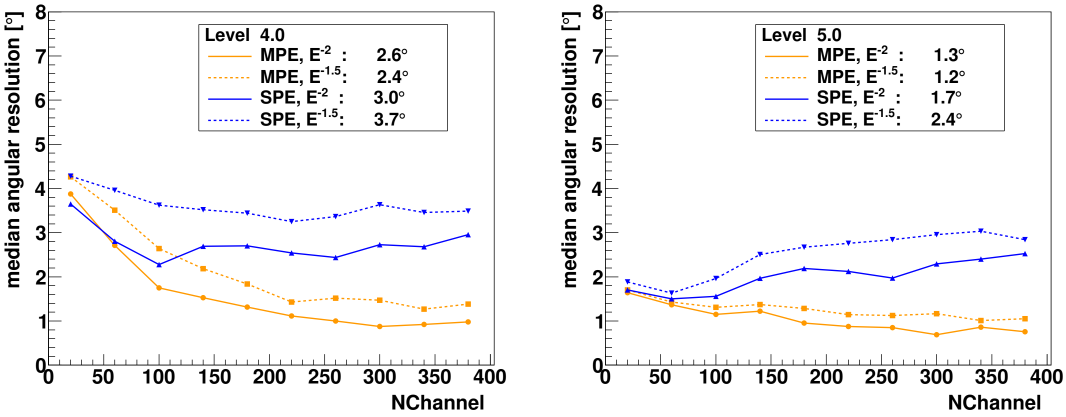

Figure 5.5.: Angular resolution for SPE and MPE reconstructions as a function of number of hit channels (participating DOMs). The event selection applied to the simulated tracks is equal to *level 4* (left) and *level 5* (right) of the IceCube 22-strings point source analysis, with cuts listed in appendix A.

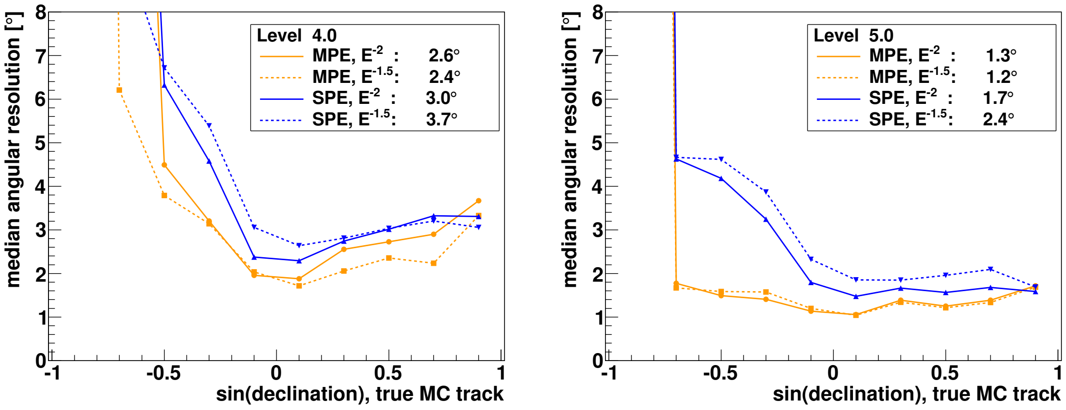

Figure 5.6.: Angular resolution for SPE and MPE reconstructions as a function of sinus of true declination. The event selection applied to the simulated tracks is equal to *level 4* (left) and *level 5* (right) of the IceCube 22-strings point source analysis, with cuts listed in appendix A.

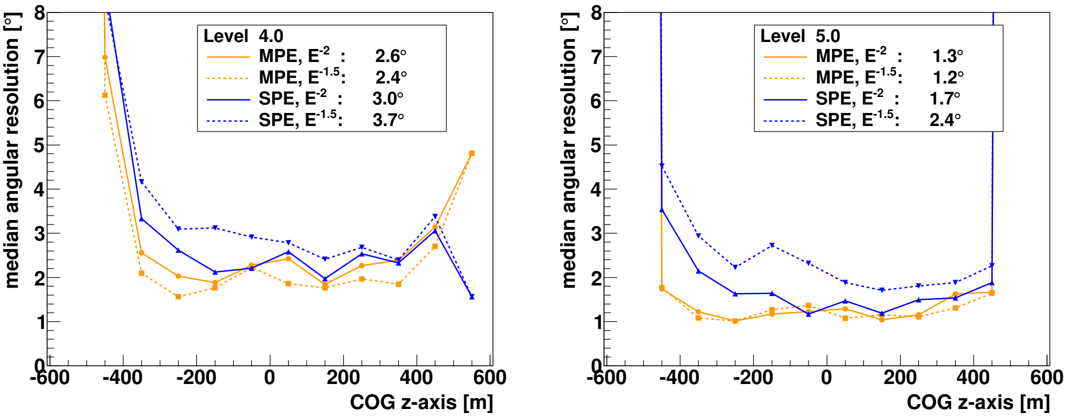

Figure 5.7.: Angular resolution for SPE and MPE reconstructions as a function of the centre of gravity of hits, projected onto the vertical z-axis (COGZ). The event selection applied to the simulated tracks is equal to *level 4* (left) and *level 5* (right) of the IceCube 22-strings point source analysis, with cuts listed in appendix A.

Fig. 5.4. Quality cuts at *level 5* eliminate the declination dependence nearly completely for the MPE reconstruction, partially by removing events which are not well constrained within the detector volume. As discussed above, the drawbacks of the SPE algorithm severely worsen the resolution at high energies and thus at southern declinations, where cuts are designed to select PeV events.

In Fig. 5.7, the angular resolution as a function of the centre of gravity of hit DOMs along the vertical z-axis (COGZ) shows a relatively flat behaviour. At *level 4*, the presence of a certain fraction of events which pass only just above or below the detector volume results in a degrading angular resolutions for very low or high COGZ values. Furthermore, low statistics lead to high uncertainties in these parameter ranges. At *level 5*, the most important feature here is the improvement of MPE over SPE in the lower part of the detector. The clearer ice at this depth, mentioned in section 4.1.1, makes the correct inclusion of later photons via the MPE-likelihood more powerful. Only in the more diffuse upper layers, the simpler SPE-likelihood serves equally well.

## 5.4. Energy reconstruction

An energy reconstruction of muon neutrino events in IceCube is challenging. It relies on the amount of light emitted by a muon and its secondaries during the passage through the detector. The stochastic nature of these processes introduces an inherent uncertainty, as discussed in section 3.1.3. Furthermore, start and end points of the track are unknown or hard to estimate for the majority of events, and additionally the relation between the original neutrino energy and that of the induced muon is not known. Within the scope of this work, muon event energies are reconstructed with a technique described below, but are only used as estimators to provide a basis for adjusting selection cuts.

The energy reconstruction method employed in this work was implemented for IceCube in the programme *Mue*, as described in [Chi08]. The underlying method is a likelihood description which generalises the approach presented in section 5.2.1 to describe $k$ pulses in a given DOM, each comprising a different number of photons $n_i$ while the expectation value of this number due to a given track hypothesis is $\mu_i$:[4]

$$\begin{aligned} -\ln\left(\prod_{\text{DOMs}} P(\{n_i\}|\{\mu_i\})\right) &= -\ln\left(\prod_{\text{DOMs}}\prod_{i=1}^{k}\frac{\mu_i^{n_i}}{n_i!}e^{-\mu_i}\right) \\ &= \sum_{\text{DOMs}}\left(\sum_{i=1}^{k} n_i \ln\frac{\mu_i}{\mu} + \sum_{i=1}^{k}\ln(n_i!) - \ln(N!)\right) \\ &+ \sum_{\text{DOMs}}\left(-N\ln\mu + \mu + \ln(N!)\right) . \end{aligned} \tag{5.12}$$

This comprehensive description of waveforms, composed of pulses with different amplitudes, was presented in [G$^+$07]. The expectation $\mu = \sum_{i=1}^{k}\mu_i$ for the total number of photons in a DOM, the observed total being $N = \sum_{i=1}^{k} n_i$, relies on five track parameters, see section 5.2.1, and a sixth parameter which relates to the total light output of the muon. The latter is the energy proxy one wants to determine. In the formulation described here it represents the total number of Cherenkov photons per unit track length of a muon in ice, denoted by $N_l$.

Taking into account the spectral range accessible by the detector, the direct Cherenkov emission from the muon amounts to approximately $3 \times 10^4$ photons per meter, see [ZC07]. In addition to this, the contribution of cascade-like radiative processes has to be considered, scaling with the energy according to equation (3.11). Above a critical energy of about 1 TeV, the linear term dominates and thus results in a simple proportionality between $N_l$ and the energy. Simulated neutrino events can be used to achieve a much more precise calibration of this relation. However, such an approach was not employed in this work, since an uncalibrated energy proxy in the form of $N_l$ suffices as a parameter for determining selection cuts.

The expected number of photons per DOM is now given as

$$\mu = N_l \cdot \mu_0(d) \tag{5.13}$$

---

[4] Additional indices on $\mu_i, n_i, \mu$ and $N$ for the designation of DOM numbers are suppressed for better readability.

and depends on the distance $d$ between the track and a DOM. The function $\mu_0(d)$, which parametrises this dependence, is provided in [Chi08]. It connects the regime of unscattered photon propagation very close to the track with the diffuse approximation relevant at greater distances.

Equation (5.13) can be used to perform a full maximisation of the waveform likelihood for all track parameters and the energy estimator. In the implementation discussed here, a simplified approach was chosen, separating the two terms in the two last lines of equation (5.12). The first term can be replaced by the MPE likelihood (5.10), thereby simplifying the dependence on the normalised expectation $\mu_i/\mu$ to one on the p.d.f. of the first photon. In the implementation of *Mue*, the result for this pure direction reconstruction is simply imported from a previously processed MPE reconstruction. Based on this track, the second term can be analytically minimised to derive the best fit value for $N_l$, entering via $\mu$ from equation (5.13), thus producing the desired energy estimator.

# Chapter 6.

# Event selection for a point source search above and below the horizon

A point source search with a neutrino telescope like IceCube crucially depends on the event selection. The main goal is to suppress the overwhelming background of muons produced in extensive air showers. To achieve an identification of neutrino candidates, events have to be rejected or retained based on directional information, quality of reconstruction and energy estimators. The optimisation and application of such data reduction steps is generally subdivided into several levels. This event selection chain for data taken with 22 IceCube strings is discussed in the following sections. Simulated signal and background events are used to judge the cut efficiencies with respect to a point source analysis. The chapter concludes with an overview of characteristic distributions of selected events in the final sample.

## 6.1. Data sample and Monte Carlo simulation

### 6.1.1. IceCube data from 22 strings

After the installation of the first 22 IceCube strings, data were taken in this configuration from 31st of May 2007 to 5th of April 2008. An off-line monitoring of rates, timing calibration and other stability indicators provided information to identify and exclude problematic runs[1]. Deviations in the performance of single DOMs were treated by excluding only these from further data processing. For this analysis, the run selection followed that of the point source analysis presented in [A$^+$09c]. After the exclusion of runs with noted problems in the general run list, two runs were rejected based on irregularities after a power failure. Furthermore, runs with less than 20 minutes of livetime were not used since these do not allow reliable rate checks to guarantee detector stability. Accounting for several small gaps during data taking in the selected runs, the total livetime of the full IC-22 data sample used here is 275.7 days.

---

[1] A run is defined as a continuous data taking period of normally 8 hours.

### 6.1.2. Neutrino simulation

Simulated neutrino events were used to determine the optimal event selection and calculate sensitivities for this analysis. The datasets were generated in the framework of the centralised Monte Carlo production for the IceCube collaboration. The methods and software for simulating neutrinos and their secondaries, in particular muon tracks, were described in section 4.2. Signal fluxes are generated with an $E^{-1}$ primary energy spectrum, providing equal event numbers per energy decade. The reweighting of the spectrum to an atmospheric flux or any desired signal characteristic is achieved by making use of stored weights for each event, which represent the total interaction probabilities of individual neutrinos.

As discussed in section 2.1.2, standard assumptions on neutrino production in astrophysical shock wave scenarios imply a natural power law with an exponent around $-2$ as a benchmark for signal expectations. Even harder neutrino spectra can also be considered realistic, emerging from the complex dependencies of hadronic processes on the environment of photon or matter targets. Since such harder spectra are of great importance for an analysis aiming at the highest accessible energies, as outlined here, a second benchmark signal hypothesis with a spectral index of $-1.5$ was used. While it is questionable if sources can feature an unbroken power law from TeV to EeV energies with an index as hard as $-1.5$, many models predict such a spectrum in certain limited energy ranges. In the light of recent studies about absorption of TeV photons from distant AGN, see [A$^+$06e, A$^+$08h], it is generally considered as an extreme possibility for intrinsic AGN spectra.

The neutrino simulation does not provide a point source flux but an isotropic distribution of primary directions. This setup is more appropriate for a study of cut efficiencies in dependence of zenith angle by providing a uniform coverage of track orientations. For the atmospheric neutrino spectrum the model of [BGL$^+$04] was used in the implementation of the flux weights, with an additional prompt component, see section 3.1.4, based on [FNV01].

No reference flux exists for the expected signal from cosmic sources. Its normalisation can be chosen arbitrarily with respect to the cut optimisation, since it suffices to compare relative efficiencies based on the number of events before and after cuts. Nevertheless, to provide an approximate scale of the expected signal strength relative to the background, the current limits from searches for diffuse neutrino fluxes were chosen as a reference. If not stated otherwise, in the plots of this section the $E^{-2}$ neutrino signal spectrum is scaled to an incoming flux of $E^{-2} \times 10^{-7}$ GeV cm$^{-2}$ s$^{-1}$ sr$^{-1}$, and the $E^{-1.5}$ spectrum to $E^{-1.5} \times 10^{-10}$ GeV$^{0.5}$ cm$^{-2}$ s$^{-1}$ sr$^{-1}$, resulting in similar absolute event numbers for both fluxes at filter level.

### 6.1.3. Atmospheric muon simulation

Compared to neutrinos, the simulation of atmospheric muons is based on a different software, generating the charged primary particles and their interactions in the atmosphere. This is done with the Corsika [HKC+98] package for air shower simulation, adapted to the requirements for passing events to the IceCube software. The hadronic interaction model chosen inside the Corsika framework is *Sibyll* [FGLS94, FGLS99]. The results are forwarded to the same software for propagation and detector simulation as described in section 4.2. In the simulation steps for propagation and detection in the ice[2], only the direct muon component from decays in the atmosphere is considered. The much lower flux of atmospheric neutrinos is simulated in a dedicated approach, as mentioned in the previous section.

A Corsika event in IceCube consists either of a single muon or a muon bundle. Such a bundle comprises several muons which are not resolved individually with the standard reconstruction techniques employed in this work and are treated as one track.

While in the normal simulation only one air shower per event is generated, the size of the detector often leads to a simultaneous detection of muons or muon bundles originating in two separate air showers within one trigger time window of 10 $\mu$s. The on-line software cannot distinguish between the separate parts of such an event and combines it into one set of DOM hits. A dedicated simulation effort is needed to reproduce this type of event with its special characteristics. Internally named *double coincident* events, they are shown as separate event samples in some of the following plots to highlight certain differences with respect to single air shower events. For the total background expectation they are combined with the single Corsika event generation, with the appropriate weighting to account for the different relative rates.

The *full* Corsika sample, including both the single as well as the double coincident component, has an effective livetime. This is derived from the rate of air shower events at a given primary energy at the South Pole. If not stated otherwise, the Corsika data in all plots in this chapter are scaled to match the actual total observation time of 276 days. This allows a direct comparison of event numbers and rates between measurement and simulation.

## 6.2. On-line filter

### 6.2.1. Filter settings at the South Pole

The trigger rate of the simple multiplicity trigger (see section 4.1.3) in IC-22 data was 500 Hz, with a corresponding data volume of 130 gigabytes (GB) per day.

---

[2] IceTop is disregarded in the following and not used in this analysis

Since the transfer of data to the North has to be accomplished via satellites with a limited bandwidth of approximately 32 GB per day, a filter to reduce data rates is necessary. Furthermore, it is desirable to achieve a low level selection of different data samples, so-called filter streams, designed to favour various characteristic event types based on the physics goals of different analyses. The two filter streams with the highest rates, filling roughly half the total bandwidth, are the *muon* and the *cascade filter*. They cover the two different types of neutrino interaction signatures, track-like in the former and particle shower in the latter case.

For the analysis presented here, two filter streams were used, the *muon filter* and the *extremely high energy* (EHE) filter. The muon filter has been designed to select tracklike events, based on a minimum threshold of 10 DOMs with photon hits. Due to the limited computing resources available for on-line filters, a simple *linefit* reconstruction, see section 5.1.2, was used to estimate the arrival direction of the event. While the original filter only allowed tracks with a reconstructed zenith angle larger than 70°, this was extended further into the down-going region. The threshold values on the number of hit DOMs (NChannel) were set to rise in two steps from 10 to 50 to suppress the overwhelming flux of lower energy atmospheric muons. The last of these steps, covering reconstructed zenith angles up to declination $-50°$($40°$ above horizon), was a filter extension designed specifically to allow detailed studies for the point source analysis presented in this work.

The EHE filter for IC-22 was a simple NChannel-threshold requiring 80 DOMs to be hit, with all-sky coverage. By using this filter stream in addition to the muon filter, additional bright events from far above the horizon (zenith angle $\leq 50°$) could be included. The combined on-line filter condition, depending on the reconstructed *linefit* zenith angle $\theta$, reads:

$$\begin{array}{rlll} & \text{NChannel} \geq 80 & & \\ \text{OR} \ ( & \text{NChannel} \geq 50 & \text{AND} & \theta \geq 50°) \\ \text{OR} \ ( & \text{NChannel} \geq 60 & \text{AND} & \theta \geq 40°) \\ \text{OR} \ ( & \text{NChannel} \geq 70 & \text{AND} & \theta \geq 10°) \ . \end{array}$$

### 6.2.2. Zenith distribution of filtered events

Figure 6.1 compares experimental data with Monte Carlo simulation of muon background and various neutrino fluxes. Plotted versus cosine of zenith, the structure of the filter setup is visible in the stepwise suppression of the originally rising muon rate above the horizon. Even for events reconstructed as up-going, the background of atmospheric muons dominates by several orders of magnitude over any atmospheric or possible signal neutrino flux. Since no muon from an air shower can travel more than a few tens of km inside Earth, see Fig. 3.5, these events at zenith angles larger than 90° are misreconstructions. In particular coincident air showers are often misreconstructed in this way due to the fact that the simple

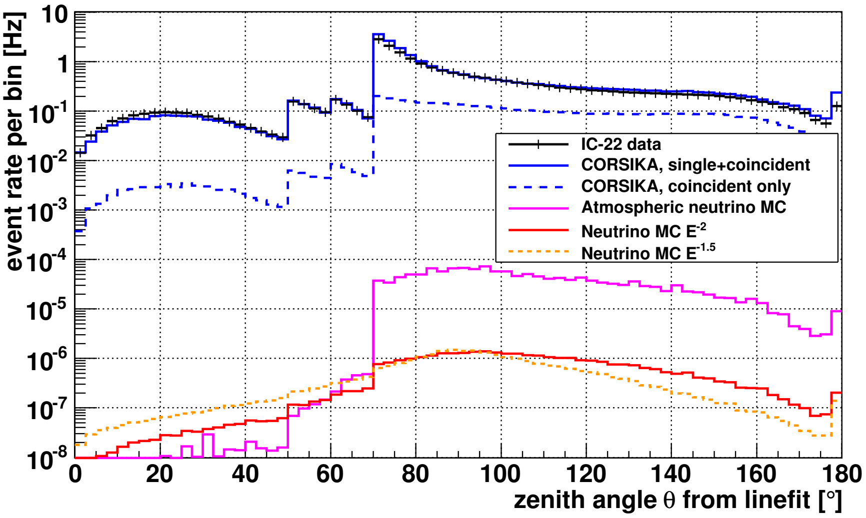

Figure 6.1.: Event rates as a function of zenith angle for IceCube data at on-line filter level (22 strings, Muon and EHE filter streams) compared to signal and background Monte Carlo simulation. The angles were reconstructed with *linefit* and highlight the stepwise filer cuts.

*linefit* reconstruction connects photon hits from two separate down-going muons in one up-going track fit.

To illustrate the efficiency of the on-line filter for neutrino events, Fig. 6.2 shows the fraction of events passing the cuts as a function of zenith angle. In the low-threshold region above 70°, the passing rate is slightly below 90% for an $E^{-2}$ spectrum and above 90% for a harder $E^{-1.5}$ spectrum. In the down-going part, with its strong NChannel cuts, the fraction of selected $E^{-2}$ events lies between 20% and 30%. Here, only the sample with a harder signal spectrum hypothesis give passing rates between 30% and 60%, justifying this high energy selection.

Considering the overwhelming contribution from misreconstructed muon events visible in Fig. 6.1, an improved reconstruction is crucial for background rejection. For simulated neutrinos with an $E^{-2}$ spectrum, the angular resolution of *linefit*, averaged over the full zenith range, is 10.3°, hence not yet precise enough to allow a point source search.

## 6.2.3. Seasonal background variations

Filter rates are not constant over the year due to seasonal variations in the atmosphere which influence air shower interactions and decay and consequently the number of atmospheric muons in the detector. The main effect relevant here is the expansion of the atmosphere in austral summer. The lower density leads to a reduced rate of meson interactions with air molecules in the upper layers of

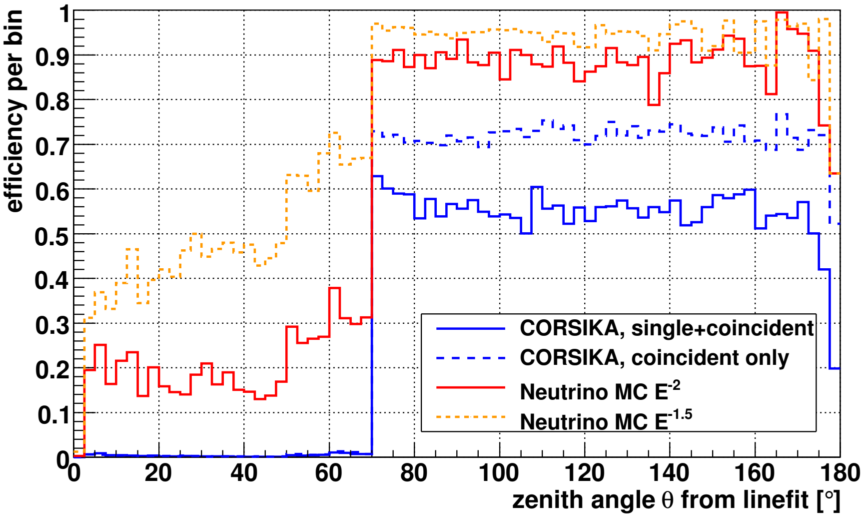

Figure 6.2.: Efficiency for Monte Carlo events at the IceCube on-line filter level (22 strings, Muon and EHE filter streams) as a function of zenith angle and relative to trigger rates. Above the horizon (on the left) atmospheric background is strongly suppressed while high energy signal neutrinos are retained.

the atmosphere so that more of these air shower mesons decay before they can interact. This results in a larger number of muons reaching the IceCube detector and increases the trigger and filter rates. A detailed study of the phenomenology is presented in [TDK$^+$09].

The Corsika background simulation used for IceCube in-ice analyses uses only one atmospheric model, equivalent to the South Pole conditions in October. To estimate the seasonal effects at the filter level described above, Fig. 6.3 compares this Corsika simulation with four runs, taken on the 15th of June, September and December 2007, as well as March 2008. The largest changes between summer and winter months are approximately ±10% of the average. The shape of the zenith distribution is basically unchanged for the different seasons, generally matching that of the simulation.

For a time integrated point source search, relatively slow changes of this kind are irrelevant, since background in each zenith band is measured from the summed total of data events over the full year, see section 7.1. For time-dependent searches like the one in section 7.3, it is important to account for seasonal variations.

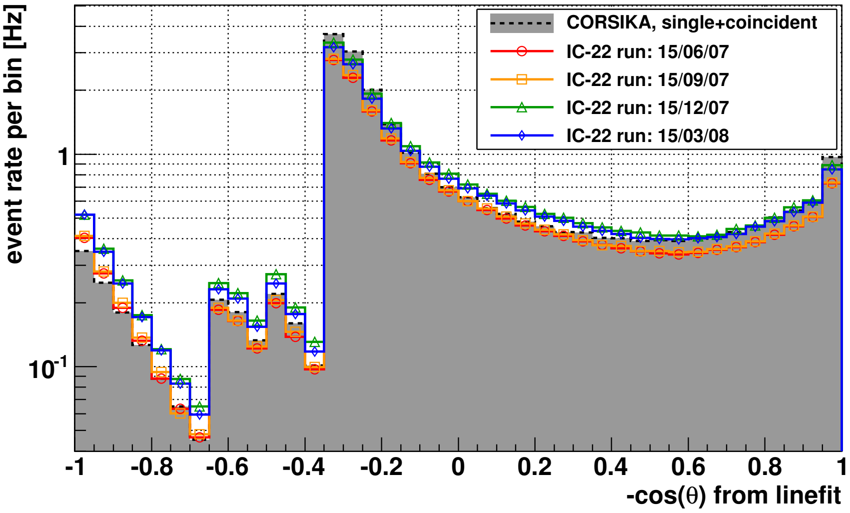

Figure 6.3.: Event rates of atmospheric muons at on-line filter level for different seasons over the year. The distributions are shown in dependence of the zenith angle $\theta$ as reconstructed with the *linefit* first guess algorithm and highlight the step-wise filter cuts.

## 6.3. Off-line event selection

### 6.3.1. Low-level background rejection

#### Level 2

The events that passed the combined muon and EHE filters were processed off-line to provide better track reconstructions and quantify other event characteristics. At this stage, a common set of algorithms was used, defined by the collaboration and applied under the name *level 2*. For this analysis, the most important additional information from this processing stage was the track result obtained with a single iteration of the SPE likelihood fit, see section 5.2.2. The distribution of the zenith angle $\theta$ from this reconstruction is shown in Fig. 6.4, with $\cos(\theta)$ on the x-axis to obtain bins representing equal areas. The stepwise structure of the on-line filter is already washed out due to the improved direction fit compared to *linefit*.

The cuts described in the next paragraph are based on the *level 2* reconstruction results. The CPU time necessary to perform the MPE reconstruction, which has been shown to provide improved angular resolution in section 5.3, does not allow the processing of the data from the full year before this reduction is performed.

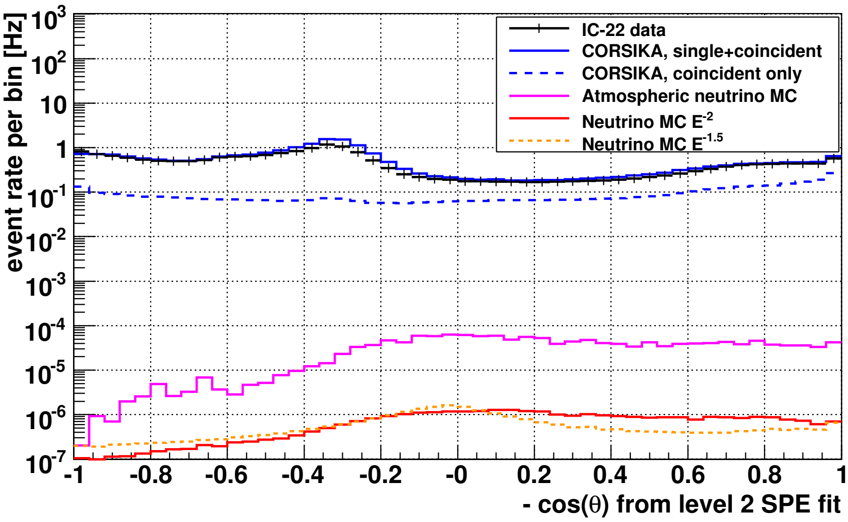

Figure 6.4.: Event rates as a function of zenith angle. Only on-line filter cuts are applied, but their structure is smeared out due to the improved reconstruction with the SPE likelihood fit from *level 2* processing.

### Level 3

For steeply down-going neutrino events, the 1 km thick ice layer above the detector provides too little interaction volume, as can be seen in the falling signal expectations in Fig. 6.4. A hard cut was placed on the zenith angle at 40° to completely reject the background from this part of the sky. After the MPE likelihood fit was performed for all events passing the *level 3* criteria, this zenith cut was applied again, making use of the better reconstruction to reject further events.

The second *level 3* cut was a threshold on the number of hit channels, NChannel $\geq$20, for events with reconstructed zenith angles smaller than 80°. Considering that the on-line filter condition includes a stronger cut on all events with *linefit* zenith angles smaller than 60°, this additional requirement has little rejection power. However, events which were at first reconstructed with larger zenith angles passed lower NChannel thresholds and can now be identified as down-going with the *level 2* SPE information. This cut guarantees a more uniform rejection of such events with low brightness.

The third cut was planned as a simple one-parameter cut for background suppression both above and below the horizon. Several variables were compared in their rejection power for a chosen signal passing rate. A standard IceCube track quality parameter obtained from the 1-iteration SPE likelihood fit and called *reduced log-likelihood* (rlogl) proved to be the most efficient one. It is computed as the negative logarithm of the likelihood minimum from the SPE Pandel fit, see section 5.2.2, divided by the number of degrees of freedom. The latter is given by the number of hit DOMs minus five, which is the number of track fit

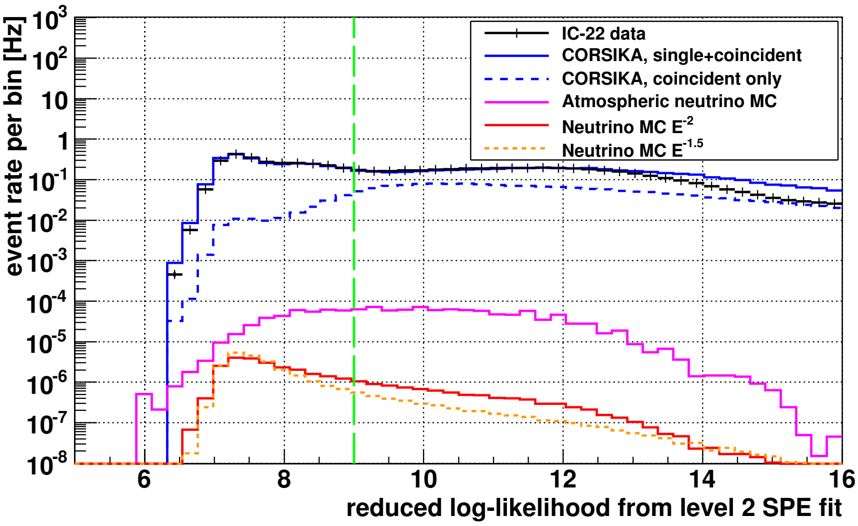

Figure 6.5.: Reduced log-likelihood distribution (SPE fit quality parameter) after cuts on the number of hit DOMs and zenith angle $\theta > 40°$. The green dashed line indicates the main *level 3* cut, selecting events with reduced log-likelihood $\leq 9$.

parameters. This does not fully account for the fact that these parameters are not completely independent, but works well as a quality cut. The threshold value chosen as sufficient at this level was: reduced log-likelihood $\leq$9. Bright events tend to have smaller reduced log-likelihood values, but this bias is not a problem for this analysis aimed at high energies. The effect is visible in Fig. 6.5 when comparing the line for the $E^{-2}$ signal spectrum hypothesis to the one representing the hard $E^{-1.5}$ power law. The distribution of reduced log-likelihood displays a good agreement between CORSIKA background simulation and measured data, with a slight over-estimation of the Monte Carlo events at very large and very low reduced log-likelihood values.

After the three *level 3* cuts the mean data rate, averaged over the full livetime is 2.7 Hz, 12% of the on-line filter rate. The efficiency for an $E^{-2}$ neutrino signal hypothesis is larger than 65% relative to the on-line selection, and around 80% for primary energies above $10^5$ GeV or an $E^{-1.5}$ spectrum. One should keep in mind that these average values represent signal distributions which vary in dependence of the zenith angle and cover quite different energy regimes in the down-going part above the horizon versus the up-going fraction from below the horizon. This is discussed further in the following.

### Level 4

Shown in Fig. 6.6 is the zenith angle distribution based on the MPE likelihood reconstruction which has become available after processing the events selected at

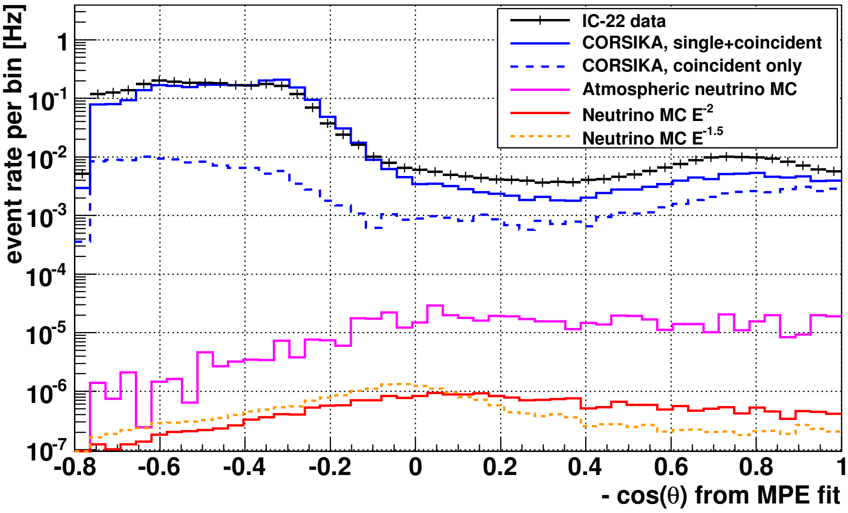

Figure 6.6.: Event rates as a function of zenith angle, reconstructed with the MPE fit, after *level 3* cuts.

*level 3*. Due to the steeply rising atmospheric muon background, the rates above the horizon are more than one order of magnitude larger than those below the horizon. The up-going background is, at this level, dominated by misreconstructed muons. The down-going events are mainly well reconstructed muon bundles. As outlined in section 3.3, they have to be reduced by cuts based on two criteria for distinction from neutrino-induced events: The soft atmospheric energy spectrum and differences in the event topologies, i.e. the light distribution of multiple muons in bundles versus that of single high energy muons.

For the cuts at this level, the MPE fit results as well as an energy estimator from the *Mue* module, described in section 5.4, are available. Both reconstructions were run on all events passing the *level 3* cuts. The basic idea of the *level 4* selection is to use these two event variables to define a two-dimensional threshold function for a topology-related cut parameter. The shape of this function is derived from the distribution of actual data, dominated by background muons. With this approach, the cut value is determined as a function of energy and zenith angle for each event and scales according to the actual background rate that needs to be suppressed.

After comparing different cut variables, the so-called *hits per channel* was found to have the strongest background rejection power for down-going events. The name *hits* was kept for consistency with IceCube conventions, referring to the number of pulses extracted from a waveform, see section 4.1.3. Each hit does not necessarily represent only one photoelectron but can have a higher charge if several photon pulses are not resolved individually. Nevertheless, this parameter provides an approximate estimate of the photon multiplicity in each DOM. It also avoids problems with the charge estimation that occurred in early simulations of 22-

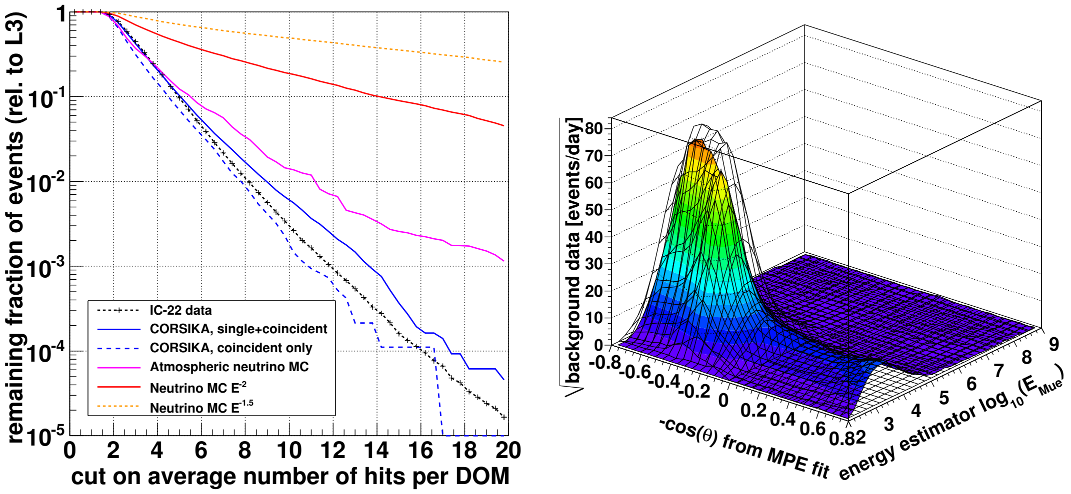

Figure 6.7.: *Left:* The remaining fraction of events after a cut on the number of hits per DOM, relative to *level 3*. *Right:* Distribution of measured data in dependence of zenith angle and *Mue* energy estimator. A fit to this shape (mesh) provides the parametrisation for the cut on average hits per channel at *level 4*.

strings data. Dividing by the number of channels that were triggered, i.e. DOMs participating in the event, the resulting number of hits per channel is an event parameter correlated to the photon density.

Since very high energy air showers predominantly produce multiple muons traversing the detector in muon bundles, the event topology is different from single muons induced by cosmic neutrinos. A very energetic single muon produces not only Cherenkov emission, but also secondary particles in concentrated showers along its track. These event topologies have a narrower, more concentrated light emission compared to the muons in a bundle which can have the same total brightness with their combined Cherenkov light, but spread out more homogeneously over a wider emission region. Setting lower thresholds on the number of hits per channel favours the higher photon densities along neutrino-induced muon tracks. Furthermore, in these high energy signal events, the major light contribution from cascades of secondary particles is not emitted directly from the muon. This expanded emission topology leads to more late hits of single photons after the main Cherenkov cone. Using the number of hits instead of, for example, the charge of events, one expects a larger weight from this signature of late pulses.

Due to the large spatial separation between DOMs, as well as prevailing uncertainties about light propagation in the ice, a more detailed study of muon bundle topology within IceCube was not possible within the scope of this thesis. Nevertheless, a check of cut efficiencies for different variables, including comparisons to those using charge information, corroborated the above explanations. Exploiting

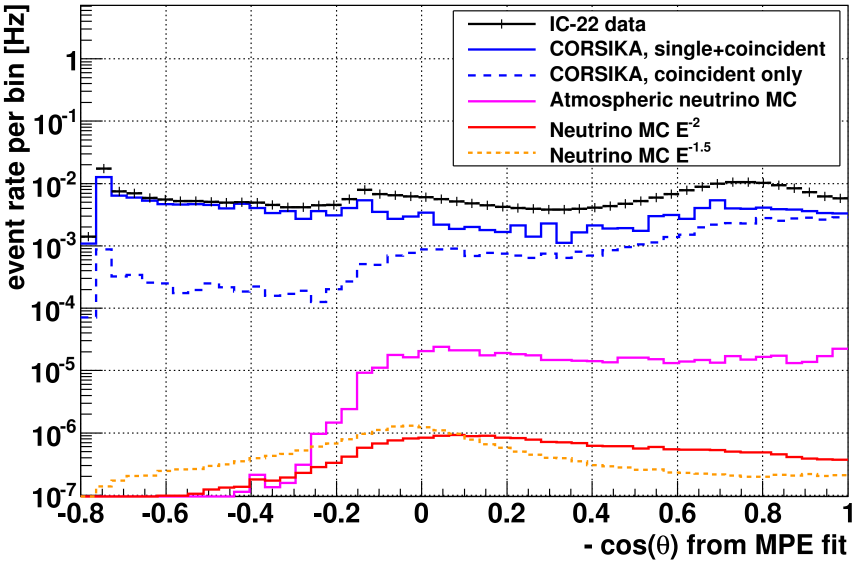

Figure 6.8.: Event rates as a function of zenith angle, reconstructed with the MPE fit, after *level 4* cuts.

hit time information to count for example late hits showed no improvements over the use of the number of hits per channel. Further progress on reconstructions using the full waveform information may lead to future improvements, though.

To illustrate the efficiency of the cut on number of hits per channel, the left part of Fig. 6.7 highlights the passing rates for rising cut strengths in a logarithmic plot, with the cumulative passing rate on the y-axis and the threshold value on the x-axis. The background rejection of this variable behaves like a power law over several orders of magnitude. The hits per channel also show good agreement in the rejection power of data and CORSIKA MC.

To illustrate the scaling of the threshold with a two-parameter function, the right plot in Fig. 6.7 shows the square root of the background data (events per day) at *level 3* as a two-dimensional histogram over zenith angle (MPE reconstruction) and energy estimator (uncalibrated *Mue* reconstruction). Using slices along the energy-axis, with steps of 0.05 in $\cos(\theta)$, a Gaussian fit of the background distribution was performed for each zenith band. The fitted histogram is displayed as a mesh on top of the distribution. With the goal to reduce the down-going muon rate to the level of the up-going background rate, $\sim 0.5$ Hz at this stage, this fit to the square root of the background rate defines the cut value. It is normalised to give a maximum threshold value of approximately 15 hits per channel. The parametrisation is cut off at the horizon ($\cos(\theta) = 0$), since other variables are known to be more effective to reduce the misreconstructed muons below the horizon. The actual threshold function is given in appendix A.

The resulting zenith distribution shown in Fig. 6.8 validates that the down-going background on the left was suppressed to a reasonably flat level. This actually shows slightly better agreement between data and simulation when compared to the up-going regime, were certain features of misreconstructed muons seem not to be fully reproduced in the Corsika events.

Compared to the previous level, the hits-per-channel cut has reduced the background in the region above the horizon by a factor of $\sim 10$. It should be noted that the atmospheric muon rate still dominates over any signal expectation by several orders of magnitude. No further optimisation of the actual threshold scaling was attempted, for example by using a more elaborate fit or including the signal expectation, because a dedicated cut optimisation for point source searches follows in the next step. The *level 4* background reduction to an average rate of 0.3 Hz over the full zenith region from 40° to 180° was sufficient to run the multi-variate cut optimisation described in section 6.3.2.

The *level 4* cut efficiency for an $E^{-2}$ signal spectrum is 90% relative to *level 3* (58% relative to the on-line filter) and exceeding 96% for an $E^{-1.5}$ spectrum. No other cut choices that were tested, with or without scaling to the background, showed the same or better passing rates for a comparable reduction of the background.

### 6.3.2. High-level quality selection

As discussed in section 3.3, very different energy regimes of neutrinos are covered by observing induced muon tracks if they are up-going compared to down-going. In combination with the two backgrounds of atmospheric muons from above the horizon and atmospheric neutrinos from below, this leads to a zenith-dependent efficiency of selection cuts. Consequently, thresholds for an optimised event selection have to be adjusted as a function of reconstructed zenith angle to achieve the necessary background suppression. In the final step of event selection for this analysis, the sky was subdivided into 35 zenith bands with each half of a band overlapping with the neighbouring one. Cuts on several variables were optimised in each band to yield the best sensitivity. The sensitivity was calculated based on the Feldman-Cousins approach as described in section 3.2.2.

After several tests with different sets of event characteristics, five variables were selected, together with the search bin radius as a sixth free parameter. Using 10 to 20 discrete steps for each parameter range, a programme tested all combinations of threshold values to find the set of cuts which yield the optimal sensitivity in each band. This optimisation was performed twice for different reference signals of simulated neutrinos, one with an $E^{-2}$ spectrum and one with as a harder spectrum, $E^{-1.5}$ . To smoothly combine the results for different zenith bands and find a compromise between the two results for different signals, a linear function of the zenith angle was derived for each cut variable.

In the following, the variables for the optimisation are listed with a short description of their quality as final cutting parameter. In the plots in Fig. 6.9, the

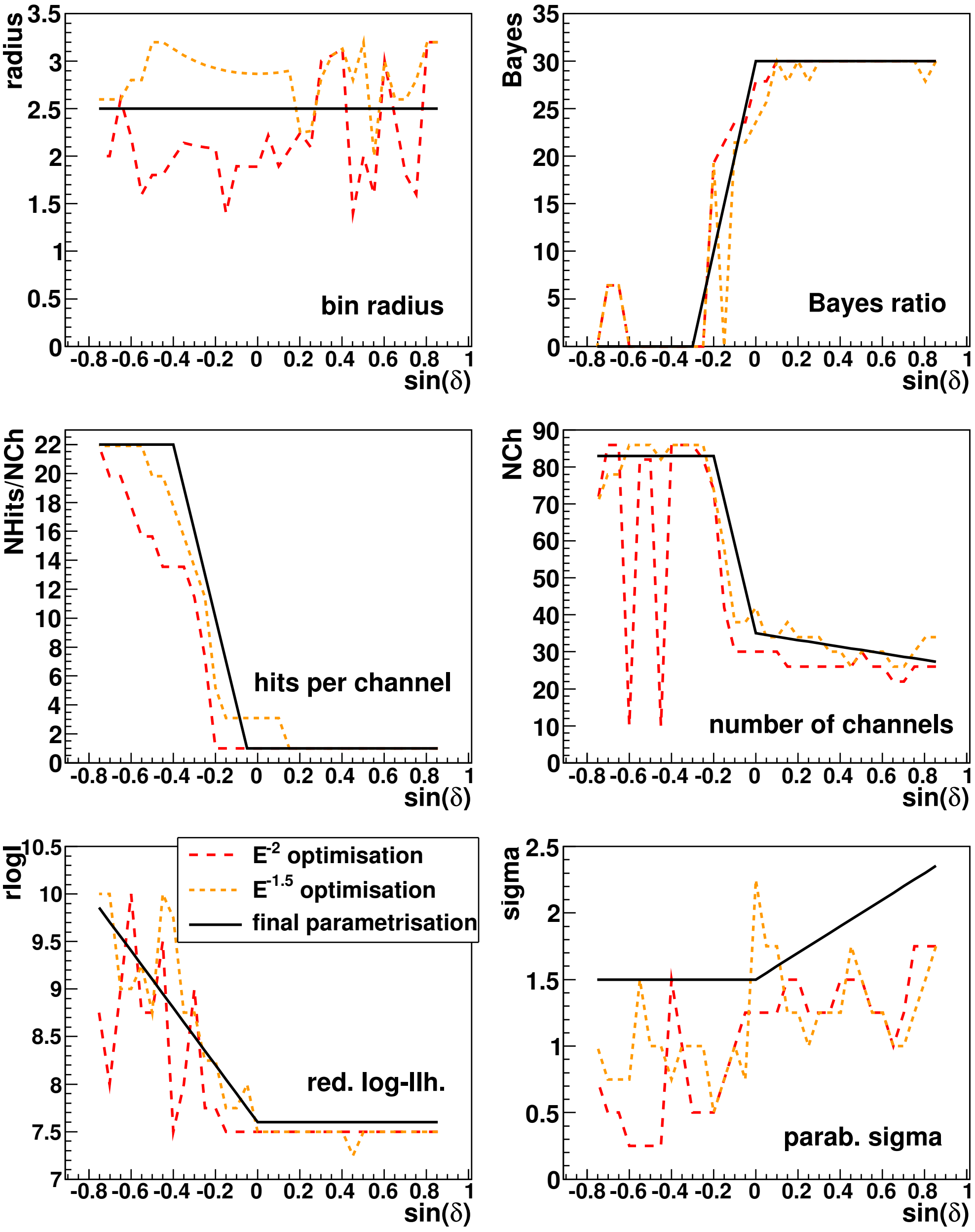

Figure 6.9.: Results from simultaneous optimisation of five cut parameters based on $E^{-2}$ (red) and $E^{-1.5}$ (orange) signal benchmark spectra. The parametrisations chosen for the cuts at final level are shown as black solid lines, for details see appendix A.

optimal cut values for 35 overlapping zenith bands of width $\Delta\cos(\theta) = 0.1$ are shown.[3] The red curves refer to the $E^{-2}$ spectrum, the orange to $E^{-1.5}$ and the black solid line is the chosen linear parametrisation. The latter determines the cuts applied to data and Monte Carlo for determining the sensitivity and for the eventual binned search. The actual formulae and values of the parametrisation are given in appendix A.

### Bin Radius

The radius of the angular search bin was varied between 1.5° and 3.2° in the optimisation of testing all cut and bin size combinations. Finally, a fixed size of 2.5° was chosen, since the variations with declination showed no particular potential for an optimisation. This is not surprising, considering that cuts on quality parameters like the paraboloid sigma error (see below) are more precise tools for selecting events with good angular resolution.

### Bayesian Likelihood Ratio

This variable is the logarithm of the ratio of likelihood values from the SPE track fit divided by the Bayesian track fit (32 iterations each), see section 5.2 for details. The Bayesian ansatz is based on the angular distribution of background muons and the difference between the likelihood values is only large for events which do not follow this distribution, hence those that are not down-going. Thus, for horizontal or up-going tracks, a minimum cut value on this ratio is very useful to reject atmospheric muons produced in air showers. For tracks from above the horizon this method cannot exploit a fundamental difference in the angular distribution between signal and background and the parameter should not be used for a cut, as is obvious in the optimisation plot.

### Hits per channel

This variable which counts the number of hits per DOM was used as main cutting parameter at *level 4* and remains very useful to reject down-going muons, relying in part on a good energy correlation. As expected, the optimisation shows that it should primarily be used for cuts on the down-going events above the horizon.

It has to be remarked that the final cut optimisation here leads to threshold functions depending only on zenith angles. The additional inclusion of an energy estimator, as employed in the parametrisation of the *level 4* cut in the previous section, was not practical with respect to the amount of computing time needed for the scan over all combinations. Cutting again on hits-per-channel in the simpler form of a one-dimensional function partially reduces the advantage of the more

---

[3] The x-axes show $\sin(\delta)$, which is the sinus of the declination, spanning $-50° \leq \delta \leq +90°$ or 40° to 180° in zenith angle $\theta$. Hence, $\sin(\delta)$ is equivalent to $-\cos(\theta)$.

structured cut in the previous selection step. However, considering the computational limitations, the chosen optimisation approach profits from the introduction of a larger variety of cut variables. This improves the signal efficiency through an optimised interplay instead of tuning only one parameter.

### Number of channel

The number of hit channels, i.e. DOMs taking part in the event, is a simple energy estimator. A threshold applied to this variable also serves to improve the angular resolution by rejecting events with short track lengths and thus generally bad track fit.

### Reduced log-likelihood

The logarithm of the likelihood value of the MPE fit divided by the number of hit DOMs minus five is a track quality parameter. In the same way as discussed in section 6.3.1 for *level 3*, a cut on this variable favours higher energy events and rejects track fits with large uncertainties. It helps mainly to reduce coincident background events misreconstructed as up-going tracks.

The linear parametrisation for this cut has been slightly weakened in the up-going part compared to optimal values. This was done to avoid too low event numbers and reduce possible systematic effects in a low-statistics regime.

### Paraboloid Sigma

The paraboloid reconstruction estimates the angular error ellipse by mapping the likelihood space near the minimum, see section 5.2.5. The version of the Pandel-MPE reconstruction employed for this work is known to produce values, called paraboloid sigma, which are up to two times lower than the true reconstruction error. Nevertheless, disregarding the absolute scale, the parameter still serves to estimate relative track quality. A cut on it helps to reject misreconstructed muons and events which cannot be fitted properly and hence are of less importance in a point source search. With respect to these scaling uncertainties, the parametrised cuts have been slightly weakened compared to optimal values to reduce possible systematic effects.

### Number of direct hits

After the optimisation for the five parameters and the bin radius discussed above, the thresholds were applied as linear parametrisation. In the up-going part, a comparison of atmospheric neutrino simulations and data showed a slight excess of measured events after these cuts. This is considered to be a contamination of misreconstructed atmospheric muons, based on the fact that CORSIKA simulation, though statistically limited, predicts a remaining contribution of these background

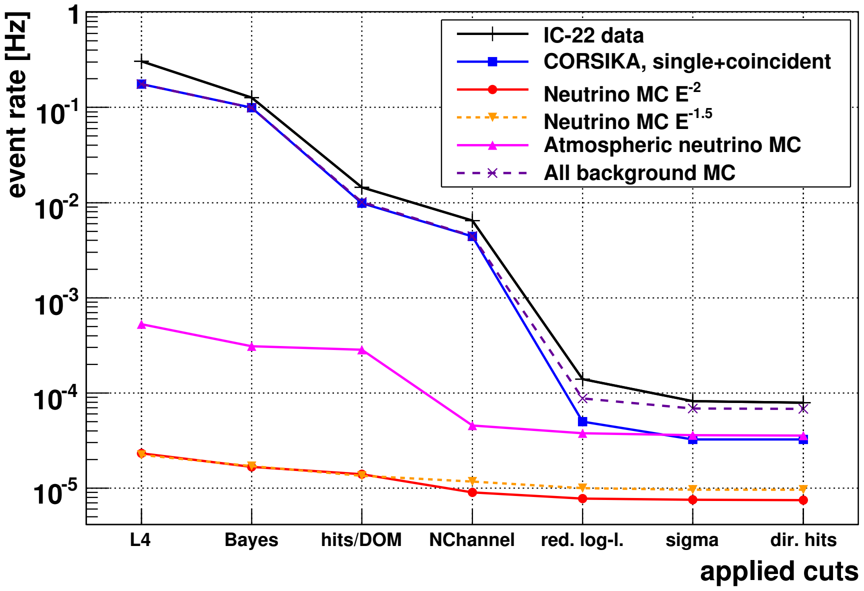

Figure 6.10.: Reduction of data and simulated background samples as well as signal expectation in dependence of the successive application of *level 5* cuts. See text for a description of the variables.

events below the horizon. They are not critical for a point source search based on directional event excesses since they are isotropically distributed. Nevertheless, achieving a sample with a higher purity of atmospheric neutrino-induced muons in the up-going part is desirable. The introduction of an additional weak cut for zenith angles $\theta \geq 90°$ reduces these misreconstructed events.

The number of direct hits is a suitable parameter, a prescription to quantify the number of DOMs hit by practically unscattered photons. Given a track fit, in this case the MPE-Pandel reconstruction, the residual time between expected and observed detection of a Cherenkov photon is calculated, see section 5.2.1. If this time difference does not exceed a given range[4], the channel is counted as a direct hit. A cut on this variable helps to reject misreconstructions. For these, few direct hits are expected due to the assumption of a wrong track direction. Based on this motivation, the cut was only applied for up-going declinations $\delta > 0°$ with a constant threshold of 30 direct hits.

The background reduction achieved with these six cut parameters is approximately a factor $3 \times 10^{-4}$ compared to the previous *level 4* selection, averaged over all zenith angles and energies. Figure 6.10 illustrates the reduction of data and Monte Carlo samples with each successive cutting step, as well as the effect on the signal simulation. Details on the compostion and characteristics of the *level*

---

[4] The range was chosen here to be $-15$ ns $< t_{res} < +250$ ns.

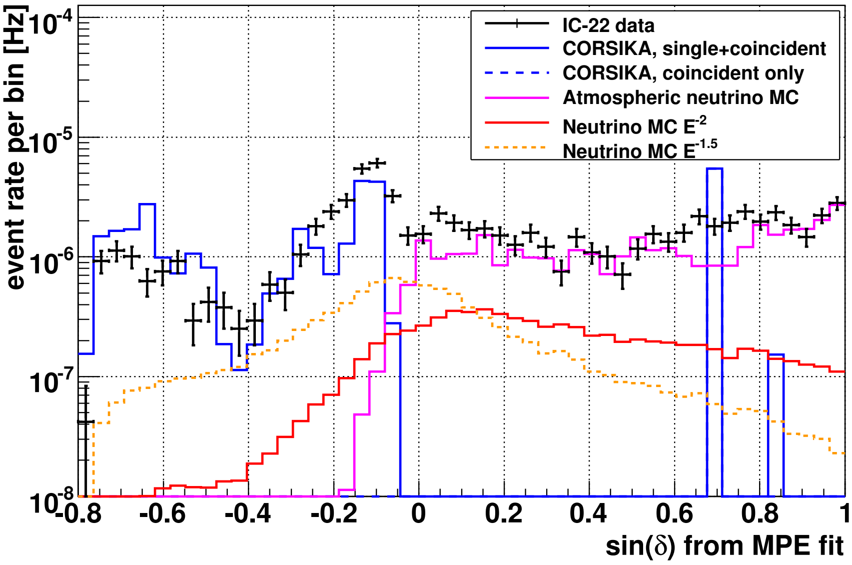

Figure 6.11.: Event rates as a function of zenith angle, reconstructed with the MPE fit, at the final selection level. Up-going events on the right follow the distribution of atmospheric neutrino simulation. The statistics of the weighted CORSIKA Monte Carlo sample are limited but approximately describe the data, in particular in the downward regime on the left.

*5* data sample are discussed in the following section.

## 6.4. Final event sample characteristics

### 6.4.1. Zenith angle distribution

The event selection described in the previous section was optimised on various levels to allow a point source search focusing on neutrinos with energies above 100 TeV and with primary energy spectra of $E^{-2}$ or harder. Efficiencies and energy ranges of expected signal events passing the cuts are very dependent on their incoming zenith angle due to the interaction probabilities in the matter through which they have to travel before inducing a signal in the detector. All cuts were determined by the requirements of suppressing different backgrounds of down-going muons from above the horizon and an isotropic atmospheric neutrino flux.

Applying the cuts to data with 276 days of livetime, the resulting final sample is composed of 1885 events in a range of reconstructed zenith angles between 40°and 180°. This is equivalent to a declination coverage of $-50°$ to $+90°$ in equatorial coordinates. Event selection in the northern hemisphere was focused on rejecting

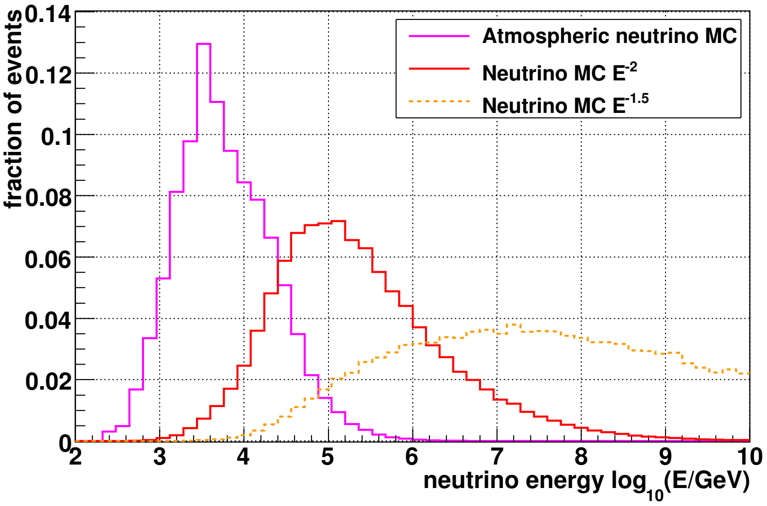

Figure 6.12.: Distribution of neutrino energies for three simulated spectra at final selection level.

misreconstructed atmospheric muons resulting in a relatively flat passing rate over the whole region below the horizon. The right part of Fig. 6.11 shows that data in this region largely match the expectation from a neutrino flux generated in the atmosphere by charged cosmic rays. Two CORSIKA events remain at final level. One is a simulation of two coincident showers with a high Monte Carlo weight. Sensitivity studies led to the conclusion that harder cuts, which could eliminate such background, would lead to a significant reduction in signal efficiency and are not necessary since the point source method is robust against any background with an isotropic distribution in right ascension, see section 7.1.

Regarding only the up-going part ($\delta > 0°$), measured data includes 1099 events. The simulated contribution of atmospheric neutrinos is 823 with a statistical uncertainty of $\pm 39$, to which weighted CORSIKA Monte Carlo adds an additional $133 \pm 130$ events. This places the measured total at the upper limit of but within the uncertainty estimate. It is discussed further in section 8.4.

At negative declinations, the down-going subsample as shown on the left of Fig. 6.11 comprises 786 events. Based on the simulation, only $29 \pm 3$ events due to atmospheric neutrinos are expected. Here, down-going muons dominate the background. This is qualitatively represented in the CORSIKA simulation, showing $637 \pm 68$ events and hence only slightly less then the measured rate. The difference is discussed in section 8.4. The uneven zenith distribution is a result of the cut optimisation with several parameters, which was not tuned to deliver a particularly flat event sample.

A peak of passing events in the region $-0.2 \leq \sin(\delta) \leq -0.1$ just above the horizon is caused by the fact that this zenith band does not only feature the maximum in the signal expectation for an $E^{-1.5}$ neutrino spectrum, but also the

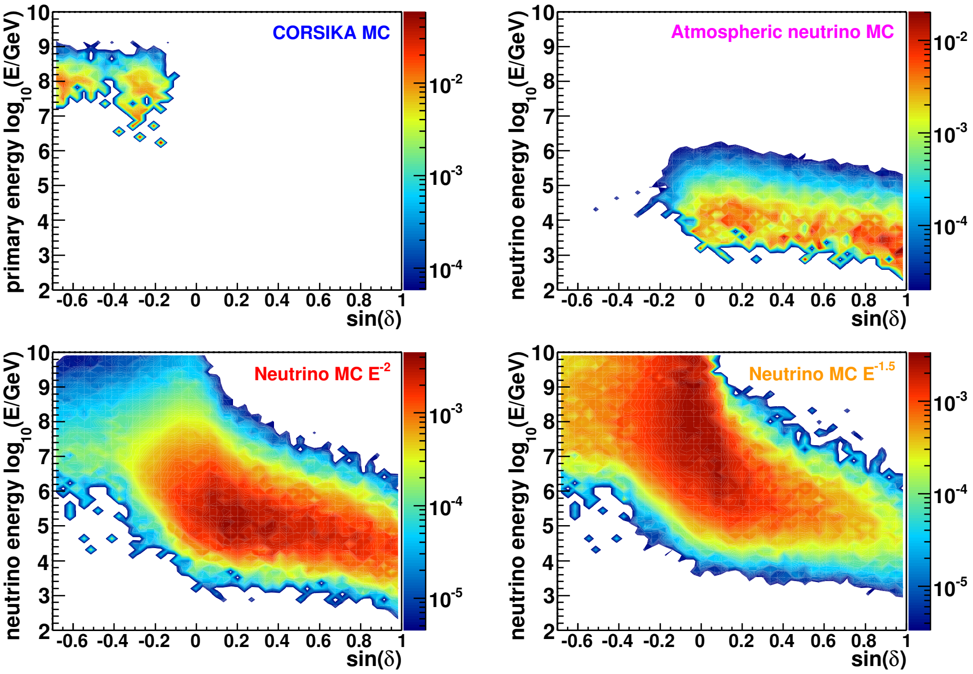

Figure 6.13.: Distribution of primary energies for simulated events in dependence of true declination. The colour indicates the fraction of events per angle and energy bin at final selection level.

onset of the rising background of down-going atmospheric muons. For smaller negative declinations, the stronger thresholds on the number of channels and hits per channel restrict this background rate much more strongly. The choice of the cut parametrisation in Fig. 6.9 explains the onset of another rise below about -0.4 in $\sin(\delta)$, were the limited signal statistics effectively prohibit a fine tuning of cuts to avoid such fluctuations.

### 6.4.2. Energy distribution

The background flux of atmospheric neutrinos with its spectral index of $\sim -3.7$ (section 3.1.4), is significantly softer than the expected contributions of signal neutrinos following $E^{-2}$ or harder power laws. Figure 6.12 represents this fact by directly comparing the normalised energy distributions, averaged over all simulated events passing the final selection cuts.

As discussed before and based on the considerations in section 3.3, cuts for a neutrino point source search necessarily have to lead to very different regimes of covered signal energies above versus below the horizon. To study the effective energy thresholds introduced by the cuts presented here, Fig. 6.13 shows two-dimensional histograms with sinus of declination on the x-axis and primary energy on the y-axis. A Corsika background sample and the atmospheric neutrino

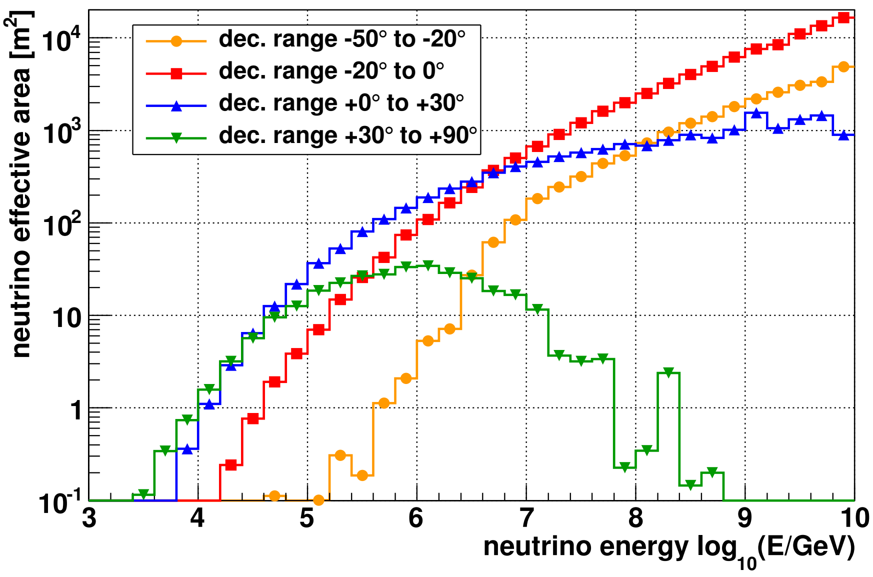

Figure 6.14.: Muon neutrino effective areas for an $E^{-2}$ spectrum at final selection level. For positive declinations, highest energies are suppressed through absorption. The curve for $-50°$ to $-20°$ on the other hand is lowered in general due to the strong cuts for down-going events.

model as well as the two benchmark signal spectra are compared. The colour indicates the fraction of events per bin at *level 5*.

The remaining background from air showers in the CORSIKA simulation is dominated by down-going muons with cosmic ray primaries above tens of PeV. Atmospheric neutrinos, on the other hand, can only contribute as up-going events from the northern hemisphere, displaying a relatively flat energy distribution since only the quality cuts matter in this region. The two neutrino signal spectra in the lower part of Fig. 6.13 clearly illustrate the effect of the energy-sensitive cuts. The lower energy threshold for neutrinos rises from one TeV in the up-going part to approximately one PeV on the down-going side. Compared to the $E^{-2}$ spectrum, the bulk of expected events from the $E^{-1.5}$ case is shifted to PeV energies and hence to the region at and below the horizon. The suppression of the highest energies is visible as a cut-off, scaling with the rising declination.

Another way of quantifying the acceptance of the sample with respect to neutrinos is the neutrino effective area, introduced in section 3.2.2. Figure 6.14 shows these values for equivalent detection areas as functions of energy, separately for four zenith regions. The rise with energy up to at least the PeV regime is a common feature, stemming from the detector limitations to measure faint light signals on the one hand and the increasing cross section on the other. The lines representing up-going events display a flattening and even a strong decrease for

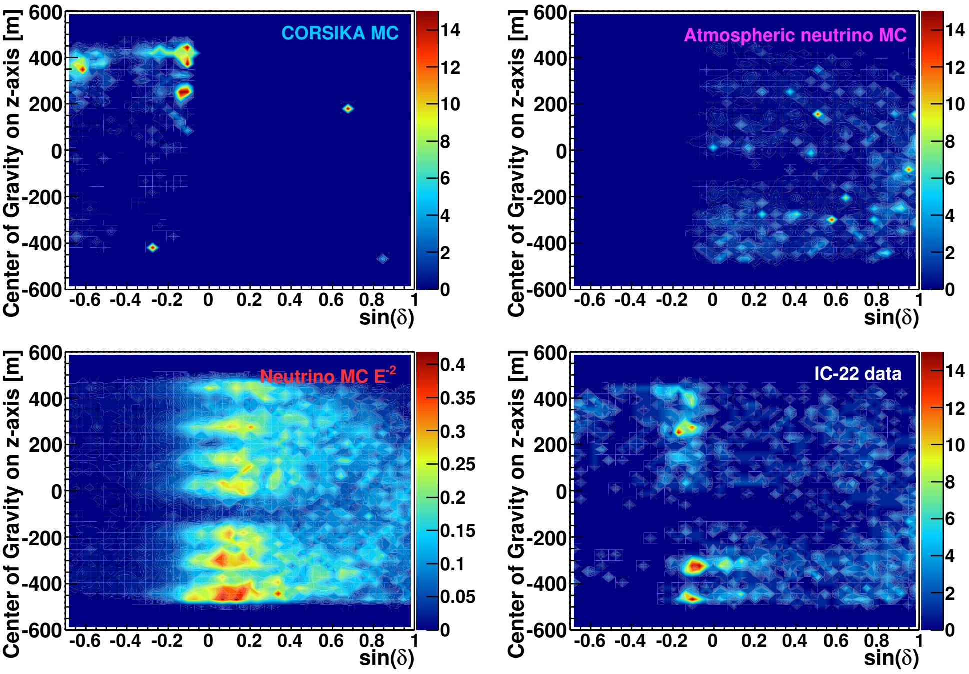

Figure 6.15.: Distribution of the centre of gravity of hit DOMs along the z-axis in dependence of reconstructed declination at final selection level. The colour indicates the number of events and the three Monte Carlo samples have the same normalisations as in Fig. 6.11.

the steepest zenith band above 120°, an effect of the absorption of the most energetic neutrinos in the Earth. The down-going sample on the other hand has an increasing effective area up to the highest energies simulated.

### 6.4.3. Depth dependencies

Figure 6.15 displays background and signal simulation, as well as measured data, in histograms for the centre of gravity along the y-axis, as derived from the depth of all DOMs with registered hits, in dependence of the reconstructed declination. The fact that many down-going muons penetrate the detector only up to a certain length before they are stopped leads to an accumulation of this background signature in the top part of the detector, visible in the upper left panel. The atmospheric neutrino background, on the other hand, mainly appears in the form of up-going events, which are consequently slightly biased towards the lower part of the detector.

Section 4.1.1 introduced the detector medium, the South Pole glacier, as a layered structure which leads to a clear depth dependence of photon detection efficiencies. A prominent feature is that the ice below approximately -200 m is clearer then in the shallower layers. This results in a particularly efficient detection of up-going muons in this deep part.

The signal simulations show a more uniform efficiency along the z-axis, thereby highlighting the various dust layers as deficit regions in the lower left panel of Fig. 6.15. These strong absorption effects are also visible in the histogram for measured data in the lower right, which overall shows good agreement with the superposition of muon and neutrino backgrounds.

### 6.4.4. Angular resolution

The angular resolution and its dependence on different event parameters was discussed in section 5.3, including the stable performance of the MPE-Pandel reconstruction over the full range of zenith angles and energies. Here, only two final average values for the angular resolution are given, 1.3° for an $E^{-2}$ and 1.2° for an $E^{-1.5}$ neutrino spectrum, and slightly worse 1.4° for an atmospheric neutrino spectrum.

# Chapter 7.

# Point source search methods

This chapter provides a detailed account of the strategies and methods used in the point source analysis of this work. They are applied to the data collected with 22 strings of the IceCube detector after the event selection described in the previous chapter. The binned search is introduced as a technique to identify or exclude directional clustering. Its application in a systematic scan of the sky for neutrino signals is the focus of the first section. The selection of source candidates for a separate test of pre-defined directions is discussed afterwards. The final section presents a search for variable neutrino emissions, for which time information is used to investigate a particular model for hadronic acceleration processes in an AGN.

As in the previous chapter, all search parameters for the analysis presented here were optimised and fixed while keeping the directions of individual muon tracks blinded. Data with randomised right ascensions were used to estimate background rates in the event sample. The actual celestial coordinates of event directions were unblinded afterwards. Results of the individual analyses are presented in chapter 8.

## 7.1. Binned search method

### 7.1.1. Directional event clusters

**Framework**

The binned point source search is an established technique in neutrino astronomy, applied for example in AMANDA analyses like [A$^+$07b] and discussed in detail in [Ack06]. It is designed to measure the local event clustering and compare it to the background expectation, with the aim to identify excesses due to point-like signal contributions. In previous AMANDA and IceCube searches, this approach was used only in connection with almost pure samples of atmospheric neutrinos. In this work, the same method is applied to the full sample discussed in chapter 6 that includes events from above the horizon where the background is dominated by atmospheric muons. The usage of the binning technique in such an extended search is possible since the background events are of different types but still uniformly distributed, at least when limited to declination bands as detailed below.

A significant local excess of events is expected to be due to a neutrino flux from an astrophysical point source. Alternative contributions could include gamma-ray air showers. As mentioned in section 3.3, though, these fluxes would be strongly suppressed at energies above $\sim$ 100 TeV which are the focus of this analysis. A point-like annihilation signal from accumulations of dark matter, gravitationally trapped e.g. in our Sun or the centre of the galaxy, would also be limited to energies below a few TeV according to current bounds. For a discussion of these fluxes and recent results from dedicated dark matter searches with IceCube see [A$^+$09d].

### Excess probabilities

In a binned search, probabilities for excesses of possible signal events are based only on the reconstructed directions of events in a pre-defined sample. The events that are located inside a circular bin around a given direction $\vec{d}$ in the sky constitute a spatial clustering that can be compared to background expectations. With a solid angle $\alpha$ for the bin radius, the condition for an event with direction $\vec{v}_e$ to be counted is expressed via the scalar product

$$\vec{d} \cdot \vec{v}_e \leq \cos\alpha \,. \tag{7.1}$$

This determines what *point-like* is in the context of binned neutrino searches, i.e. an emission angle which is smaller than or equal to the bin size.

To calculate the probability for observing a given number of events inside the bin assuming no signal contribution, the value has to be compared to the expected background. It is possible to use the event distribution from data for this calculation by averaging over all events in the declination band that includes the bin and has a height equal to the bin's diameter. It is important that in this way the declination dependence of the event distribution, discussed in section 6.3.2, is retained, since it applies to background and signal expectations.

The method implicitly assumes that the distribution along the right ascension is uniform. This is justified for IceCube with its location at the South Pole, since asymmetries in the detector-centric azimuth distribution are washed out by the rotation of the Earth. Only for short live times on the order of days instead of months, additional considerations are required. After extracting right ascension values for each event by transforming coordinates from the local to the equatorial reference frame the distribution averaged over the live time of 276 days shows no significant directional bias, see Fig. 7.1.

The average number of background events per bin is given by the total number $N_{band}$ in the declination band and the size of the solid angle inside the bin, $A_{bin}$,

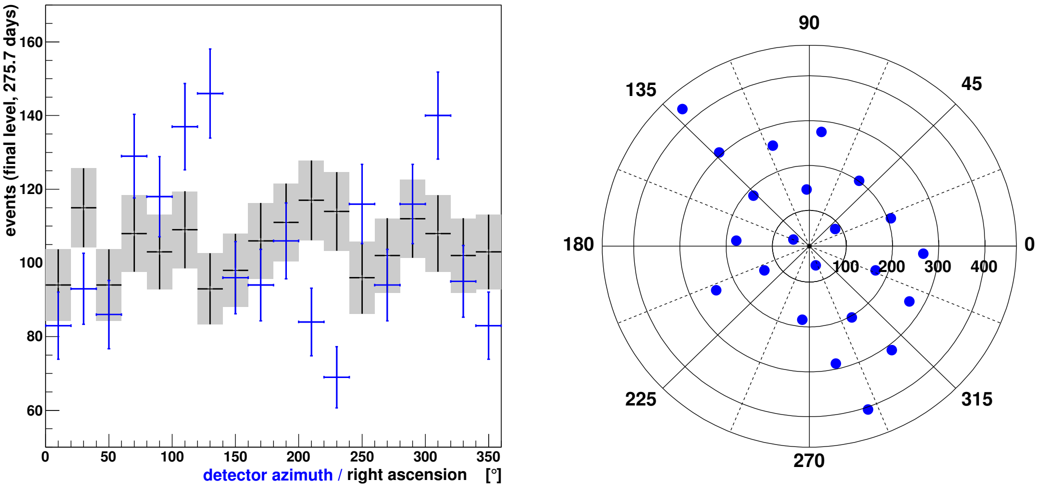

Figure 7.1.: *Left:* IceCube 22-strings final level distribution of right ascensions (black squares), derived from the reconstructed azimuth angles in detector coordinates (blue triangles). The latter distribution bears a non-uniform signature due to the asymmetric detector configuration displayed on the right. *Right:* Positions of the first 22 IceCube strings with radial distances in meters and azimuth angles in degrees.

relative to that of the band, $A_{band}$:

$$b = \frac{A_{bin}}{A_{band}} N_{band} \, . \tag{7.2}$$

Centred around the declination $\delta_d$ and extending to $\delta_d \pm \alpha$, the solid angle of the band is

$$A_{band} = 2\pi \left( \sin(\delta_d + \alpha) - \sin(\delta_d - \alpha) \right) \tag{7.3}$$

and that of the bin

$$A_{bin} = 2\pi \left( 1 - \cos(\alpha) \right) \, . \tag{7.4}$$

To derive the probability for observing $n$ events in a bin given the total number of events in the band, the expectation $b$ is not used directly, but enters through a binomial description of accumulating individual events. The probability function directly depends on the number $N_{band}$ of events in the band as

$$P(n|N_{band}) = \binom{N_{band}}{n} p^n \, (1-p)^{N_{band}-n} \, , \tag{7.5}$$

with the individual probabilities for an event to be located inside the bin given by

$$p = \frac{A_{bin}}{A_{band}} = \frac{1 - \cos(\alpha)}{\sin(\delta_d + \alpha) - \sin(\delta_d - \alpha)} \,. \tag{7.6}$$

This prescription involves also the events inside the search bin in the estimation of background, including a possible signal contribution. The underlying assumption is that the number of signal neutrinos is negligible when compared to the total background. The general isotropy observed in the right ascension distribution and the negative results of previous searches justify this approach. If a signal contribution is present anywhere in the band the background is overestimated, resulting in conservative probability values for any excess and hence no false discovery claims.

### Significances and upper limits

The $P(n|N_{band})$ from (7.5) is the probability of observing exactly $n$ events for a given number of background events. To obtain the more meaningful probability for an equal or larger excess to occur due to random fluctuations, one has to sum over all $P(n|N_{band})$ values for $n \geq n_{\text{obs}}$[1]:

$$\text{P-value} = \sum_{n=n_{\text{obs}}}^{\infty} P(n|N_{band}) \,. \tag{7.7}$$

This probability is called P-value. When testing a large number of directions, large excesses and hence very small P-values can occur and it is common practice to state the results for the largest excesses as $-\log_{10}(\text{P-value})$, called the excess parameter. This value represents the significance of having observed a neutrino point source if only one direction is tested. A scan over multiple bins requires to consider trial factors as explained below. The significance can be expressed in terms of standard deviations of a Gaussian function, determined by the point from where the area under the one-sided Gaussian tail (to the right) equals the P-value. An excess with a significance $> 3\sigma$ would be considered an indication for a source at the bin's position, and in the case of a result $> 5\sigma$ a discovery could be claimed.

To quantify a flux necessary for a point source detection, one can determine the number of observed events equivalent to a $5\sigma$ excess. Based on the average background per bin one derives the required signal addition to achieve this $5\sigma$ level in 50% of all trials. Simulated signal neutrinos, generated and processed as outlined in section 4.2, are used to translate this excess into a neutrino flux value, in the same way as introduced in section 3.2.2 for limit conversion. Thus one obtains a discovery potential for the IC-22 event selection in the form of a required point source flux. This was calculated as a function of declination for both $E^{-2}$ and $E^{-1.5}$ spectra and with a search bin radius of 2.5°, shown in Fig. 7.2.

---

[1] In case of an event deficit, the sum runs over $n \leq n_{\text{obs}}$.

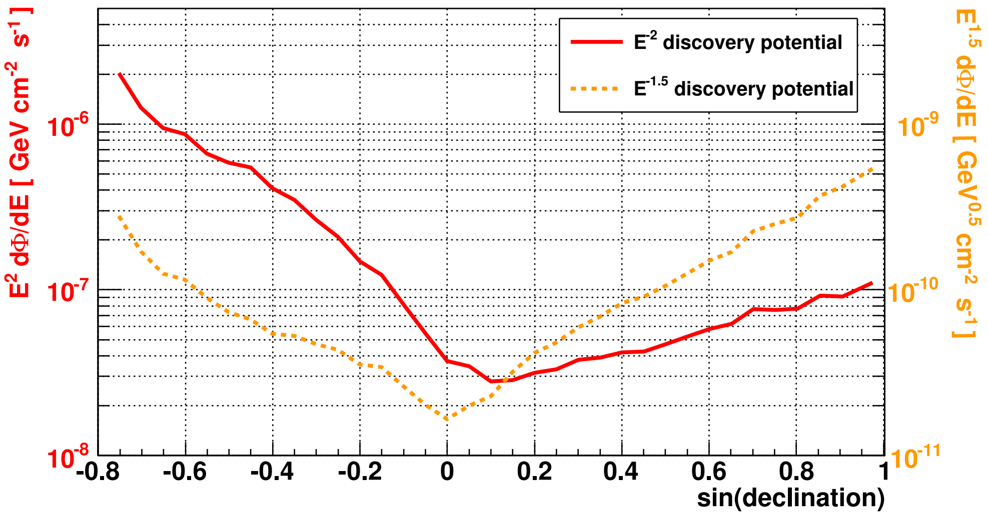

Figure 7.2.: Point source flux required for a $5\sigma$ discovery in 50% of trials as a function of declination. The axes are scaled differently for the $E^{-2}$ spectrum (red solid) on the left side and the $E^{-1.5}$ spectrum (orange dashed) on the right.

If a bin contains no significant excess and hence is compatible with the background hypothesis, one can calculate the maximum signal contribution which could be present. Section 3.2.2 introduced the prescription for such an event upper limit $\mu_{90}$ following the construction of [FC98] with the confidence level (CL) set to 90%. Relying on a simulated neutrino flux, equation (3.17) allows transforming $\mu_{90}$ into an upper limit $\Phi_{lim}$ for the point source flux from the direction of the bin. The same method can be applied if an event excess is a significant indication for a signal contribution. In this case, both the lower and upper limits from the confidence belt construction can be used to derive a range of estimated neutrino fluxes.

The average upper limit on the flux, obtained from a pure background sample, is called sensitivity and was defined in equation (3.18). It was already used to optimise the cuts and bin radius in chapter 6. In Fig. 7.3 the sensitivity is shown as a curve in dependence of declination. It follows the behaviour of the discovery potential in Fig. 7.2, mainly determined by absorption of high energy neutrinos in the up-going regime (on the right) and the background suppression cuts increasing with the angle above the horizon (on the left).

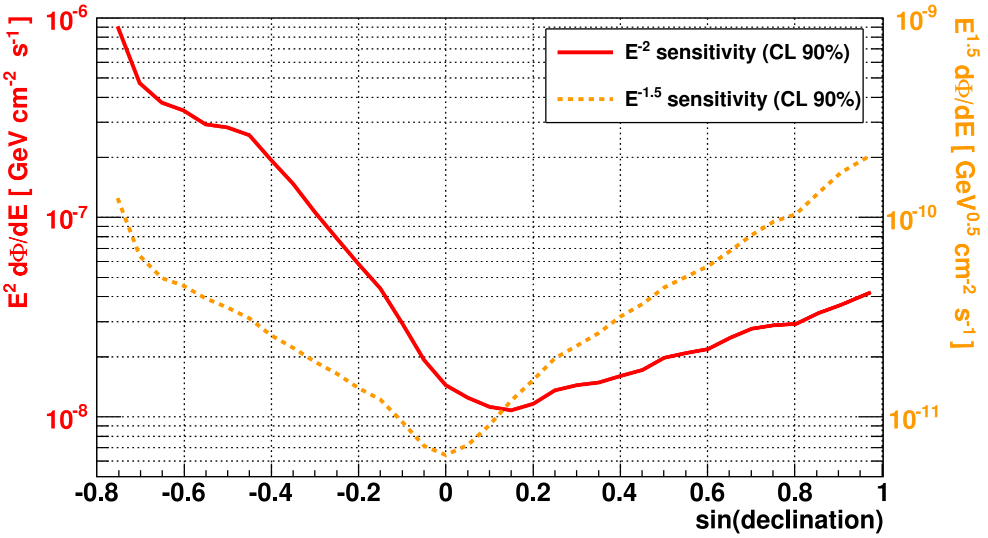

Figure 7.3.: Point source sensitivity as a function of declination. The axes are scaled differently for the $E^{-2}$ spectrum (red solid) on the left side and the $E^{-1.5}$ spectrum (orange dashed) on the right.

### 7.1.2. Sky map scan

Except for the Sun and supernova 1987A (see e.g. [MSS$^+$04] for details), no astrophysical neutrino point source has yet been identified. At GeV or higher energies, no direct indication for any neutrino source exists. This motivates an unbiased search in the accessible part of the sky. For the IceCube analysis presented here, the field of view encompasses the northern hemisphere as well as, for the first time, a large part of the southern hemisphere, down to $-50°$ declination, as discussed in section 6.3.1.

In the binned approach the sky is covered with circular search areas (bins), their centres defined by a grid. The radius of each bin is 2.5°, fixed after an optimisation procedure described in section 6.3.2. To cover every part of the sky, the bins overlap with each other. The distance between bin centres is chosen to be small enough to provide a precise sampling of possible point source locations. Since signal neutrino directions would be distributed around a source according to the point spread function of the track reconstruction, a given bin position might only contain part of the events with origins between grid points. This would reduce the chance of discovery, since it could be that none of the bins contains all detected neutrinos from this source. To avoid this, a smaller separation is preferable, resulting in a denser grid than required for a simple coverage of the full area.

A closer spacing also increases the number of search bins and one could expect that accounting for these additional trials would reduce the significance of an observation too much at some point. Nevertheless, as discussed in [Hau04], the strong correlation between counts in overlapping bins does not change the probabilities much, and the necessary corrections, called trial factors, are included in the treatment presented in the following section.

The optimal grid spacing was studied further in [Ack06], and showed a broad range of stable discovery potential for separations smaller than the bin size. Since the angular resolution (minimum $\sim 1.5°$) and the number of events ($\sim 4000$) were similar to those of the IceCube search, the same value of 0.5° separation between two bin centres in right ascension and declination was adopted here.

The probability for observing $n$ events in a bin depends on the number $N_{band}$ of (background) events in a declination band according to equation (7.5). This relation introduces a statistical uncertainty on the total background rate per band. Furthermore, it precludes the application of the binned method, or any method relying on the comparison to measured background, in the northernmost regions, where the total space angle per band becomes too small. Consequently, declinations $> 85°$ are excluded from the search. This reduces the number of events in the final sample for IC-22 from 1885 to 1877.

### 7.1.3. Trial correction

To correctly calculate significances for event excesses, the number of repeated observations (called trials) has to be taken into account. The P-value of each binned event count as described in equation (7.7) is referred to as *pre-trial* probability. When performing a number of independent tests, which here applies to non-overlapping bins, the *post-trial* probability for observing $n_p \geq n$ events at least once can be easily expressed. For $k$ trials and a fixed background $N$ in the band it is

$$\mathcal{P}_k(n_p > n) = 1 - \left( \sum_{i=1}^{n-1} P(i|N) \right)^k , \tag{7.8}$$

where $P(i|N)$ is the binomial probability from (7.5). In the case of the sky map search, this simple expression is not applicable, since overlapping bins lead to correlated probabilities in the summation over individual possibilities. While an analytical calculation is in principle possible, as outlined in [Ack06], the large number of bins on the order of 10,000 would lead to extreme computational demands for such an approach.

A more practical method is to use Monte Carlo techniques to generate randomised sky maps, on which the same point source search can be performed. In each case, right ascension angles in the final sample are replaced by random values, thus retaining the declination dependence but erasing any possible signal accumulation in the event distribution. By determining the fraction of generated maps featuring a lower chance probability for the maximum excess than a given observation, the post-trial significance for the bin with the strongest clustering can be evaluated.

## 7.2. Selection of source candidates

### 7.2.1. Motivation and outline

In chapter 2, various scenarios for astrophysical neutrino production were introduced. They can be used to compile a list of known astronomical objects that are good candidates for neutrino generation above TeV energies. Testing the hypothesis of having a neutrino point source among these objects significantly reduces the trial factors compared to the full sky map search discussed in the previous section. It is therefore reasonable to perform such a separate search on a sample of promising source candidates. The binned technique described above is applied by taking each astronomical source position as centre of a search bin and calculating individual significances and limits based on the event count.

With respect to the full sky, a scan of an a priori selected list of objects is a test of a separate hypothesis, related to specific model predictions. Thus, the final P-value from each search is considered to determine the overall compatibility with background as the lowest of these, but the trials have to be counted. The correlation between the two can be neglected, since even a list of tens of sources covers only a very small fraction of the total number of directions in the sky. The trial corrected significance for the largest excess from both searches is calculated by inverting the probability for having twice a value below the one observed. With $P_l$ as the lowest P-value from both searches, this leads to:

$$1 - (1 - P_l)^2 \approx 2 \cdot P_l \ \text{ for } \ P_l \ll 1 \,. \tag{7.9}$$

This trial factor, accounting for two tests of the overall background hypothesis, would have to be further corrected with respect to other separate searches on the same sample, as those described later. However, the total correction on the order of a few is small compared to the $5\sigma$ threshold for discovery ($\sim 10^{-7}$). It thus needs to be considered only if a final P-value is close to the $5\sigma$ threshold. In contrast to this, the trial corrections from scanning various directions or sources in one test are much larger and are always taken into account.

The event selection for this work focuses on optimal performance for very high energies (roughly $> 100$ TeV), in particular above the horizon where less energetic signals are suppressed together with the background. As discussed in chapter 2, extra-galactic sources are likely to contribute significantly to the cosmic ray and neutrino flux at these energies, with AGN as prime candidates. Consequently, the source list described in the following was designed as a systematic selection of such objects, based on gamma-ray observations and other photon data.

A list compiled for a separate point source search also using IC-22 data, analysing only upward going tracks [A$^+$09c], included many sources detected at TeV energies by IACTs. While particle acceleration up to very high energies is guaranteed in these objects, the fact that a significant part of the TeV photons escapes the local environment of the source might indicate that proton-photon interactions are not very efficient. The result would be only a low neutrino flux, as argued for example in [NS02]. For this reason and to provide a complementary selection to [A$^+$09c], TeV gamma-ray observations were not considered as a criterion for the compilation of source candidates here.

### 7.2.2. Systematic selection of bright gamma-ray sources

The theoretical motivation for the source selection presented in the following is given by hadronic acceleration models for AGN with a special focus on blazars, as introduced in section 2.2. The interactions of high energy protons with photon fields, see section 2.1.3, lead to a decay chain producing gamma-rays and neutrinos, possibly up to EeV energies.

Calculations of spectral energy distributions (SEDs) for photons and the prospects of neutrino emission from low-luminosity blazars (BL Lac objects) according to [MPE$^+$03] were described in section 2.2.3. As discussed on p. 16, photon target densities in HBLs seem to be so low that accelerated protons lose their energy primarily through synchrotron radiation and thus do not allow efficient neutrino production. LBLs on the other hand are more likely to provide conditions that generate a detectable neutrino flux. In this case, a significant gamma-ray flux at GeV up to TeV energies is expected, primarily due to synchrotron or pion cascade radiation originating from the hadronic acceleration processes.

Model predictions for high-luminosity blazars classified as Flat Spectrum Radio Quasars (FSRQ) are presented in [AD04], as introduced on p. 16. In contrast to BL Lac objects, the existence of UV and soft X-ray radiation fields produced near the accretion disk of an FSRQ guarantees more target photons for photoproduction of mesons which then decay into neutrinos. These radiation fields are called external since they are not produced through particle acceleration processes. Internal photon fields vary with time in dependence of the changing jet structures, while external targets are always present and lead to a steady neutrino rate. The calculations in [AD04] for FSRQs predict gamma-rays with a spectral cut-off at GeV energies, hence in general one does not expect a large TeV photon flux. This is supported by the fact that only two such sources have been discovered by IACTs, see also section 7.3.

The two hadronic models for BL Lac objects and FSRQs reviewed here both feature GeV gamma-ray fluxes scaling with the same hadronic interaction rate that induces neutrino generation. Thus, a correlation of the amplitudes from both emissions is expected and a list of promising candidates for neutrino searches among FSRQs and LBLs can be composed by using gamma-ray fluxes as a main

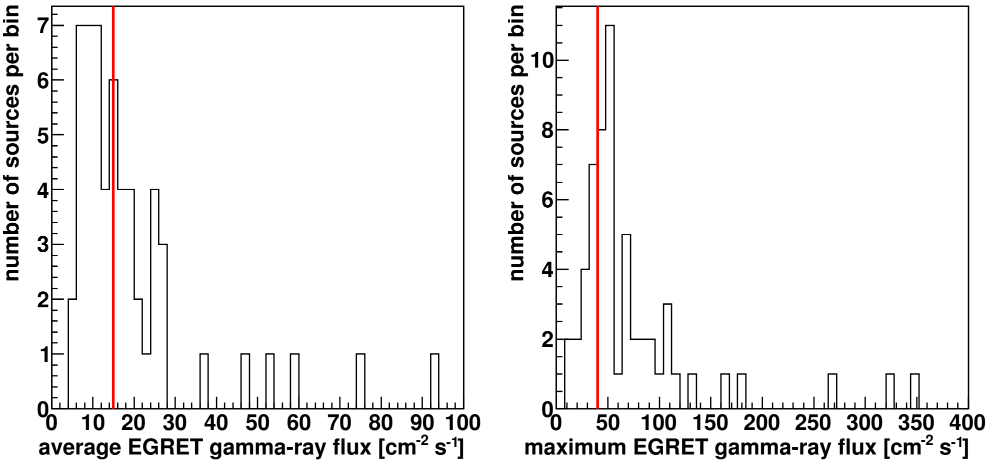

Figure 7.4.: Distributions of the average (left) and maximum (right) gamma-ray fluxes of 57 sources detected by EGRET with confirmed AGN counterparts and declinations $\delta > -45°$. The red lines indicate the thresholds chosen for the point source search selection.

selection criterion.

At the time the source selection was finalised (November 2008), the most comprehensive catalogue of objects with gamma-ray emissions at GeV energies was the third EGRET catalogue [H+99]. The data collected with the EGRET experiment on the *Compton Gamma Ray Observatory* satellite contain 67 confirmed AGN observations, defined as gamma-ray flux measurements for which an extragalactic counterpart object could be identified at 95% confidence level. For each of these sources, flux measurements from several viewing periods are available. A classification for these confirmed AGN is given in [N+07] and can be used to select BL Lac objects and FSRQs, which make up 62 out of 67 detections.

This list of bright blazars was used as a starting point for a systematic application of simple selection criteria. Only objects with declinations $> -45°$ were selected to guarantee that a bin around each would be fully within field of view of this analysis. Without modelling individual source spectra, two generic thresholds on the gamma-ray flux were defined, one on the maximum amplitude to identify the strongest emitters and one on the average flux over all observations periods to guarantee a certain baseline emission. The latter is important for a steady search covering the time span of one year that is less sensitive to large but short fluctuations. The distributions of these parameters are shown in Fig. 7.4. The threshold values of $15 \times 10^8$ cm$^{-2}$ s$^{-1}$ for the average and $40 \times 10^8$ cm$^{-2}$ s$^{-1}$ for the maximum flux at energies $> 100$ MeV were simply chosen to select a reasonably large fraction of the sources, in lack of precise theoretical criteria. The resulting 23 objects are listed in Table 7.1 together with the additions from the next section.

| object | EGRET identifier | type | redshift | r.a. [°] | dec. [°] |
|---|---|---|---|---|---|
| EGRET*selection* | | | | | |
| PKS 0537-441 | J0540-4402 | LBL | 0.89 | 85.02 | $-44.05$ |
| PKS 1622-297 | J1625-2955 | FSRQ | 0.82 | 246.36 | $-29.92$ |
| PKS 1622-253 | J1626-2519 | FSRQ | 0.79 | 246.50 | $-25.32$ |
| PKS 1830-210 | J1832-2110 | FSRQ | 1.00 | 278.10 | $-21.18$ |
| PKS 1730-130 | J1733-1313 | FSRQ | 0.90 | 263.46 | $-13.23$ |
| PKS 1510-089 | J1512-0849 | FSRQ | 0.36 | 228.17 | $-8.83$ |
| PKS 1406-076 | J1409-0745 | FSRQ | 1.49 | 212.42 | $-7.75$ |
| QSO B2022-077 | J2025-0744 | FSRQ | 1.39 | 306.36 | $-7.75$ |
| 3C 279 | J1255-0549 | FSRQ | 0.54 | 193.98 | $-5.82$ |
| PKS 0336-01 | J0340-0201 | FSRQ | 0.85 | 55.04 | $-2.02$ |
| PKS 0420-01 | J0422-0102 | FSRQ | 0.91 | 65.65 | $-1.04$ |
| 3C 273 | J1229+0210 | FSRQ | 0.16 | 187.25 | 2.17 |
| 4C +10.45 | J1608+1055 | FSRQ | 1.20 | 242.12 | 10.93 |
| 4C +11.69 | J2232+1147 | FSRQ | 1.04 | 338.11 | 11.80 |
| PKS 0528+134 | J0530+1323 | FSRQ | 2.06 | 82.74 | 13.38 |
| 3C 454.3 | J2254+1601 | FSRQ | 0.86 | 343.51 | 16.02 |
| PKS 0235+164 | J0237+1635 | LBL | 0.94 | 39.36 | 16.59 |
| QSO B0827+2421 | J0829+2413 | FSRQ | 2.05 | 127.49 | 24.22 |
| QSO B0430+2859 | J0433+2908 | LBL | 0.97 | 68.40 | 29.14 |
| QSO B1611+3420 | J1614+3424 | FSRQ | 1.40 | 243.54 | 34.40 |
| 4C +38.41 | J1635+3813 | FSRQ | 1.81 | 248.92 | 38.22 |
| 4C 51.37 | J1738+5203 | FSRQ | 1.38 | 264.64 | 52.05 |
| 8C 0716+714 | J0721+7120 | LBL | 0.30 | 110.43 | 71.34 |
| *additions* | | | | | |
| PKS 1454-354 | - | FSRQ | 1.42 | 224.36 | $-35.65$ |
| PKS 1502+106 | - | FSRQ | 0.56 | 226.10 | 10.49 |
| M87 | - | radio galaxy | 0.0043 | 187.71 | 12.39 |
| Centaurus A | J1324-4314 | radio galaxy | 0.0018 | 201.37 | $-43.02$ |
| Sgr A* | J1746-2851 | galactic centre | - | 266.42 | $-29.01$ |

Table 7.1.: Source list composed of 23 blazars, selected based on GeV gamma-ray measurements with EGRET, and five additional promising neutrino source candidates.

### 7.2.3. Individually selected candidates

In addition to the third EGRET catalogue, the results AGILE [T$^+$01, M$^+$00] and FERMI [RMM07] satellite gamma-ray experiments presented by November 2008 were scanned for further blazar observations. As no repeated measurements and hence average fluxes were available, only the threshold on the maximum flux of photons with energies $> 100$ MeV was applied, as well as the requirements that the source object could be identified as a blazar and lies within the field of view of this IceCube analysis. This led to two additions to the source list, the FSRQs PKS 1454-354 and PKS 1502+106, reported by the FERMI LAT collaboration in [Cip08] and [Mar08].

Two AGN were added even though they are not blazars, having jets that are not pointing towards Earth. One is M87, a radio galaxy that lies at a distance of $\sim 16$ Mpc and thus relatively close to our galaxy. The misalignment between the jet and the axis of observation might be small enough to allow for a measurable neutrino flux due to hadronic acceleration based on the blazar model discussed in [PDR03]. This prediction features very high energy neutrinos with a large contribution above 10 PeV. The position of the source at 12.4° below the horizon would lead to absorption of a large fraction of these neutrinos inside the Earth. Nevertheless, this unique object is a promising candidate in a dedicated search at high energies. Furthermore, the object was observed in TeV gamma-rays by several IACTs, first reported in [A$^+$04b].

The second AGN addition is the radio galaxy Centaurus A. In contrast to M87 it is included in the third EGRET catalogue as an identified source, but with a flux slightly below the threshold values chosen for the systematic selection above. The decision to make it part of the source list relies mainly on the report on an anisotropy in the charged cosmic ray distribution at energies above $\sim 56$ EeV by the Pierre Auger collaboration in [A$^+$07a, A$^+$08d]. The direction of Centaurus A is correlated with an event accumulation that can be considered a 'hotspot' of cosmic rays. In addition, it was recently revealed as a TeV gamma-ray emitter [A$^+$09k] and is the closest known AGN, at a distance of $\sim 3.8$ Mpc [HRH09]. All this makes Centaurus A a prime candidate for being a cosmic ray source. With a declination of $-43°$, Centaurus A is an object of the southern sky. Thus, extending the field of view for point sources above the horizon is crucial for including it in IceCube searches.

Finally, the presumptive super-massive black hole Sgr A$^*$ at the centre of our galaxy was also included in the list of candidates. As the only galactic object, it is assumed to be the least likely object in this selection to produce a large neutrino flux at PeV energies or above. Nevertheless, it is considered a promising candidate, with neutrino predictions for example in [AN05]. Its position at a declination of $-29°$ prevented it from being observed in any previous point source analysis with AMANDA or IceCube.

In total, 28 neutrino source candidates were selected, of which all but three are blazars, chosen due to their strong GeV gamma-ray emission.

## 7.3. Time dependent analysis of 3C279

### 7.3.1. Motivation

**Flare search**

For many AGN observed at GeV to TeV energies, the measured photon fluxes at all wavelengths exhibit strong variability, on time scales sometimes as short as an hour or less. Short outbreaks of this kind are called *flares*. If one assumes a direct correlation of these emissions to hadronic particle acceleration, as motivated above, neutrino flares should happen in the same time periods. The possibility of small time shifts would still be possible, depending on the details of the acceleration process. By using the arrival time of each event in the final IceCube sample, the search for neutrino excesses can be limited to the most promising time windows. They are determined based on the available data on fluctuations in the photon flux at various wavelengths. This approach significantly reduces the number of background events compared to those accumulated for the live time over a full year. Thus, the sensitivity to short, strong bursts of neutrinos in these periods is increased, allowing better tests of models that predict flux correlations for known flares.

**Source selection**

The hadronic model from [AD04], see section 7.2, highlights FSRQs as one of the most promising source classes for neutrino astronomy. The calculations themselves rely on data related to a gamma-ray flare and provide motivation for a time-dependent search for neutrino emission in correlation with periods of raised photon fluxes for objects of this type. Predicted neutrino spectra have strong contributions above $10^5$ GeV and extend to EeV energies. This suggests to restrict the dedicated flare analysis to objects with declinations near or above the horizon, where absorption does not preclude detection of neutrinos with such energies. Of all bright FSRQ candidates in the field of view, only for one sufficient data at various wavelengths was publicly available: the quasar 3C279 located in the southern hemisphere at a declination of $-5.8°$. Therefore, the flare search for the IC-22 data sample presented here focuses only on this one source.

The quasar 3C279 stands out among all other systematically selected EGRET AGN as the first FSRQ that has been observed as a TeV gamma-ray source, reported by MAGIC in [A+08h]. Also the fact that it is the most distant very high energy (VHE) gamma-ray observation, at a redshift of 0.54, makes it a remarkable source. The GeV gamma-ray data from EGRET and a large amount of measurements in other wavebands from different experiments present a chance to study

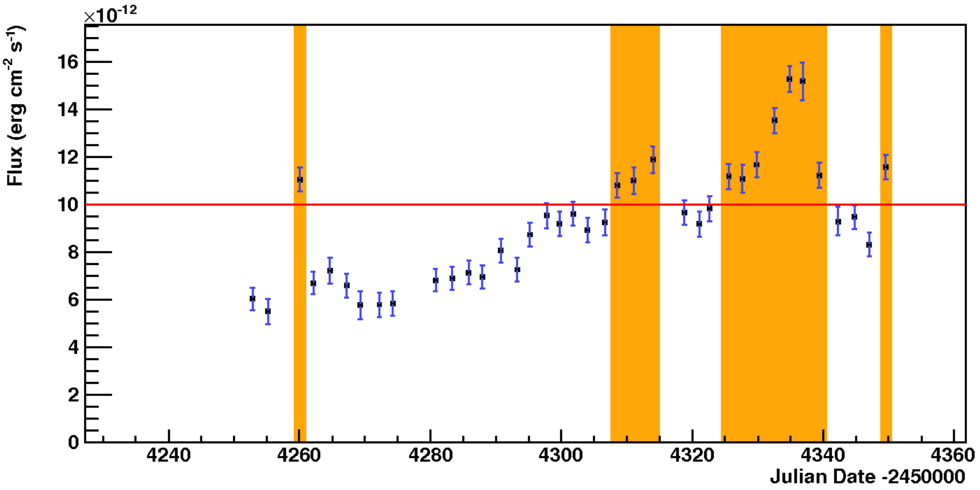

Figure 7.5.: X-ray fluxes of 3C279 measured by the RXTE satellite between June and September 2007. The areas shaded in orange mark the period selection for the neutrino flare search based on a flux threshold indicated in red. Plot based on data from [L$^+$08] provided by A. Marscher.

the variability of 3C279 in the context of correlations between different photon energies.

By using observations in the optical and X-ray bands taken simultaneously with the MAGIC measurements, an attempt to fit the SED of 3C279 with models that are either leptonically or hadronically dominated was presented in [BRM09], see also Fig. 2.5. A leptonic scenario explaining the VHE gamma-rays with Compton up-scattering of internal or external photons based on a single emission region does not plausibly reproduce the observed spectrum. Only a more complex approach with multiple zones for acceleration in the jet gives better fits to the measurements. On the other hand, a hadronic model along the lines of the synchrotron proton blazar (see p. 2.2.3) and with a single emission region can also accommodate the different observations. The latter scenario from [BRM09] was expanded in [Rei09] by calculating neutrino flux predictions which are the main motivation for the flare search presented here.

## 7.3.2. Definition of flare search parameters

The selection of search periods for 3C279 was based on X-ray and optical measurements published in [L$^+$08] and shown in Fig. 7.5. Only the overlap with the IC-22 live time (May 2007 to April 2008) is of interest here and thus results in a restriction of the considered search periods to the months May to September 2007. Following the discussion in [BRM09], X-ray high states were used as the major selection criterion and led to two periods of interest, one in June and one in August to September. The optical data is sparser, in particular after July where the source was located too close to the Sun to allow observations. Based on gradual changes in the optical light curve it was extrapolated that a high state observed in July prevailed until August and possibly up to September. The level of optical photon flux is high though not flaring. The same behaviour was observed during the gamma-ray flare detected by MAGIC and discussed in [BRM09].

Since the MAGIC discovery was made in 2006 and no GeV data was taken in 2007, gamma-ray observations of 3C279 were not publicly available for the time covered by IC-22 data. Finally, only the X-ray data were used to define the precise search periods. These data, taken with the *Rossi X-ray Timing Explorer* (RXTE) satellite instrument, cover energies between 2.4 and 10 keV. By interpolating between sampling points, lying up to 3 days apart in the periods of interest, a threshold of $1 \times 10^{-11}$ erg cm$^{-2}$ s$^{-1}$ was used to identify states of highest emission, see Fig. 7.5. Lower thresholds did not yield additional obvious flare-like structure and were dismissed. The length of a neutrino flare and possible shifts with respect to the X-ray high states can not be extracted from the model, since they might well depend on jet flow parameters that change from one event to the other. Nevertheless, one can reasonably assume time scales on the order of days as in the case of the observed gamma-ray flare. A minimum window of one day before and after each selected X-ray flux point was chosen. The selection led to four periods given here in Modified Julian Days (MJDs)[2],

- 54258.6 to 54260.6,
- 54307.0 to 54314.5,
- 54324.1 to 54339.9,
- 54348.0 to 54350.0,

adding up to a total of 25.4 days if integrated over the actual detector live time of IceCube.

The reduction of analysis live time compared to the 276 days covered by the full IC-22 sample results in a lower number of background events. This change in the signal to noise ratio made it desirable to re-optimise the bin size. For the assumption of continuous neutrino emission during the selected time window of 25.4 days, a bin radius of 4° was found to yield the best sensitivity. The cumulative plot of angular differences between true and reconstructed directions for simulated neutrinos in Fig. 7.6 shows that more than 90% of the events from $E^{-2}$ or $E^{-1.5}$ signal spectra have deviations less than 4°.

---

[2] Julian Days (JDs) are an astronomical time scale, counting days since January 1, 4713 BC Greenwich noon. An MJD date is defined as JD minus 2400000.5 .

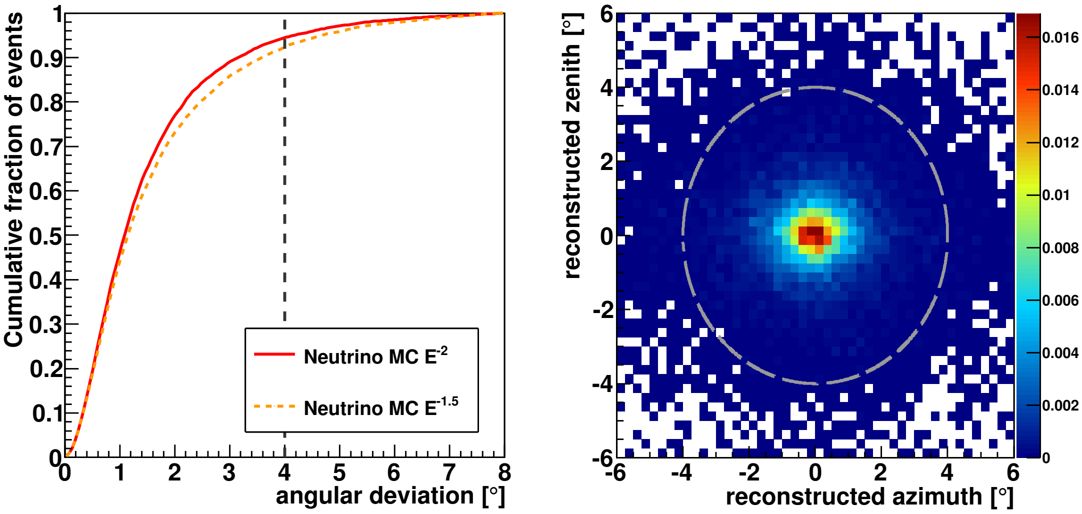

Figure 7.6.: Angular deviations for MPE-reconstruction of simulated neutrinos near the location of 3C279 (dec. −5.8°). On the left, the difference between true and reconstructed direction is shown as cumulative fraction of events, on the right the point spread function is illustrated. The chosen bin radius of 4° is indicated.

### 7.3.3. Application to the event sample

In general, the determination of significances and event or flux limits for a flare search is the same as described in section 7.1, only applied to a further restricted data sample. The one aspect that needs to be revised is the estimation of background event numbers. A more elaborate method than a simple averaging is necessary due to two causes for systematic deviations on small time scales. These are the seasonal variations discussed on page 71 of section 6.2, here applying to the muon background at the location of 3C279, and the azimuthal detector asymmetry displayed in Fig. 7.1. Both average out over the live time of a full year, the former by integration over a full cycle and the latter through the rotation of the Earth. But depending on the detector orientation, they lead to significant deviations in the event distributions on time scales on the order of a few days or less.

To cope with these time structures, a fit of the full year data can be used to model the changing rates in dependence of time during the year and right ascension of the tested directions. This allows to derive precise background estimates for specific time periods. The method was described in [BABL09] in the context of a more general neutrino flare search, for which it was developed. It was used here to derive an individual background estimate for each of the four search periods described above. This leads to a total background expectation of 0.52 events within a search bin of 4° radius.

For the hadronic model of [AD04], a neutrino flux prediction was presented in [Rei09]. Using this as input for a sample of simulated neutrinos (with a full detector processing chain, see section 4.2), a signal expectation of 0.13 events was derived under the assumption of continuous emission during the search periods. Accordingly, the probability for a deviation from the background-only value that would be equivalent to five standard deviations is very slim, around $10^{-6}$. Only a flux about 100 times larger would lead to a discovery potential of the order of a few percent.

Even with large model uncertainties this is probably not realistic. On the other hand, the flare detected by MAGIC indicates a large emission of TeV photons, requiring a relatively high transparency. Changing the model conditions in the acceleration region might well produce higher photon-proton interaction rates, resulting in less TeV photons but a higher neutrino rate with a larger discovery potential. Independent of the expected fluxes, this dedicated test is the first neutrino flare search for this object and guarantees new limits extending into the PeV energy range.

# Chapter 8.

# Point source search results

In the following sections, the results from applying the search methods described in the previous chapter to the data taken with IceCube with 22 strings in operation are presented. First, the largest excesses of binned event counts and overall significance distributions from the sky map search and the test of 28 candidate neutrino sources are discussed. The subsequent section presents the results from the time-dependent analysis of potential flare periods for the blazar 3C279.

The systematic uncertainties with respect to the background composition and the signal simulation accuracy are studied and summarised. Final flux limits are discussed in the last section in relation to astrophysical neutrino production models.

## 8.1. Sky map results

### 8.1.1. Largest excesses

The sky map of unblinded event coordinates, reconstructed with the MPE likelihood algorithm, is shown in Fig. 8.1. Each black dot represents the direction of one of the 1877 reconstructed muon tracks, predominantly produced by atmospheric neutrinos from the northern and air shower muons from the southern hemisphere.

For each bin used to scan this map, the probability that the same or a larger number of events accumulates in this search area is calculated according to equation (7.7). Its negative logarithm, the excess parameter, corresponds to the colour of each bin in Fig. 8.1, pointing to the deviations from the background-only hypothesis.

The largest excess can be found in the two overlapping bins centred at right ascension (r.a.) 103.0°/103.5° (6.9 h) and declination (dec.) 1.0°, close to the celestial equator. They each contain 8 events with a background expectation of 1.19, based on 109 events in the full declination band. This results in a pre-trial P-value of $2.9 \times 10^{-5}$ which translates to an excess parameter of $-\log_{10}(\text{P-value}) = 4.54$ equivalent to $4.02\sigma$ in units of standard deviations for a one-sided Gaussian tail.

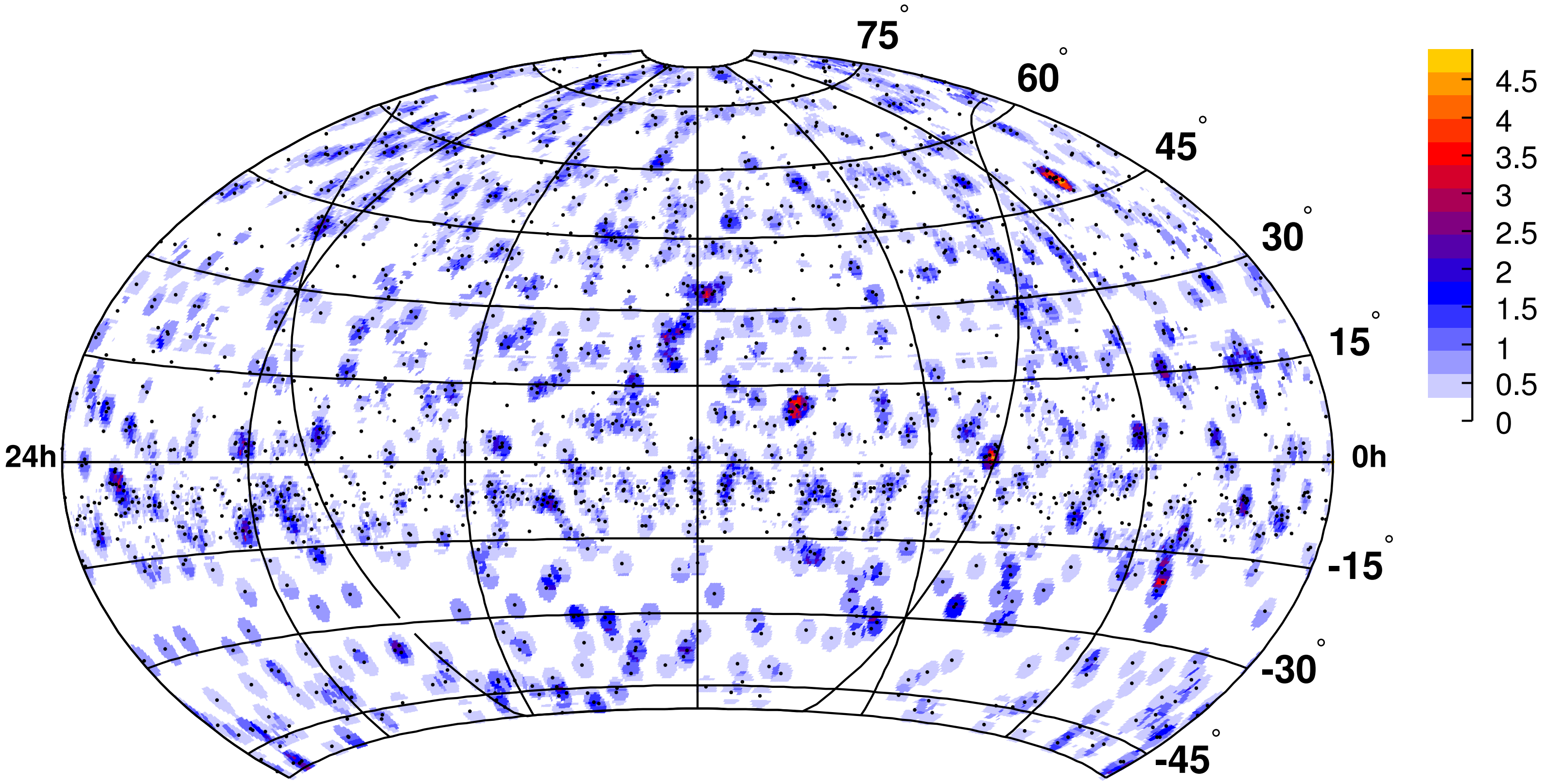

Figure 8.1.: Sky map in equatorial coordinates with 1877 IceCube events (black dots) for declinations $-50^\circ < \delta < +85^\circ$. The colours indicate the significance of upward fluctuations, i.e. $-\log(\text{P-value})$. The curved line, crossing the null meridian a few degrees north of declination 60° and reaching over both hemispheres, indicates the galactic plane.

The post-trial probability for such a maximum excess was calculated by scanning 390,000 right ascension scrambled sky maps for excesses with the same or larger significances. The resulting post-trial probability for compatibility with a background fluctuation is 37.4%, leading to the conclusion that this observation is not significant as an indication of a neutrino signal.

It is worth mentioning that the next largest excess value is located at r.a. 154.5° and dec. 11.5°, since this is close to the position of the largest upward deviation (at r.a. 153.4° and dec. 11.4°) in the likelihood analysis limited to the northern hemisphere in [A$^+$09c], based on the same IceCube raw data from 22 strings. This independent point source search covers the same time period as the data discussed here but the event selection was performed with different cuts. The resulting final sample is larger, consisting of 5114 events, though including only declinations $> -5°$. Its optimisation was also based on an $E^{-2}$ spectrum expectation for neutrino signals, favouring highly energetic muon tracks. In consequence, it is understandable that a particular accumulation of such events is identified in both approaches. The background probability for this largest excess in [A$^+$09c] is 1.34%, based on a likelihood calculation that includes the use of an energy estimator to weight the impact of each observed event. This is relatively low but compatible with background, at the level of $2.2\sigma$ after conversion to a one-sided Gaussian tail. In conclusion, both searches in the northern hemisphere are consistent with respect to their negative search results. The identification of the same large upward fluctuation in both analysis is a good indication that robust procedures for the selection of highly energetic events were used.

### 8.1.2. Significance distribution

To perform a check of the significance distribution on the sky map for consistency with an isotropic background assumption, the excess parameters from all bins in 100,000 scrambled maps were calculated. Figure 8.2 shows a histogram of the averaged distribution. The P-value used here is the probability for the same or a larger excess in case of upward fluctuations, or for the same or a lower number of events per bin in case of a downward fluctuation. The comparison to the measured values from the real sky map shows good agreement within statistical limitations, corroborating the conclusion that no significant point source signal is present in the data.

## 8.2. Source list results

For each of the 28 source candidates selected according to the procedure described in section 7.2, the number of events in a bin of 2.5° radius around its position was determined. All values are listed in Table 8.1. Depending on the observed number being an excess or a deficit compared to the expected values, the significance is

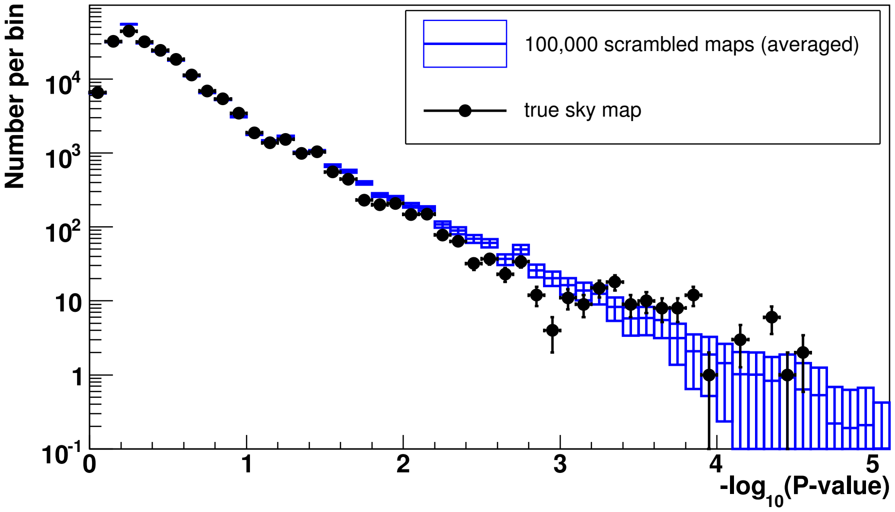

Figure 8.2.: Excess parameter distribution of the sky map search compared to averaged results from 100,000 maps with scrambled right ascensions.

calculated in the form of the P-value for either an upward or downward fluctuation of the background.

No evidence for a neutrino flux from any of the source candidates was found. The largest deviation from background expectation is an excess for the source PKS 1622-297 (Egret identifier 3EG J1625-2955) at r.a. 246.53° (16.44 h) and dec. −29.86° in the southern hemisphere. But with one observed event over an expectation of 0.25, the P-value is 22% and thus clearly not significant. The study of 390,000 randomised sky maps leads to a trial-corrected probability of 97.7% for a random fluctuation.

In the same way as for the sky map search, a comparison between the measured distribution of P-values and the one obtained from 100,000 simulated event distributions with randomised right ascensions was performed. Figure 8.3 shows the resulting histograms of excess parameters, $-\log$ (P-value). There is good agreement between observations and the background-only scenario.

## 8.3. Flare search results for 3C279

The four selected periods, 25.4 days in total, with high X-ray and optical flux states of 3C279 were tested for neutrino flares by counting events detected in these time windows. No events were found within a maximum angular distance of 4° from the source location. The upper limit at 90% confidence level on the average signal flux is 1.92 events, based on a background expectation of 0.52, see section 7.3.

This limit is a factor 15 larger than the expectation of 0.13 neutrinos derived

| source name | r.a. [°] | dec. [°] | $N_{obs}$ | $N_{exp}$ | $N_{band}$ | P-value |
|---|---|---|---|---|---|---|
| PKS 0537-441 | 85.02 | −44.05 | 0 | 0.77 | 51 | 0.46 |
| **PKS 1622-297** | **246.36** | **−29.92** | **1** | **0.25** | **20** | **0.22** |
| PKS 1622-253 | 246.50 | −25.32 | 0 | 0.16 | 13 | 0.85 |
| PKS 1830-210 | 278.10 | −21.18 | 0 | 0.30 | 26 | 0.74 |
| PKS 1730-130 | 263.46 | −13.23 | 2 | 1.23 | 110 | 0.35 |
| PKS 1510-089 | 228.17 | −8.83 | 2 | 2.44 | 221 | 0.56 |
| PKS 1406-076 | 212.42 | −7.75 | 3 | 3.21 | 291 | 0.60 |
| QSO B2022-077 | 306.36 | −7.75 | 2 | 3.24 | 294 | 0.37 |
| 3C 279 | 193.98 | −5.82 | 3 | 3.38 | 308 | 0.56 |
| PKS 0336-01 | 55.04 | −2.02 | 1 | 1.29 | 118 | 0.63 |
| PKS 0420-01 | 65.65 | −1.04 | 1 | 1.19 | 109 | 0.67 |
| 3C 273 | 187.25 | 2.17 | 0 | 1.22 | 112 | 0.29 |
| 4C +10.45 | 242.12 | 10.93 | 1 | 0.95 | 86 | 0.62 |
| 4C +11.69 | 338.11 | 11.80 | 1 | 0.89 | 80 | 0.59 |
| PKS 0528+134 | 82.74 | 13.38 | 0 | 0.97 | 86 | 0.38 |
| 3C 454.3 | 343.51 | 16.02 | 1 | 0.82 | 72 | 0.56 |
| PKS 0235+164 | 39.36 | 16.59 | 1 | 0.83 | 73 | 0.57 |
| QSO B0827+2421 | 127.49 | 24.22 | 1 | 0.77 | 64 | 0.54 |
| QSO B0430+2859 | 68.40 | 29.14 | 1 | 0.60 | 48 | 0.45 |
| QSO B1611+3420 | 243.54 | 34.40 | 2 | 0.91 | 69 | 0.23 |
| 4C +38.41 | 248.92 | 38.22 | 1 | 1.03 | 74 | 0.73 |
| 4C 51.37 | 264.64 | 52.05 | 1 | 1.41 | 79 | 0.59 |
| 8C 0716+714 | 110.43 | 71.34 | 0 | 1.33 | 39 | 0.26 |
| PKS 1454-354 | 224.36 | −35.65 | 0 | 0.54 | 40 | 0.58 |
| PKS 1502+106 | 226.10 | 10.49 | 0 | 0.95 | 86 | 0.38 |
| M87 | 187.71 | 12.39 | 0 | 0.87 | 78 | 0.42 |
| Centaurus A | 201.37 | −43.02 | 1 | 0.61 | 41 | 0.46 |
| Sgr A* | 266.42 | −29.01 | 0 | 0.26 | 21 | 0.77 |

Table 8.1.: Results for the directions in the list of source candidates with event numbers observed ($N_{obs}$), expected on average in the bin ($N_{exp}$) and summed over the full declination band ($N_{band}$). The P-value is the probability of the upward or downward fluctuation appearing in a background-only scenario.

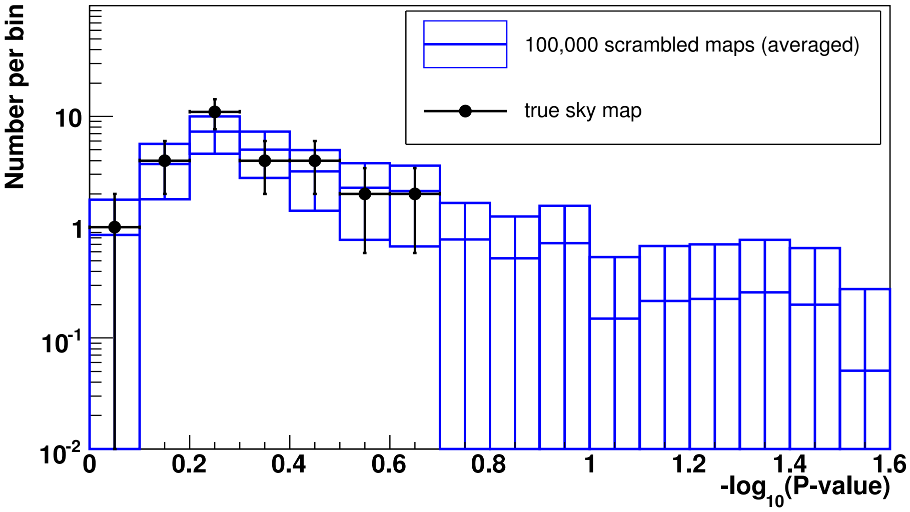

Figure 8.3.: Excess parameter distribution of the source list search compared to results from 100,000 maps with scrambled right ascensions. The latter are averaged to be of the same scale.

from the hadronic acceleration model of [Rei09] for flares in 3C279. An exclusion of the prediction is not possible with this sensitivity, but a flux limit can be obtained with the prescription from equation 3.17. It is shown in Fig. 8.4, following the shape of the model spectrum. Adopting an IceCube convention, the limit is considered to be valid only in the central energy range containing 90% of the signal events. The least and most energetic 5% of simulated events are thus excluded from the interpretation to avoid larger uncertainties due to low statistics. For 3C279, the resulting energy interval spans from $6.3 \times 10^5$ to $9.1 \times 10^7$ GeV. To obtain an integrated limit for the tested periods, one integrates the energy flux $E \cdot dE/d\Phi$ over the 90% energy range and the time of $t_p = 25.4$ days:

$$F_{ul} = \int_{t_0}^{t_p} dt \int_{E_0}^{E_1} dE\ E\ \frac{d\Phi}{dE}\ . \tag{8.1}$$

After including the systematic uncertainties as discussed in the following section, the result for the upper flux limit is $F_{ul} = 2.1$ GeV $\mathrm{cm}^{-2}$.

## 8.4. Systematic uncertainties

In the point source search presented here, the probability for an excess from a given direction was calculated by comparison to the true number of events in the same declination band. Consequently, the derived significances are directly based on the measured background level and thus very robust against any kind of

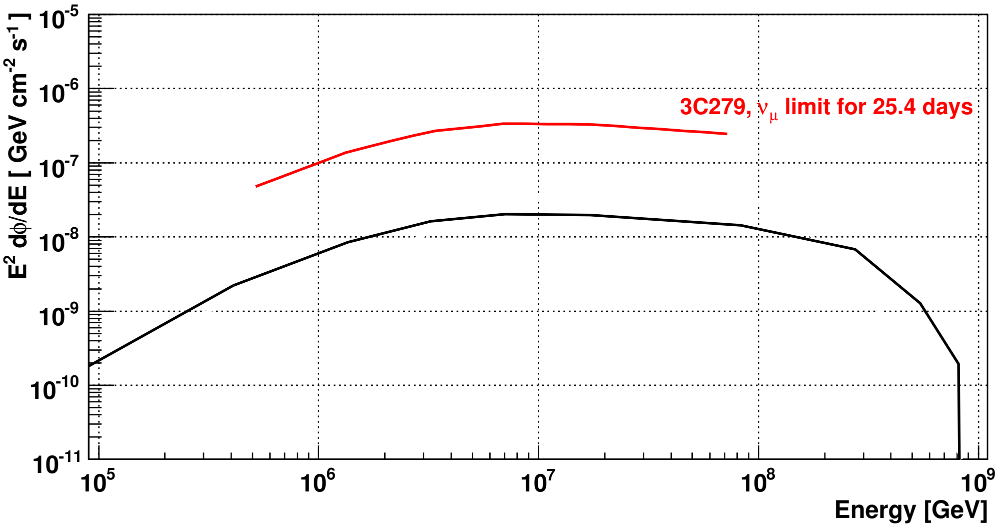

Figure 8.4.: The muon neutrino limit from the flare analysis for 3C279 covering a summed total of 25.4 days live time. The reference flux model (black line) represents the prediction from [Rei09, BRM09].

systematic effect.

To check the assumption that the background is dominated by muons originating in known air shower interactions, section 8.4.1 deals with the normalisation of the corresponding models. The only uncertainty in the background estimation that has an impact on the resulting limits stems from the limited number of events in each declination band. This effect is discussed in section 8.4.3.

Independent of the background, systematic uncertainties have to be considered when deriving flux limits from the event counts. This calculation relies on the accurate simulation of interaction, detection and reconstruction of high energy neutrinos, and the different sources and magnitudes of possible errors are the topic of section 8.4.2.

## 8.4.1. Consistency of atmospheric background fluxes

The discussion of the zenith distribution in Fig. 6.11 on page 84 already demonstrated the overall compatibility of the observed atmospheric neutrino flux from the northern hemisphere with model expectations. The statistical uncertainties of the event sample discussed here are too large to attempt a study of the different contributions from atmospheric decay chains mentioned in section 3.1.4. A more detailed comparison remains the topic of separate analyses like [Chi09], based on studies of atmospheric neutrino fluxes also at lower energies and unfolding methods for the determination of spectral shapes.

The background from above the horizon is dominated by atmospheric muons from air showers induced by charged cosmic rays in the upper atmosphere. While the energy spectrum of the primary particles is measured up to $10^{10}$ GeV, the chemical composition at ultra-high energies is poorly known. Since the number as well as the zenith and energy distribution of muons detected in IceCube depend on the types and interactions of incoming nuclei, the cosmic ray composition is a major source of flux uncertainties.

The standard IceCube background Monte Carlo data that was used here relies on the Corsika as described in section 6.1. Interactions in the atmosphere are simulated for all nuclei up to iron. Their different relative amounts are extrapolated from measurements at, following the poly-gonato model [Hoe04]. This model serves only to reproduce the galactic component of the cosmic ray flux. Furthermore, nuclei heavier than iron are not simulated in the Corsika version. For these reasons, the IceCube Monte Carlo does not correctly reproduce the observed spectrum for energies above $\sim\ 10^8$ GeV and underestimates the total flux.

Reweighting the iron component to mimic the missing events at these energies as in [Ber09] overcomes this deficit. This method was applied to the IceCube Corsika sample at the final cut level of this analysis. The following comparison with the standard background sample is considered to be a rough estimate of normalisation uncertainties of the atmospheric muon component. Double coincident events, discussed on page 69, are not regarded in these checks, since at final level only one coincident CORSIKA event survives all the cuts, thus having a statistical error of ±100%.

In the region above the horizon, declination $\delta < 0°$, the Corsika Monte Carlo data shown in Fig. 6.11 on page 84 corresponds to $637 \pm 68$ events. The changed composition leads to a new summed weight of $958 \pm 73$, i.e. an increase by 50%. When compared to the observed number of 786 events with reconstructed directions from the southern hemisphere, which include an expected $29 \pm 3$ atmospheric neutrinos, the changed composition weighting turns the deficit of muons in the Monte Carlo data into a surplus.

These total event numbers nicely bracket the measured value. Nevertheless, it has to be remarked that also a shift in the zenith distribution of the background can be observed for the two composition schemes. A pronounced deficit of simulated muons from horizontal directions remains in both cases. As can be seen from Fig. 6.11, the statistical limitations of this sample prohibit a more detailed study. The direction-dependent disagreements between measurement and simulation are in all likelihood related to an inaccurate description of light propagation in the ice layers discussed in section 4.1.1.

The conclusion from this simple background consistency check is that composition model variations and a lack of simulated events at the highest energies have a large effect on the atmospheric muon event rates at final level, of order $\geq 50\%$. The assumption of a background-dominated data sample, with atmospheric muons from above and atmospheric neutrinos from below the horizon, is consistent within the uncertainties. This justifies to base a point source search on excesses over a background level obtained from data.

### 8.4.2. Neutrino signal uncertainties

Point source results that do not constitute a discovery, which applies to all the observations presented above, can be translated into upper limits on the signal event number. They are defined by a 90% confidence level according to [FC98] as introduced in section 3.2.2. To obtain the corresponding neutrino flux limit via equation (3.17), one needs to calculate the expected number of detected neutrinos at final selection level for a given reference flux strength. This is achieved through Monte Carlo simulations, and the various systematic uncertainties are discussed and quantified in the following.

#### General simulation parameters

In the time since the neutrino Monte Carlo data for the IC-22 analyses was produced and processed, several changes were implemented in the simulation software. Probably the most important of these are new Photonics tables, see section 4.2, with finer sampling of the parameter space for photon propagation in ice. The impact on distributions of high energy neutrino signals turned out to be limited. Instead of using only the latest simulation results as reference, the difference to the previous version was considered as an estimate of systematic uncertainties due to simulation parameters in general. All reconstruction processing and event selection cuts were applied to the new Monte Carlo data to derive fractional deviations in the neutrino yield. This was done for three declination bands ($-50^\circ$ to $-10^\circ$, $-10^\circ$ to $0^\circ$, $0^\circ$ to $90^\circ$) to account for zenith dependence. For both $E^{-2}$ and $E^{-1.5}$ source spectra, the largest deviations between the Monte Carlo expectations of detectable signal neutrinos were ±5%, which was used as uncertainty value.

#### Light propagation in the ice

A major source of uncertainty is the simulation of light propagation in the ice, relying on the parametrisation of photon paths with the Photonics tables introduced in section 4.2. For a simplified uncertainty estimation, the measured scattering and absorption lengths, see page 40, can be combined in the effective propagation length, $\lambda_p = \sqrt{\lambda_e \lambda_a / 3}$. This allows to express the relative photon yield at a distance $d$ as:

$$N(d) \propto \frac{1}{d} \exp\left(-\frac{d}{\lambda_p}\right) . \tag{8.2}$$

To estimate the impact of an uncertainty of $\lambda_p$ on the order of 10%, one has to evaluate the relative change of $N(d)$ for a characteristic photon travel length $d$. The distance of closest approach between the reconstructed track and the centre of gravity of all hit DOMs is smaller than 20 m for 60–90% of all events, depending on energy and declination, as shown in Fig. 8.5 for simulated neutrinos. This demonstrates that the sample is not dominated by bright tracks outside the

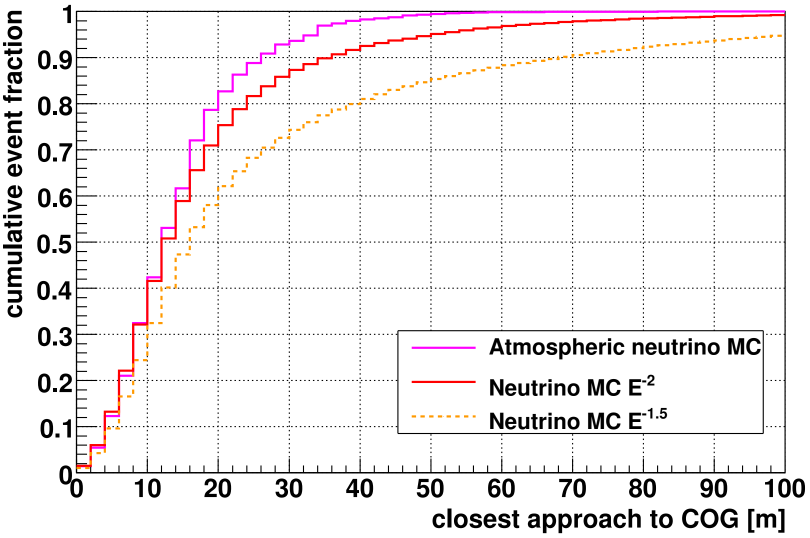

Figure 8.5.: The distance of closest approach between the reconstructed track and the centre of gravity (COG) of all hit DOMs, displayed as cumulative fraction for different simulated neutrino spectra.

detector volume but by those really passing in between the strings. For $d = 20$ m and a variation of ±10% for the effective propagation length around a mean of $\lambda_p = 30$ m, one obtains a relative shift in the light yield of less than 10% in both directions.

A simple way to estimate the effect of this uncertainty on Monte Carlo neutrino fluxes is using a dedicated simulation with modified DOM efficiencies. Two such Monte Carlo datasets of muon neutrinos with DOM efficiencies changed by ±10% were produced, covering the assumed scale of variations in light yield, i.e. detected photons. After applying the same processing and cutting scheme as in the actual analysis, the simulation with 90% nominal DOM efficiency showed an average deviation of $-4.4\%$ in the number of expected neutrinos from an $E^{-2}$ flux. The upward change was slightly larger, with the neutrino count increased by 6.3% ($E^{-2}$ ) for the Monte Carlo data with 110% DOM efficiency. Weighting the events to an $E^{-1.5}$ spectrum led to deviations of only $-1.0\%$ and $+4.1\%$, probably due to the reduced impact of these changes on selection criteria for bright events.

Due to ice transparency differences, the relative light yield of a DOM varies by more than 10% in dependence of its depth. These variations are included in the simulation, but some disagreement is observed when studying depth-dependent event rates of data and background Corsika Monte Carlo. In another muon neutrino analysis [A$^+$09e], these deviations were used directly in the simulation to define a depth-dependent rescaling of relative DOM efficiencies that covers the observed differences. These changes led to a decrease of the observable neutrino flux strength by 16% for an $E^{-2}$ spectrum. In lack of a new simulation for repeating this calculation, the same value is used here, relying on the observation that differences in the event selection have little impact on such light propagation effects. Possible small effects of deviations from the nominal acceptance of the photomultipliers themselves are covered by the uncertainties described above.

### Biases in simulation and reconstruction

For the reconstruction of simulated events, exactly the same algorithms as applied to measured data are used. Nevertheless, inaccuracies in the simulation might systematically bias the results such that cuts on the various parameters do not behave exactly as expected for actual data. Examples for such critical steps in the Monte Carlo approach are the extraction of pulses from a waveform, see section 5.1.1, or error estimates of likelihood reconstructions, see section 5.2.

To test the validity of generation and reconstruction of Monte Carlo neutrino events, it is possible to make a direct comparison with the up-going half of the event sample, which consists predominantly of atmospheric neutrinos. By attributing any deviations to systematic biases in the reconstruction of simulated events, one can derive a conservative estimate of their effect on the signal prediction. This is a simple but direct form of neutrino simulation calibration, because the same simulated events, differently weighted, are used to describe both measured atmospheric neutrinos and expected signal fluxes. For down-going events, the lack of atmospheric neutrinos precludes to perform a separate check along the same lines. There is enough reason, though, to assume that the same biases apply also to these events, for example in view of the uniform quality of the direction reconstruction with declination.

Since purity of the up-going sample was not a major concern during cut optimisation, the final level sample is still contaminated by misreconstructed atmospheric muon events. To remove this residual background before the comparison with a simulated atmospheric neutrino spectrum, slightly stronger cuts were applied. Specifically, these were the exclusion of the region at the horizon below declination $+10°$ (zenith angle $\theta = 100°$) and a harder cut on the reduced log-likelihood of rlogl $\leq$7.3. The resulting event distribution is shown in Fig. 8.6.

After applying these additional cuts, the distributions of simulated atmospheric neutrinos and data were compared for each of the variables used in the *level 5* event selection. For the number of hit DOMs (NChannel), pulses per DOM (NHits/NCh) and the error ellipse size from the MPE likelihood (Paraboloid-Sigma), these comparisons were done separately for the regions above and below the dust layer (COG-Z $>$ 0m and $< -200$m), to account for the known differences in simulation of light propagation. In each case, a Kolmogorov-Smirnov test was applied to the two histograms, yielding the probability for both having the same underlying distribution (with a maximum value of 1.0). Simple scaling factors, and in two cases also a shift, of the variable were found to improve the agreement between data and Monte Carlo distributions. This scaling cannot be considered

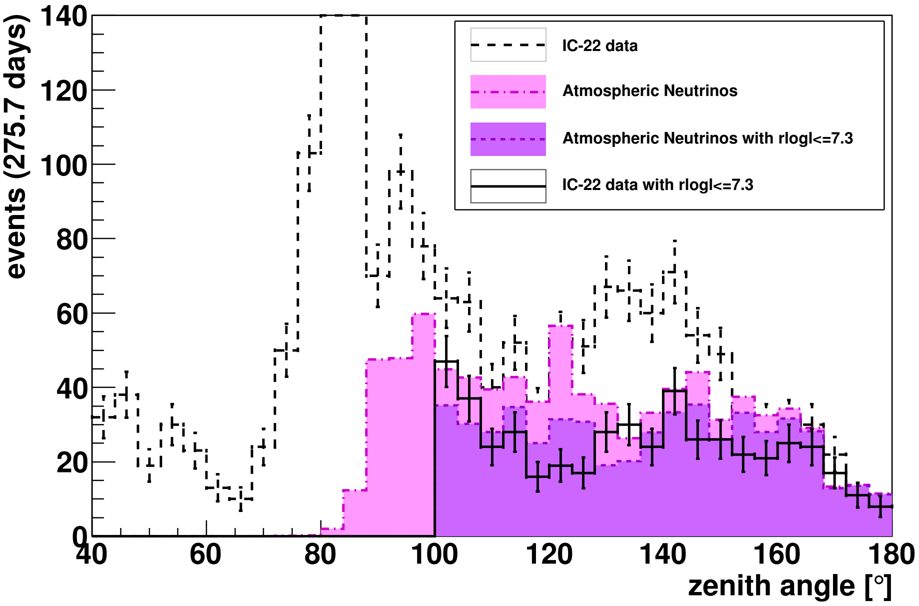

Figure 8.6.: Zenith angle event distributions for data and atmospheric neutrinos. The final level sample (dashed) is compared to an upward-only selection with additional quality cuts for reduced muon background contamination.

as an attempt to correct the atmospheric background simulation, but rather as a way of quantifying the deviations. This was done by applying the level 5 cuts based on the rescaled variables and determining the difference in Monte Carlo neutrino numbers.

Figure 8.7 presents an example for this method, using the number of channels. In the histograms for the upper detector region, the agreement cannot be improved, but in the region of deep COG-Z a scaling is applied: $v_s = 1.17 \cdot v$, $v$ representing the value of the channel count. The Kolmogorov-Smirnov probability for the Monte Carlo data to be distributed according to the measured atmospheric neutrinos was 1.0 after scaling compared to 0.04 before it.

The largest deviations were observed for the number of hits per channel. These are probably related to inaccuracies in the simulation of waveforms and in fitting individual photon pulses (the hits). In this case, the corrected values were derived from two scalings, one based on the ratio of hits over channels (*NHits/NCh scaled as ratio*) and one obtained from treating the distributions of hits and channels separately (*NHits/NCh scaled separately*).

All scaling factors are listed in Table 8.2. To estimate the change in signal rates due to the assumed simulation bias, the *level 5* cuts were applied to the rescaled variables. The resulting number of signal events using each modified variable was compared to the original value obtained without scaling. Table 8.2 shows these

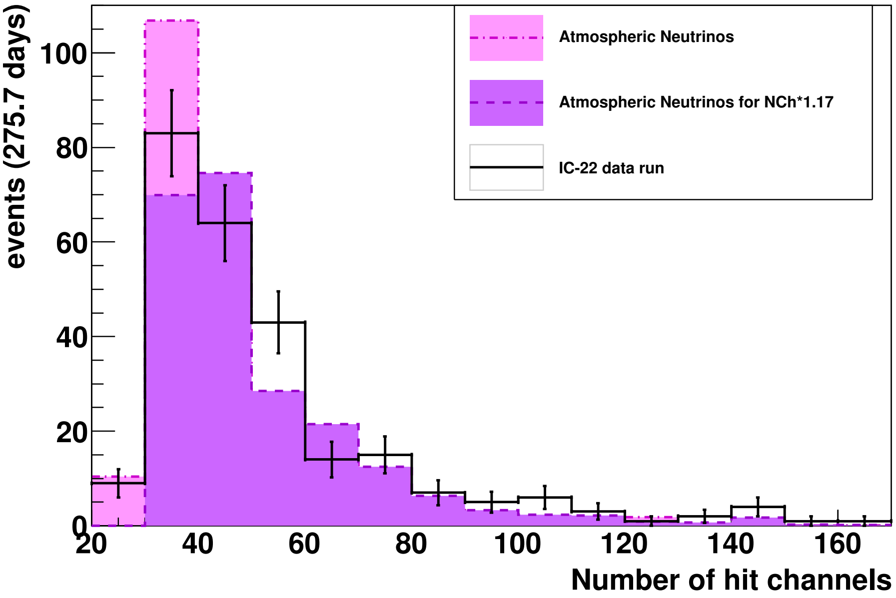

Figure 8.7.: Distribution of the number of hit DOMs (NChannel) for data and simulated atmospheric neutrinos, after application of the cuts for increased neutrino purity (see 8.6). The rescaling of NChannel in the simulated sample leads to better agreement.

deviations as percentages for both $E^{-2}$ and $E^{-1.5}$ neutrino spectra. The values are given separately for up-going ($\delta < 0°$) and down-going ($\delta > 0°$) tracks, to highlight different impacts.

The relatively small deviations related to the reduced log-likelihood cuts give confidence that the the additional quality cuts on this parameter have not significantly changed the bias effects. Since the variations are not independent from each other but induced by general reconstruction biases, only the largest uncertainty value from all variables and both hemispheres is taken as the final estimate for the magnitude of this effect. For an $E^{-2}$ spectrum, this amounts to a relative uncertainty of $-3.6\%$ / $+8.7\%$ on the muon neutrino flux. The results for the $E^{-1.5}$ spectrum, $-3.4\%$ / $+5.9\%$ are smaller.

### Theoretical uncertainties

Neutrino interactions implemented in *Neutrino Generator* are based on the CTEQ structure functions, for which [P$^+$02] provides a way to estimate inherent uncertainties. A calculation for the northern sky point source analysis [A$^+$09c] led to an error margin of 2% for the cross section and therefore also the measured neutrino flux. While the density of the ice is well known, that of the bedrock below the antarctic glacier is less certain. This aspect is discussed in [Ack06], and the

| cut variable | scaling | $E^{-2}$ | | $E^{-1.5}$ | |
|---|---|---|---|---|---|
| | | $\delta < 0°$ | $\delta > 0°$ | $\delta < 0°$ | $\delta > 0°$ |
| NCh | 1.0 for $z > 0$<br>1.17, $z < -200$ | $-2.3\%$ | $+2.7\%$ | $-3.4\%$ | $+1.1\%$ |
| NHits/NCh scaled as ratio | 1.0, $z > 0$<br>1.4 (shift $-1.0$), $z < -200$ | $+8.7\%$ | $0.0\%$ | $+5.9\%$ | $0.0\%$ |
| NHits/NCh scaled separately | 1.0, $z > 0$<br>0.95, $z < -200$ | $-3.6\%$ | $0.0\%$ | $-2.5\%$ | $0.0\%$ |
| Paraboloid $\sigma$ | 0.97, $z > 0$<br>1.55 (shift -0.25), $z < -200$ | $-1.6\%$ | $-2.7\%$ | $-1.8\%$ | $-2.2\%$ |
| red. log-llh. | 1.004 | $0.0\%$ | $-1.0\%$ | $-0.4\%$ | $-1.0\%$ |
| Bayesian ratio | 0.96 | $-2.6\%$ | $-1.5\%$ | $-1.9\%$ | $-2.4\%$ |
| NDir | 0.9 | $+0.3\%$ | $0.0\%$ | $0.0\%$ | $0.0\%$ |

Table 8.2.: Result from the comparison of up-going events with atmospheric neutrino simulation. The scaling factors and shifts for the final level cut parameters are shown, separately for centre of gravity below and above the dust layer where necessary. The impact of these uncertainties on the event selection is shown as a change of neutrino signal expectation.

estimate of its impact on simulated neutrino fluxes in IceCube data for 22 strings (see [A$^+$09c]) is an uncertainty of 2%. For the muon propagation, based on the energy loss discussed in section 3.1.3, the authors of the programme *MMC* give an uncertainty of 3% on the survival rates in [CR04].

**Total uncertainties**

The individual uncertainty estimates are listed in Table 8.3. They express the relative change in the observable muon neutrino flux, and the inverse values correspond to the shift in the limits. The $E^{-1.5}$ spectrum is not considered separately, since in all cases the uncertainties were equal or smaller compared to those for $E^{-2}$ . Also, since an unbroken $E^{-1.5}$ power law cannot be expected for a very large energy range, it is appropriate to use a more conservative estimate. The quadratic sum of all these systematic uncertainties on the signal flux amounts to $-18\%$ / $+13\%$ relative to the simulated neutrino yield.

## 8.4.3. Uncertainties on flux limits

The conversion from a given number of observed events in a bin to a neutrino flux limit is achieved by constructing confidence belts to determine the upper limit on the number of signal events. A comparison to the expected value from

| uncertainty | neutrino flux deviation |
|---|---|
| general simulation parameters | ±5% |
| light propagation length | $-4\% / +6\%$ |
| light propagation in layers | $-16\%$ |
| reconstruction bias | $-4\% / +9\%$ |
| muon propagation | ±3% |
| neutrino cross section | ±2% |
| bedrock density | ±3% |
| **total** | **−18% / +13%** |

Table 8.3.: Overview of the systematic uncertainties on muon neutrino fluxes in this IceCube 22-strings point source analysis. The square root of the quadratic sum is the total flux uncertainty.

simulation then serves to scale a reference flux, see page 33. This approach relies on the Poisson probability $P(n|s+b)$ from equation (3.15). Single bin values can be replaced by an integral over a range of probabilities for different signal ($s$) and background ($b$) numbers, weighted with a distribution that reflects the uncertainties on $s$ and $b$. A detailed description is provided in [Ack06].

For the number of background events, the statistical uncertainty was derived individually in each declination band from the total number of events. This was implemented in the probability via a Gaussian distribution around the true value. The systematic uncertainty on the signal, as presented in the previous section, required a choice of shape for the distribution of deviations. Following the prescription in [Ack06], a Gaussian distribution was used, since the true shape is unknown. To accommodate the asymmetric relative errors $r_{\text{sys}}^{+}$ and $r_{\text{sys}}^{-}$ in this scheme, the expected number of signal neutrinos from Monte Carlo simulation $s_{\text{MC}}$ was rescaled to be centred in this uncertainty interval:

$$s_{exp} = s_{\text{MC}} \frac{1}{2} \left( (1 + r_{\text{sys}}^{+}) + (1 - r_{\text{sys}}^{-}) \right) . \tag{8.3}$$

Correspondingly, the symmetric relative uncertainty,

$$r_s = \frac{\sigma_s}{s_{\text{exp}}} = \frac{1}{s_{\text{exp}}} \frac{r_{\text{sys}}^{+} + r_{\text{sys}}^{-}}{2} s_{\text{MC}} = \frac{r_{\text{sys}}^{+} + r_{\text{sys}}^{-}}{2 + r_{\text{sys}}^{+} - r_{\text{sys}}^{-}} \approx 16\% , \tag{8.4}$$

determined the width of the Gaussian representing the systematic uncertainties of each binned observation result. The value of 16% was obtained by conservatively rounding the exact value.

An integration over these symmetric intervals for statistical and systematic uncertainties was performed for the product of Gaussian weights and the Poisson probability $P(n|s+b)$. The resulting distribution function of signal and back-

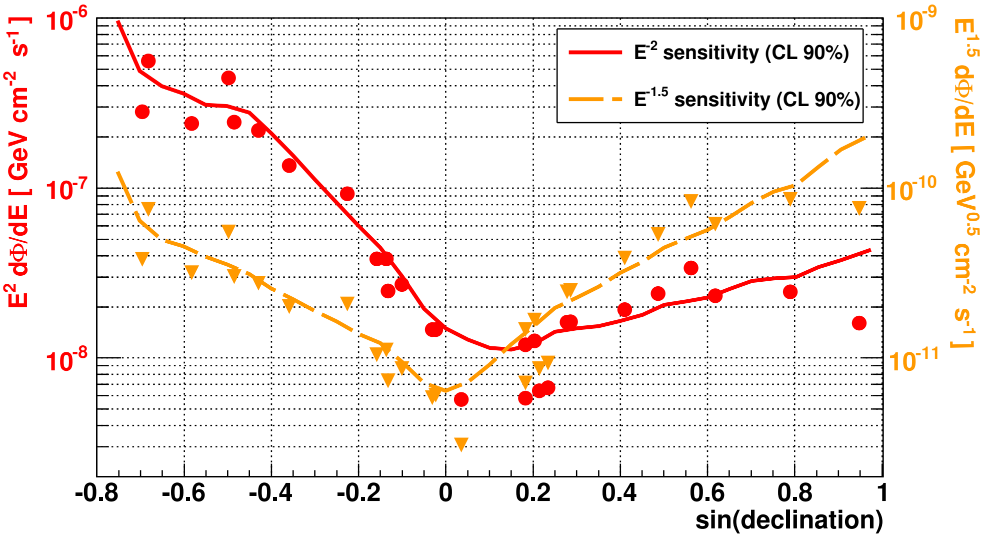

Figure 8.8.: Sensitivities, equivalent to right ascension averaged flux limits, together with individual source candidate limits for two signal spectrum hypotheses, $E^{-2}$ (solid red, circles, left axis) and $E^{-1.5}$ (dashed orange, triangles, right axis).

ground event counts is the input for equation (3.15) which is used to derive upper limits according to [FC98]. This direct inclusion of uncertainties in the upper limits was described in [CBHdlH03] and implemented in the programme POLE that was used in this work for the calculation.

The translation of neutrino event limits into muon neutrino flux limits was done through comparison to a spectrum-dependent Monte Carlo reference flux as in equation (3.17) with $N_{\Phi_0} = s_{exp}$. The scaling quotient $\mu_{90}/s_{exp}$ is referred to as the model rejection factor (MRF). If its value is smaller than one, the model predicting a flux $\Phi_0$ is excluded.

## 8.5. Neutrino flux limits

The individual neutrino flux limit for each bin depends on the exact number of observed and expected events. Variations due to background fluctuations are visible in the significance distribution in Fig. 8.1. The overall level of sensitivity, shown in Fig. 7.3, varies on a larger scale, mostly as a result of the declination dependence of cuts and absorption characteristics. This sensitivity as a function of declination was adjusted by including systematic uncertainties as discussed above. Figure 8.8 presents the final mean upper limits for $E^{-2}$ and $E^{-1.5}$ signal spectra. The limits for the 28 source candidates are included as points and illustrate fluctuations from the mean due to actual measured event numbers. Excluded muon neutrino fluxes

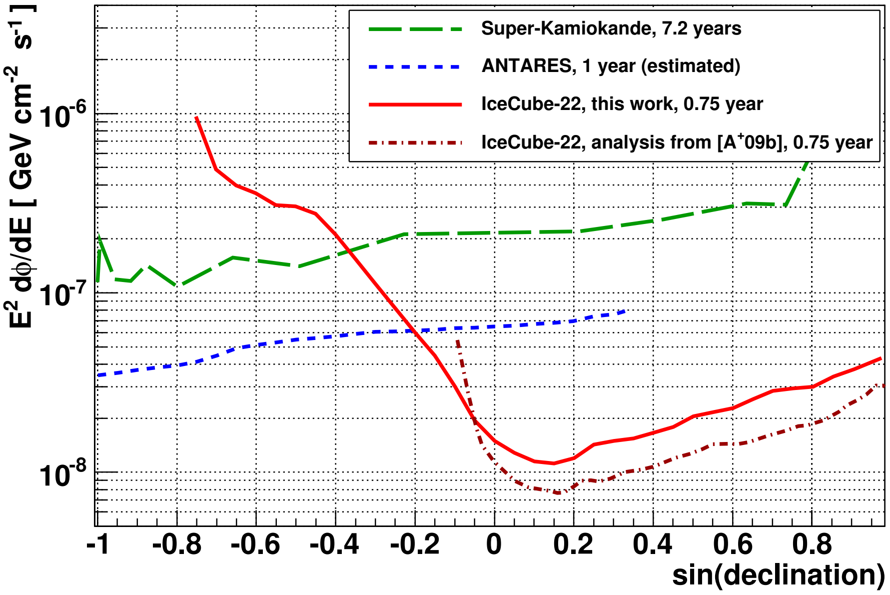

Figure 8.9.: Sensitivities for an $E^{-2}$ neutrino signal spectrum hypothesis in dependence of declination. The point source search from this work is compared to the IceCube analysis in [A+09c], the one published by the Super-Kamiokande collaboration in [Thr09] and the Antares study [AS07].

are listed in Table 8.4.

The $E^{-1.5}$ sensitivity can be considered a benchmark for spectral indices harder than $-2.0$, illustrating that the sensitivity to such fluxes is as good for sources above the horizon as for those at mirrored angles below the horizon, due to the importance of higher energy events.

A comparison of the $E^{-2}$ sensitivity to those of other point source searches is presented in Fig. 8.9. The likelihood analysis of IC-22 data in [A+09c] provides slightly better average values for declinations in the northern sky, but is limited to that hemisphere. For the comparison to the average limit from the Super-Kamiokande point source search [Thr09] and the estimate of the Antares sensitivity with one year of data [AS07], one has to consider the difference in energy coverage. These experiments scan the southern sky[1] with up-going events that cannot exceed PeV energies due to absorption and are also more sensitive to low TeV energies. Consequently, the Super-Kamiokande and Antares limits on neutrino fluxes at negative declinations are complementary to the results of the analysis presented here, with its higher thresholds above hundreds of TeV, see

---

[1] The location of the detectors in Japan and in the Mediterranean sea actually permits a partial coverage of both the southern as well as the northern sky with up-going events, as illustrated in the plot.

| source name | dec. [°] | $\mu_{90}$ | $\Phi_{-2}$ $\times 10^{9}$ | $\Delta E_{-2}$ [GeV] | $\Phi_{-1.5}$ $\times 10^{12}$ | $\Delta E_{-1.5}$ [GeV] |
|---|---|---|---|---|---|---|
| PKS 0537-441 | $-44.1$ | 1.8 | 281.3 | $10^{6.5} - 10^{8.8}$ | 38.1 | $10^{6.8} - 10^{9.7}$ |
| PKS 1622-297 | $-29.9$ | 4.0 | 442.8 | $10^{6.4} - 10^{8.8}$ | 55.2 | $10^{6.8} - 10^{9.7}$ |
| PKS 1622-253 | $-25.5$ | 2.4 | 218.3 | $10^{6.4} - 10^{8.8}$ | 27.6 | $10^{6.8} - 10^{9.7}$ |
| PKS 1830-210 | $-21.1$ | 2.3 | 135.5 | $10^{6.1} - 10^{8.8}$ | 20.0 | $10^{6.7} - 10^{9.7}$ |
| PKS 1730-130 | $-13.1$ | 4.6 | 92.4 | $10^{5.6} - 10^{8.4}$ | 20.8 | $10^{6.2} - 10^{9.7}$ |
| PKS 1510-089 | $-9.1$ | 3.4 | 38.3 | $10^{5.1} - 10^{8.3}$ | 10.4 | $10^{6.0} - 10^{9.7}$ |
| PKS 1406-076 | $-7.9$ | 4.2 | 38.2 | $10^{4.9} - 10^{8.2}$ | 11.2 | $10^{5.9} - 10^{9.7}$ |
| QSO B2022-077 | $-7.6$ | 2.8 | 24.8 | $10^{4.9} - 10^{8.2}$ | 7.3 | $10^{5.9} - 10^{9.7}$ |
| 3C279 | $-5.8$ | 4.0 | 27.1 | $10^{4.8} - 10^{8.2}$ | 8.7 | $10^{5.7} - 10^{9.7}$ |
| PKS 0336-01 | $-1.8$ | 3.0 | 14.7 | $10^{4.4} - 10^{8.0}$ | 5.9 | $10^{5.5} - 10^{9.7}$ |
| PKS 0420-01 | $-1.3$ | 3.1 | 14.7 | $10^{4.4} - 10^{8.0}$ | 6.0 | $10^{5.5} - 10^{9.7}$ |
| 3C 273 | 2.0 | 1.5 | 5.7 | $10^{4.4} - 10^{7.6}$ | 3.1 | $10^{5.3} - 10^{9.6}$ |
| PKS 1502+106 | 10.5 | 1.6 | 5.8 | $10^{4.3} - 10^{6.8}$ | 7.1 | $10^{4.8} - 10^{7.8}$ |
| 4C +10.45 | 10.5 | 3.3 | 11.9 | $10^{4.3} - 10^{6.8}$ | 14.7 | $10^{4.8} - 10^{7.8}$ |
| 4C +11.69 | 11.7 | 3.4 | 12.6 | $10^{4.2} - 10^{6.8}$ | 16.7 | $10^{4.8} - 10^{7.7}$ |
| PKS 0528+134 | 13.5 | 1.6 | 6.7 | $10^{4.2} - 10^{6.7}$ | 9.3 | $10^{4.8} - 10^{7.6}$ |
| 3C 454.3 | 16.1 | 3.5 | 16.2 | $10^{4.1} - 10^{6.6}$ | 24.5 | $10^{4.7} - 10^{7.4}$ |
| PKS 0235+164 | 16.6 | 3.5 | 16.3 | $10^{4.2} - 10^{6.6}$ | 25.0 | $10^{4.7} - 10^{7.4}$ |
| QSO B0827+2421 | 24.2 | 3.5 | 19.3 | $10^{4.0} - 10^{6.3}$ | 38.7 | $10^{4.5} - 10^{7.0}$ |
| QSO B0430+2859 | 29.1 | 3.7 | 24.0 | $10^{4.0} - 10^{6.2}$ | 53.2 | $10^{4.4} - 10^{6.7}$ |
| QSO B1611+3420 | 34.2 | 5.0 | 33.9 | $10^{3.8} - 10^{6.1}$ | 83.1 | $10^{4.4} - 10^{6.8}$ |
| 4C +38.41 | 38.1 | 3.3 | 23.3 | $10^{3.9} - 10^{6.0}$ | 61.2 | $10^{4.3} - 10^{6.7}$ |
| 4C +51.37 | 52.2 | 2.9 | 24.5 | $10^{3.6} - 10^{5.7}$ | 85.5 | $10^{4.0} - 10^{6.3}$ |
| 8C 0716+714 | 71.3 | 1.4 | 16.0 | $10^{3.3} - 10^{5.5}$ | 75.9 | $10^{3.9} - 10^{5.9}$ |
| PKS 1454-354 | $-35.6$ | 2.0 | 238.9 | $10^{6.0} - 10^{8.8}$ | 31.8 | $10^{6.8} - 10^{9.7}$ |
| PKS 1502+106 | 10.5 | 1.6 | 5.8 | $10^{4.3} - 10^{6.8}$ | 7.1 | $10^{4.8} - 10^{7.8}$ |
| M87 | 12.4 | 1.7 | 6.4 | $10^{4.2} - 10^{6.8}$ | 8.6 | $10^{4.8} - 10^{7.6}$ |
| Centaurus A | $-43.0$ | 3.7 | 556.7 | $10^{6.5} - 10^{8.8}$ | 74.7 | $10^{6.8} - 10^{9.6}$ |
| Sgr A* | $-29.0$ | 2.3 | 244.3 | $10^{6.4} - 10^{8.8}$ | 30.2 | $10^{6.8} - 10^{9.7}$ |

Table 8.4.: Upper limits on muon neutrino event numbers ($\mu_{90}$) and fluxes for the 28 objects of the pre-defined source candidate list. The limits for the two signal spectrum hypotheses, $\gamma = -2$ and $\gamma = -1.5$, are given as normalisation constants for the differential flux $d\Phi/dE \leq \Phi_\gamma (E/\mathrm{GeV})^\gamma\,\mathrm{GeV}^{-1}\mathrm{cm}^{-2}\mathrm{s}^{-1}$. Systematic uncertainties are included in all limits. The energy ranges $\Delta E_\gamma$ describe the intervals containing 90% of simulated signal neutrinos, excluding the highest and lowest 5% of events. See also Table 7.1 for more information on the objects.

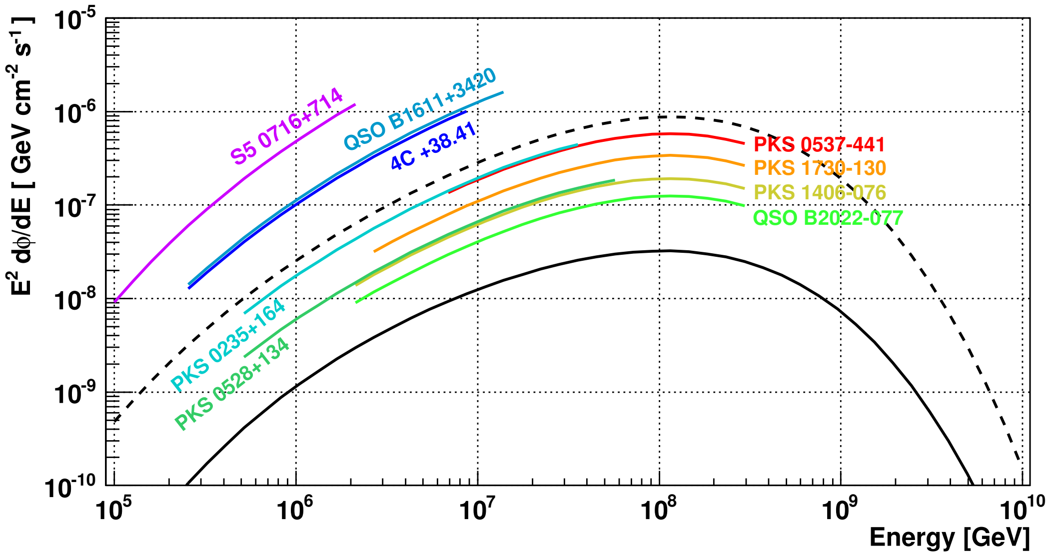

Figure 8.10.: Muon neutrino limits for nine selected blazars. Differences in energy coverage are due to varying declinations, indicated by the last digits of the names. The spectral shape reflects the prediction for emission with an opening angle of 1° (black dashed) or 5° (black solid) from [NSAK02].

Table 8.4.

### Blazar models

The model from [NSAK02] for proton acceleration in AGN cores mentioned in section 2.2.2 was used in [NS02] as a basis for selecting blazars that are promising neutrino source candidates. The argument is based on jet orientation and ultraviolet photons as seed particles for pion production. Since the authors also use GeV gamma-ray emissions of blazars detected by EGRET as a starting point to apply their selection criteria, the final list has a large overlap with the source candidates chosen in section 7.2. Nine out of fourteen objects preferred in this model were tested in the analysis presented here. Figure 8.10 shows the muon neutrino limits for these blazars based on the generic spectrum from [NS02]. Two different opening angles for neutrino emissions are discussed by the authors, the larger one corresponding to the level of collimation observed for gamma rays. For many of the tested sources, the optimistic neutrino scenario with a 1° opening is ruled out by the observed flux limits.

Apart from the restrictions placed on this model, Fig. 8.10 also illustrates the different energy ranges of sensitivity for sources below the horizon, listed on the left, and the four objects above the horizon on the right. The limits are shown for the energy intervals containing 90% of the signal expectation, which only for the

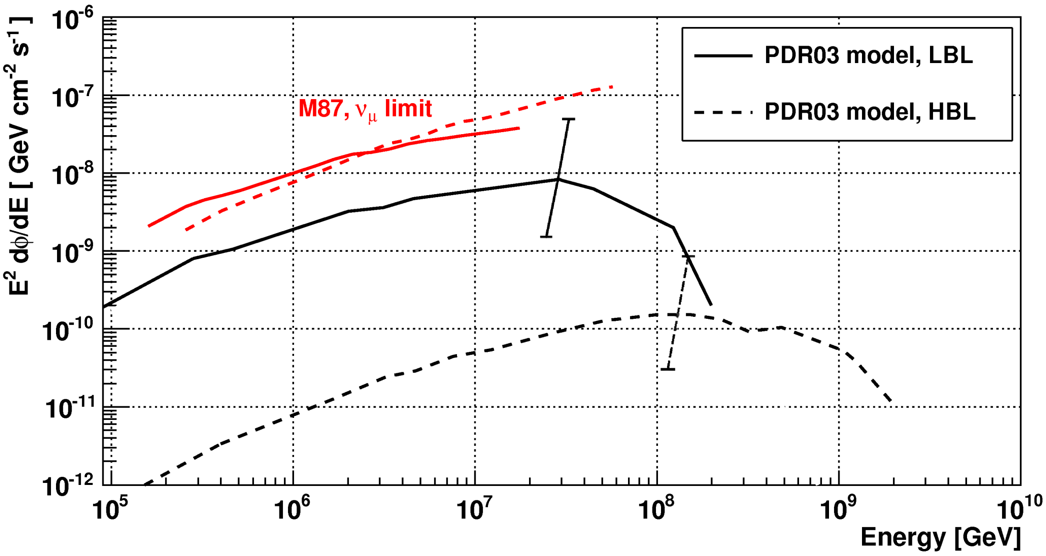

Figure 8.11.: Muon neutrino limits for the radio galaxy M87. The reference model fluxes are derived in [PDR03] under the assumption of the source being a misaligned blazar with LBL-like (black solid) or HBL-like (black dashed) characteristics. The error bars represent theoretical uncertainties.

four blazars at negative declinations covers the full PeV range.

### M87

The radio galaxy M87 is not classified as a blazar due to the orientation of its jet axis, which does not point directly at Earth. Nevertheless, it is proposed in [PDR03] that this object might feature the acceleration characteristics of a BL Lac object based on the model from [MPE$^+$03]. Two dedicated muon neutrino emission spectra are presented and reproduced in Fig. 8.11. The lower dashed curve represents a model based on fits of photon data to a synchrotron spectrum following an average HBL-like behaviour, while the upper one results from an LBL-like modelling. For the latter, the limit obtained in this analysis allows a flux constraint that falls within the upper error margin indicated by the authors for their model. The absorption of neutrinos during passage through Earth at energies exceeding tens of PeV at the object's position of dec. +12.4° does not permit to fully probe the favoured energy range for neutrino emissions.

### Centaurus A

As discussed in section 7.2, the radio galaxy Centaurus A could be the source of charged cosmic rays in the context of results from the Pierre Auger Obser-

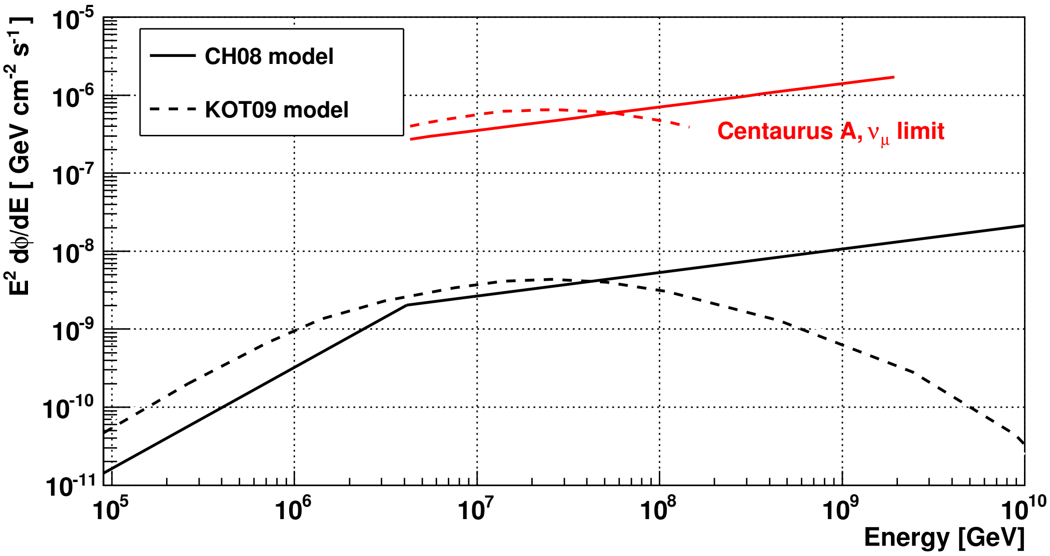

Figure 8.12.: Muon neutrino limits for the radio galaxy Centaurus A. The two spectral shapes represent the emission models from [CH08] and [KOT09].

vatory (PAO) [A$^+$07a, A$^+$08d]. An emission model published in [CH08] uses this input to derive a neutrino spectrum prediction shown in Fig. 8.12. It was reduced to the muon neutrino component assuming full flavour mixing as in section 3.1.1. The flux limit for this spectral shape derived from the IC-22 search results is approximately two orders of magnitude higher and thus cannot constrain this prediction.

Additionally, Fig. 8.12 includes a neutrino flux prediction presented in [KOT09]. Out of the range of model parametrisation discussed there, it is the case with the highest neutrino rate not excluded by the recent TeV gamma-ray measurements with Hess for Centaurus A [A$^+$09k]. The sensitivity of the IC-22 search is not enough to probe the predicted flux level. Nevertheless, these are the first neutrino limits in the PeV to EeV energy range for Centaurus A.

### Galactic centre

For the object Sgr A$^*$, considered to be a super-massive black hole at the centre of our galaxy, the lower energy threshold in this analysis lies above 1 PeV. The neutrino flux upper limit, shown in Table 8.4, is the first for this source that covers this energy range, made possible by the observation of down-going events from the southern sky.

# Chapter 9.

# Correlations between neutrinos and charged cosmic rays

In addition to the search for individual neutrino point sources, presented in the previous chapters, the IceCube event sample defined in this work can also be used for all-sky studies of correlations with other cosmic ray observations. In the following, such a multi-messenger analysis is presented, using the directions of charged particle events at ultra-high energies. These data stem from air shower experiments, introduced in the first section. The correlation search method and the simulations necessary for its optimisation with respect to the discovery potential are discussed in the second part. The chapter concludes with the results from applying this analysis to the IceCube 22-strings event sample.

## 9.1. Charged cosmic ray observations

### 9.1.1. Motivation for a correlation study

In section 3.2.3 the concept of multi-messenger searches was introduced. The significance of an excess of potential cosmic neutrinos can be enhanced by finding directional correlations between the events and other observations of particles assumed to originate in the same sources. A natural choice for these complementary messengers are protons or heavier charged cosmic rays, because they are expected to generate a secondary neutrino flux in or near their sources, see section 2.1.3. Due to deflection in astrophysical magnetic fields, only charged particles with ultra-high energies larger than several EeV can be traced back to their source regions.

In the approach presented here, publicly available data on *ultra-high energy cosmic rays* (UHECR) are used as a set of reference directions. Around these, up to a pre-defined distance, the number of neutrino candidates from the IceCube event sample is determined. The significance of this event count can be calculated by comparing its value to expectations from randomised maps of the IceCube data.

## 9.1.2. Air shower experiments

Data from two extensive air shower detectors currently provide the majority of information on UHECR: The High Resolution Fly's Eye (HiRes) experiment, decomissioned in 2006, and the currently operating southern Pierre Auger Observatory (PAO). A brief overview of their techniques and results relevant for a correlation study is given in the following. For this search, only fully analysed and published air shower data were used.

### The HiRes experiment

The HiRes experiment was operated for nine years between 1997 and 2004 in the desert of Utah, USA. In moonless nights, extensive air showers within a radius of 35 km were detected and reconstructed by measuring the fluorescence emission along their paths through the atmosphere. Since 1999 two detectors, located at a relative distance of 12.6 km from each other, were operated together, one containing 21 and the other 42 telescopes. Each telescope had a spherical mirror area of 5.1 $m^2$ and directed light onto a camera consisting of 256 photo-multipliers. Coincident stereo operation of both sites resulted in a total of 3460 hours livetime [$A^+09g$]. For a full description of the experiment see [$AZ^+99$, BKMS02].

### The Pierre Auger Observatory

The Pierre Auger Observatory [$A^+04a$] was designed as an experiment with two sites in different hemispheres where air showers are measured with a hybrid technique of fluorescence telescopes and particle detectors. While the northern part is still in the planning phase, the PAO South array near the city of Malargüe, Argentina, is running in a stable data taking mode since 2004. The construction of this array is now completed. 1600 surface detectors are distributed over an area of 3000 $km^2$ with a triangular grid spacing of 1.5 km. These components are tanks, each containing 12 tons of purified water in which three photo-multipliers detect Cherenkov light from through-going shower particles. Geometric and calorimetric information from an event allows the reconstruction of energy and direction of the primary particle initiating a shower in the upper atmosphere.

Additionally, fluorescence detectors, similar to those of HiRes, are located at 4 sites at the edges of the array, each containing 6 independent telescopes with segmented primary mirrors. A single mirror has an area of $\sim$13 $m^2$. Under favourable weather conditions and sufficiently low moonlight at night, the measured fluorescence light is used to reconstruct showers, giving the possibility to verify and complement the surface detector data [$A^+09j$].

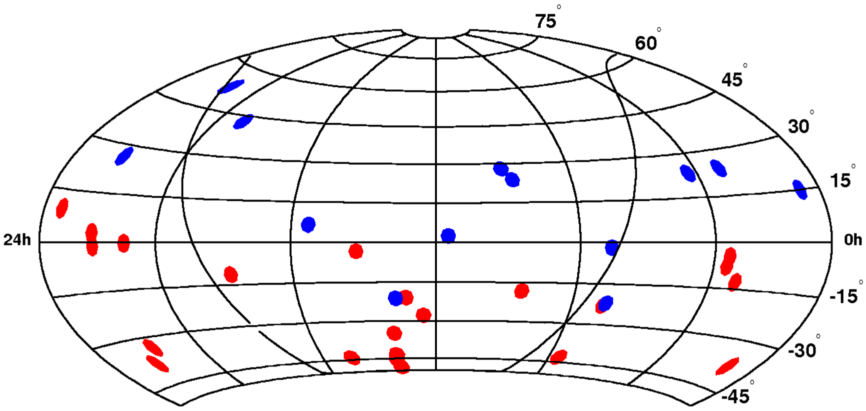

Figure 9.1.: Arrival directions of UHECRs in equatorial coordinates for the IC-22 field of view: 22 events from PAO (red) and 13 events from HiRes (blue).

### UHECR data samples

The published PAO data on arrival directions from UHECRs comprise 27 events above an energy of $6 \times 10^{19}$ eV, collected between January 2004 and August 2007 [A+08d]. The precise energy threshold of 56 EeV was optimised in a search for correlations with nearby AGN from an astronomical catalogue [VCV06], together with two other search parameters as described in [A+07a]. In that analysis, the hypothesis of an isotropic distribution of UHECRs was rejected with a probability of 99% and a correlation with the AGN sample was claimed. Recently, the results were updated in [H+09] with 31 additional events detected until March 2009. The degree of correlation in the full sample has decreased, because the new data does not show a significant excess of UHECRs close to AGN from the chosen catalogue.

The possible correlation of the PAO data with AGN has no impact on the neutrino analysis presented in this work. Only the reported coordinates of UHECR arrival directions themselves are considered here. Since the 31 events from [H+09] have not been made publicly available, only the original 27 directions are used. 22 of these have declinations above $-50°$ and thus lie inside the field of view of the IceCube sample defined in chapter 6, see Fig. 9.1.

Following the PAO reports on correlations with AGN, the HiRes collaboration applied the same energy threshold as in the PAO study to all their events collected in stereo mode. They found 13 events and published the arrival directions in [A+08c]. HiRes could not confirm a correlation with the AGN catalogue. Furthermore, a second test with a different event selection optimisation did not show evidence for anisotropy. Due to the location of the experiment, this search covered mainly the northern celestial hemisphere, in contrast to the PAO observations of the southern sky.

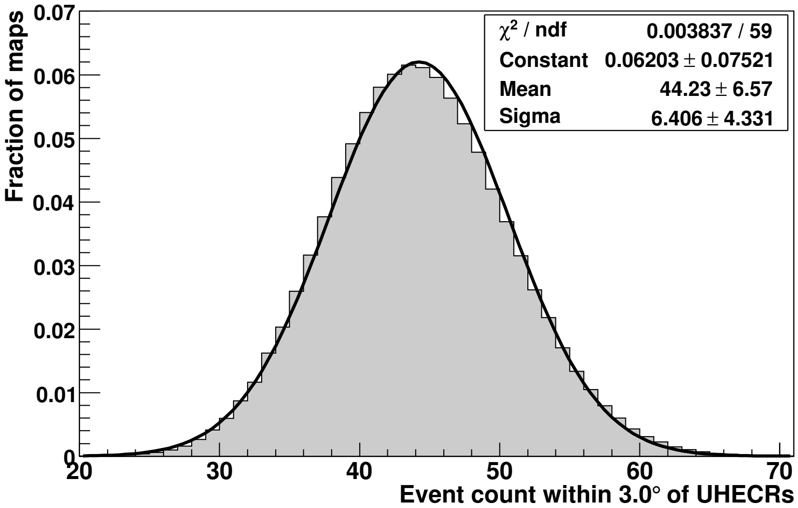

Figure 9.2.: Expected distribution of total event counts in bins of 3.0° radius around PAO & HiRes UHECR directions for background-only simulations. The histogram was obtained from 1 million randomised maps and is shown with a Gaussian fit.

All 13 arrival directions of UHECRs above $6 \times 10^{19}$ eV reported by HiRes lie inside the field of view of the IceCube 22-strings event selection, see Fig. 9.1. They can be tested for correlations together with the 22 PAO events with the method described in the following.

## 9.2. Directional correlations

### 9.2.1. Correlation method

A possible correlation between UHECR directions and the IceCube data can be tested by counting the neutrino candidates in circular bins of a pre-defined radius centred on the arrival directions of the charged cosmic rays. In [Pet09], an application of such an approach to generic neutrino and UHECR data samples is discussed. To calculate the significance of the observed sum of events over all bins, it has to be compared to the expectation from pure background samples. Figure 9.2 shows a histogram of event counts for $10^6$ sky maps, generated by randomising the right ascension of each each of the 1885 events in the IceCube 22-strings sample. The declination distribution was kept unchanged, see also page 92. The bin locations refer to the combined PAO and HiRes UHECR samples, comprising 35 directions. The bin radius of 3.0° is a result of the optimisation discussed in the following section.

The event count over all bins is performed by testing for each IceCube event if the minimum angular distance to any UHECR direction is smaller than the fixed bin radius. This guarantees that events in overlapping bins are not counted more than once. The distribution of counting results in background samples is well approximated by a Gaussian function around a mean of 44.2 events with a width of 6.4 . By integrating the background distribution over all event numbers larger than the one which is eventually observed, one obtains the probability for the measured outcome to appear in a background-only scenario.

The optimisation of the search parameters, discussed in the following, was based on neutrino simulations as well as data with scrambled direction information. This was done to avoid observational biases in accordance with the IceCube blindness policy. The application of the fixed analysis prescription to unscrambled event coordinates leads to the final probability value. No trial factors have to be considered.

## 9.2.2. Signal simulation

### Magnetic deflection

The above method for a search for correlations between two sets of event directions is independent of model assumptions on the signal. However, a neutrino signal simulation is necessary to assess the discovery potential and optimise the analysis for realistic expectations.

The UHECR directions are used as references for simulated neutrino sources. Contrary to the neutral neutrinos, charged protons or nuclei are affected by magnetic fields that have to be taken into account even for particles energies above $6 \times 10^{19}$ eV. There are few established facts about astrophysical magnetic fields and predictions vary concerning their strengths and orientations. Discussions on their impact on the propagation of proton UHECRs above tens of EeV are presented for example in the following publications:

- The PAO collaboration assumes deviations around 3° and up to 7°, as discussed in [$A^+$08d] and references therein;
- The authors of [KST06] derive average deflections on the order of 1° to 3°, based on different galactic field models. Only one of these models produces deviations exceeding 10° for tracks going directly through the galactic centre;
- Galactic magnetic field models discussed in [TS09] cause deflections of up to 8°, but with average values $\sim 4°$;
- In [DGST05], extensive simulations of magnetic fields in galaxy clusters are described, with the conclusion that the impact of extra-galactic fields on UHECR propagation is negligible.

These and other references with similar conclusions imply average deflections on the order of a few degrees for UHECRs in the energy range under consideration.

To account for these magnetic deflections in the simulation, neutrino sources were individually shifted with respect to the UHECR directions. An average width of 3° was chosen for a Gaussian function according to which angular displacements values were generated. For each simulated map, individual shifts together with random orientations were produced for each of the 35 PAO or HiRes directions.

The cited predictions on the degree of deflection are derived under the assumption that UHECRs are dominated by protons. Deviations for heavier nuclei are expected to be significantly larger, due to a dependence on the charge. Such conditions would then strongly limit the advantages of a neutrino correlation approach compared to an unbiased all-sky search. For the purpose of the optimisation performed in this analysis, a proton domination is assumed, which seems to be favoured by some recent experimental results like [A$^+$10b].

The angular resolution of the air shower reconstruction for the chosen data is $\sim 0.8°$ for HiRes [A$^+$08c] and $\sim 0.9°$ for PAO [A$^+$08d] and was not considered as a separate effect, since not only magnetic deflections but also the IceCube angular resolution, discussed in the next section, cause larger uncertainties.

### Neutrino simulation

In absence of any information that would allow a calculation of individual neutrino expectations for the hypothetical cosmic ray sources, equal point source fluxes from all 35 UHECR directions were assumed in the simulation. Based on the discussion of astrophysical particle acceleration in section 2.1.2, the neutrino emission was modeled according to an $E^{-2}$ power law. In contrast to these uniform source conditions, the IceCube sensitivity varies with declination and energy. This is a result of energy cuts for down-going events from the southern hemisphere and absorption of up-going events, see section 6.4. A full neutrino simulation, including these effects, was used to determine the average number of neutrinos in the IceCube 22-strings final level selection which would be detected from each source direction for the total livetime of 276 days. Based on these mean values, neutrino event numbers for each source were generated in each trial according to a Poisson distribution.

The simulated events were distributed around the 35 source positions with the above prescription for magnetic shifts. An angular deviation was introduced for each event, following the IceCube point spread function from section 5.3. These deviations depend on declination and were implemented via a fitted function of azimuth and zenith errors from reconstruction results for simulated neutrinos. A detailed description is provided in [Mah09]. The generated signal events were placed into a background map, produced by scrambling the right ascensions of the 1885 measured events. To retain the original statistics, equal numbers of background events were removed, randomly chosen from the same declination bands as the added source neutrinos. Figure 9.3 shows a comparison between the resulting event count distributions with and without signal addition. In both

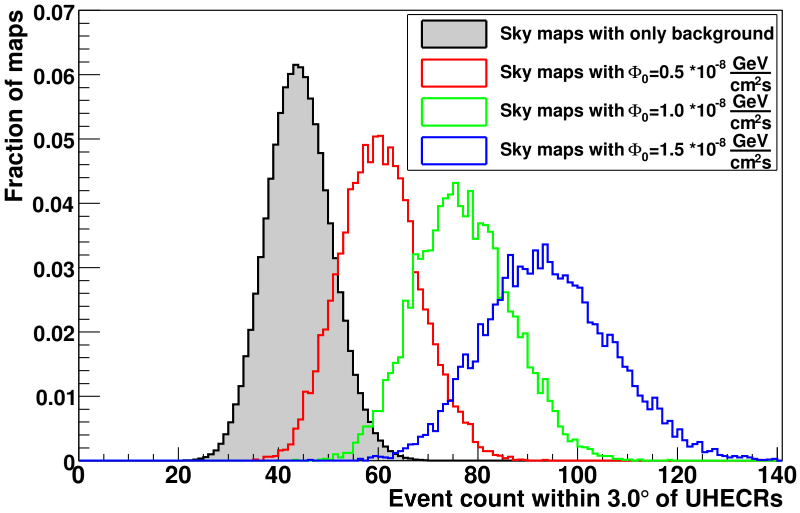

Figure 9.3.: Histograms of total event counts in bins of 3.0° radius around PAO & HiRes UHECR directions. The distribution from Fig 9.2 is compared to three cases with added neutrino signals, obtained from 10,000 scrambled maps each. One map contain 35 simulated sources, with a different flux strength $\Phi_0$ per source in each case.

cases, the search bin centres were defined by the measured, not the randomly shifted UHECR directions.

### 9.2.3. Search bin optimisation

The radius of the search bin, the only free parameter in the actual analysis prescription, was optimised with respect to the discovery potential. Histograms of the event counts for scrambled background distributions as shown in Fig. 9.2 were produced for different bin radii between 0.5° and 5.0°. From these, one obtained individual thresholds at which the chance probability of a counting result drops below the probability equivalent to a $5\sigma$ deviation for a one-sided Gaussian tail. The previously described simulations of sources with $E^{-2}$ spectra were then used to calculate the probability of observing total event numbers in excess of these thresholds in presence of a signal.

Figure 9.4 shows the resulting probabilities as a function of the bin radius. These curves make it possible to derive the optimal bin size. Since the statistics for maps with excesses above the $5\sigma$ threshold are limited even with $10^6$ trial runs, the discovery probability was also calculated at the $3\sigma$ level, to better estimate the position of the maximum. In conclusion, the simulations indicate an optimal radius of 3.0° for the correlation search.

For the discovery probabilities displayed in Fig. 9.4, the signal flux normalisation in $d\Phi/dE = \Phi_0 E^{-2}$ was chosen as $\Phi_0 = 1 \times 10^{-8}$ GeV cm$^{-2}$ s$^{-1}$. An investigation

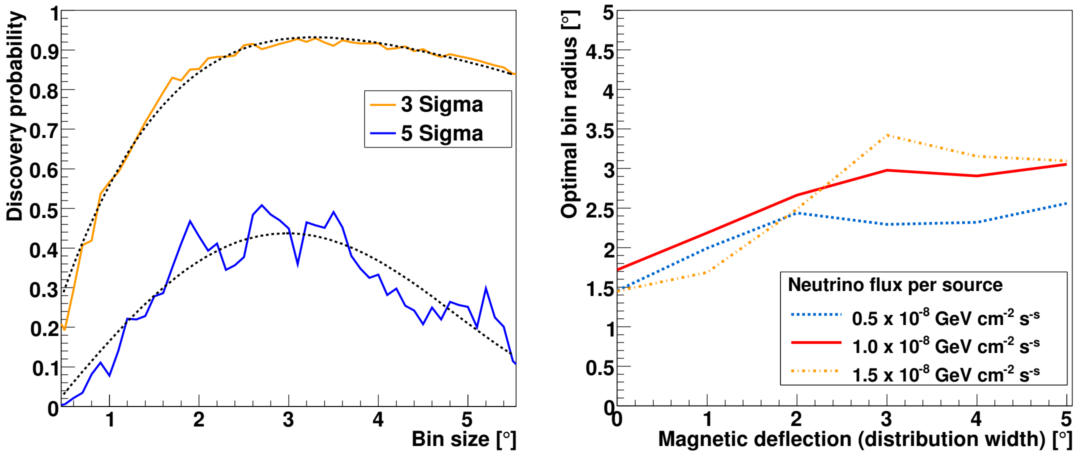

Figure 9.4.: *Left:* Discovery probability at $5\sigma$ and $3\sigma$ as a function of bin size, with polynomial fits. *Right:* Dependence of the optimal bin radius on variations of simulated magnetic deflection.

of the dependence of the optimisation on the flux strength per source showed only small variations for values up to $\Phi_0 = 2 \times 10^{-8}$ GeV cm$^{-2}$ s$^{-1}$. For larger fluxes, the number of signal events approaches the total background number in some declination bands, which is obviously unrealistic.

To test the influence of weaker or stronger magnetic deflections, the same simulations were performed with different source shifts, based on Gaussian distance distributions with widths varying between 0° and 5°. The right part of Fig. 9.4 shows the resulting optimised bin radii for these varying degrees of simulated magnetic deflection. The curves flatten out for mean deflections $> 3°$. This demonstrates that a larger bin size is not optimal even for increased probabilities of sources lying outside the search area. The explanation for this behaviour is the worse signal-to-background ratio for too large bins.

An optimisation for a low flux per source would lead to slightly smaller bins than 3°, but the following section shows that a value $\Phi_0 < 1 \times 10^{-8}$ GeV cm$^{-2}$ s$^{-1}$ would anyway reduce the chances of discovery below 50%. In summary, the tests with varying simulation parameters confirm the conclusion of 3.0° being the optimal value.

### 9.2.4. Discovery potential

After fixing the bin size, the $E^{-2}$ neutrino flux per source required for a $5\sigma$ discovery in 50% of trials was determined by calculating the discovery probability for different flux normalizations, as shown in Fig. 9.5. The comparison of the curve with the chosen bin radius of 3° to those for 2.5° and 3.5° illustrates that small changes of the bin size do not strongly influence the final discovery probability.

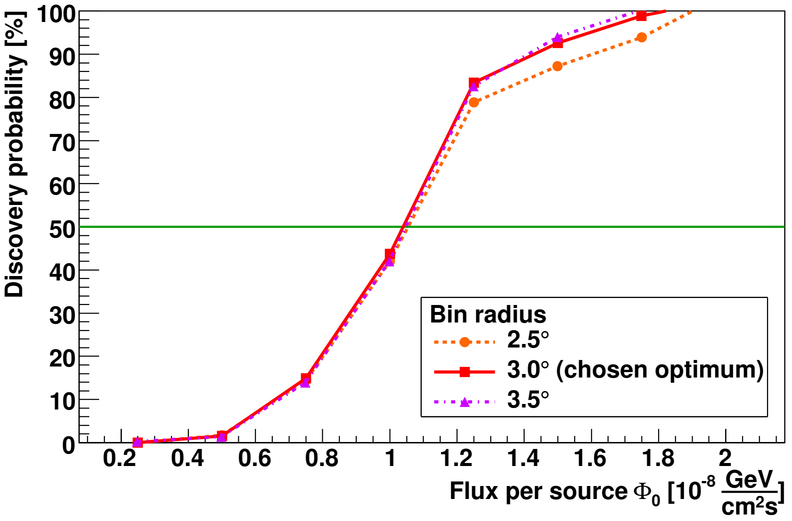

Figure 9.5.: Discovery probability (at $5\sigma$) in dependence of the signal flux strength per source. The curves for 2.5° and 3.5° are shown for comparison to the chosen optimal bin radius of 3°.

The discovery potential defined in this way corresponds to a flux per source of $\Phi_0 = 1.0 \times 10^{-8}$ GeV cm$^{-2}$ s$^{-1}$, resulting in an average number of 76 signal events in the full event sample. Summing over the limited search areas of the 35 bins, one would then expect on average a contribution of 36.8 signal neutrinos on a background of 40.9 events.

The total signal contribution from all sources can be compared to the diffuse flux limit for muon neutrinos to understand if the flux required for a $5\sigma$ detection has already been excluded by other analyses. The solid angle integration for the IceCube 22 strings field of view results in a value of $\Omega = 3.6 \times \pi$ sr, hence it has to be checked if the inequality

$$35 \times \Phi_0 < \Phi_{\mathrm{lim},\mu} \times 3.6 \times \pi \tag{9.1}$$

is fulfilled. The best published flux limit for an $E^{-2}$ neutrino spectrum is provided in the AMANDA-II analysis in [A+08g] with an all-flavour value of $\Phi_{\mathrm{lim}} = 2.7 \times 10^{-7}$ GeV cm$^{-2}$ s$^{-1}$ sr$^{-1}$. It is valid in the energy range $10^5$ to $10^9$ GeV, which is comparable to the one for this event sample, see section 6.13. Assuming equal flavour ratios according to section 3.1.1, the flux limit is divided by 3 to obtain a value for muon neutrinos only. This leads to an upper limit on the average flux per source:

$$\Phi_0 < \frac{\Phi_{\mathrm{lim}} \times 3.6 \times \pi\,\mathrm{sr}}{3 \times 35} = 2.9 \times 10^{-8}\,\mathrm{GeV\ cm^{-2}\,s^{-1}}\,. \tag{9.2}$$

Thus, the flux levels necessary for a $5\sigma$ detection are still below the excluded

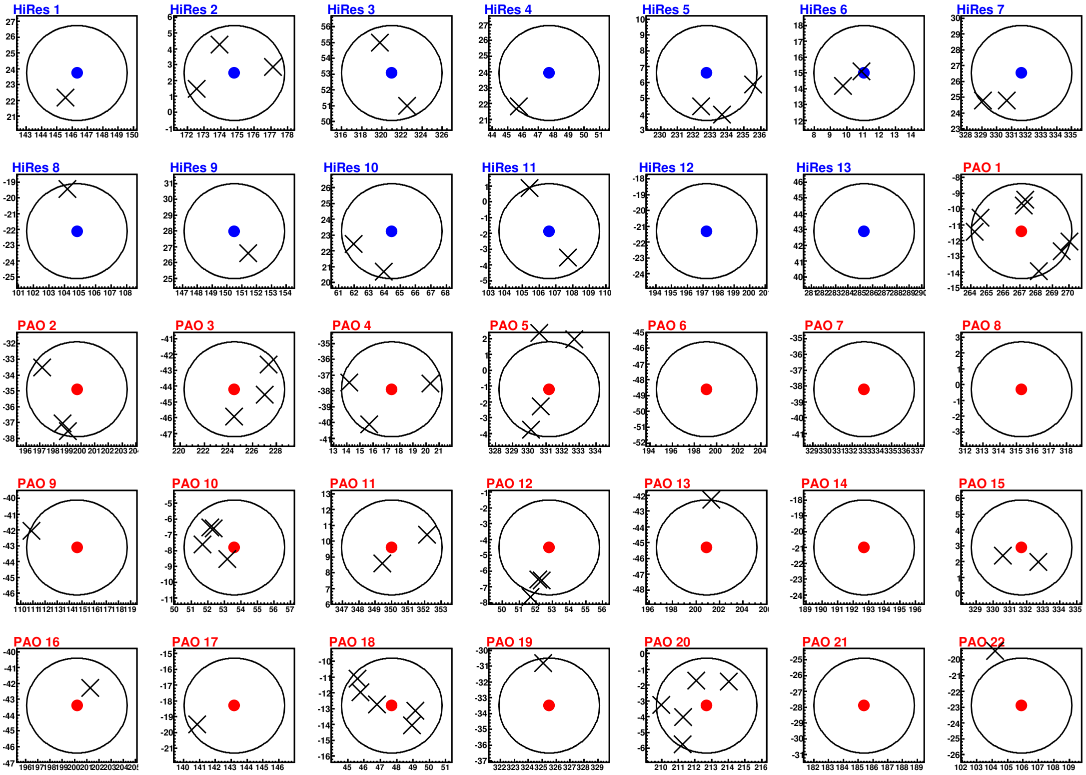

Figure 9.6.: Zoomed sky map regions around the 35 unblinded UHECR directions (blue and red dots) with indicated bin areas (3° radius) and IceCube events (crosses). The x-axes show right ascension, the y-axes declination, both in degrees.

limits.

## 9.3. Results

After applying the analysis prescription to the IceCube data by scanning the 35 bins of 3° radius, a total of 60 events were observed. The mean background expectation based on scrambled sky maps was 43.7 events. The probability for an excess of the same or a larger magnitude within the background-only scenario is 0.0098, i.e. $2.3\sigma$ as one-sided Gaussian equivalent. In conclusion, this result is regarded as being compatible with a background fluctuation.

A check of the event count in each bin showed the largest individual upward fluctuation to be 7 events where 2.3 were expected, within a 3° radius around the direction 267.1° r.a., -11.4° dec. On its own, this would correspond to a significance of $2.4\sigma$. No particularly strong clustering of IceCube events on a smaller scale than the bin size was observed in any tested direction, see Fig. 9.6.

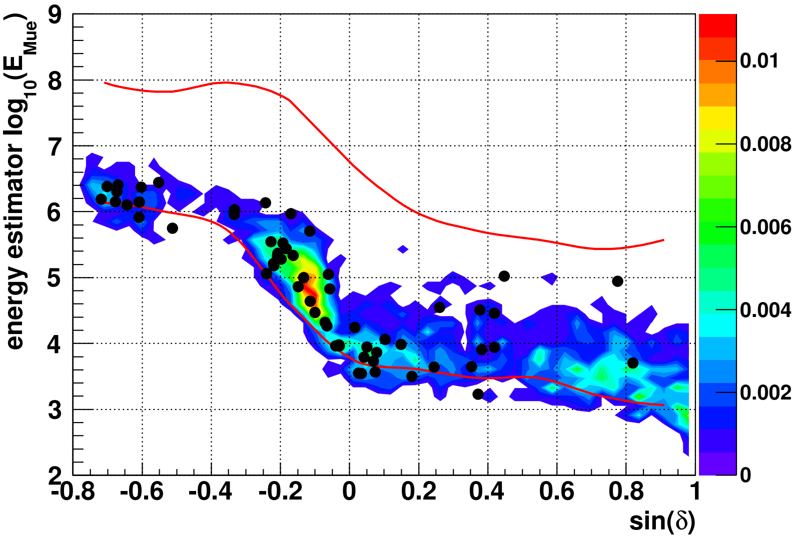

Figure 9.7.: Estimated energies in dependence of declination for the 60 events (black dots) correlated with UHECR directions. The coloured contours highlight the distribution of all events in the final sample, while the red lines indicate the upper and lower boundaries within which 90% of an $E^{-2}$ neutrino signal flux is expected.

The muon energies calculated with *Mue*, introduced in section 5.4, for the 60 IceCube events were inspected but no unusual values were observed. Figure 9.7 shows that the distribution of this energy estimator versus declination basically matches that of the background data.

Under the emission hypothesis of equal neutrino fluxes from all 35 PAO and HiRes UHECR directions, the result can be used to derive an upper limit on the flux normalisation per source. Confidence belts for the total event counts were constructed with the method of [FC98] introduced in section 3.2.2. Given the observed 60 events, a limit of $\Phi_{\rm lim} = 0.9 \times 10^{-8}$ GeV cm$^{-2}$ s$^{-1}$ on the muon neutrino flux per source was obtained, assuming a mean magnetic deflection of 3°. Since this uniform emission scenario is only a simplified framework for interpreting the event counts, the limit should be considered only as an average value for the level of excluded fluxes.

# Chapter 10.

# Summary and outlook

> *"We all live under the same sky, but we do not all have the same horizon."*
>
> Aesop, ca. 600 BC

Measurements of charged cosmic rays with energies up to $10^{20}$ eV provide strong evidence for the existence of efficient astrophysical acceleration of particles that are expected to generate a flux of secondary neutrinos. Observing such neutrinos from point-like origins would be a robust way of identifying sources of hadronic cosmic rays. In particular in the range between TeV and low EeV energies, where photons from extra-galactic sources suffer strong absorption and charged particles are scrambled by galactic magnetic fields, neutrinos are unique cosmic messengers.

Neutrino astronomy is still a young field of research, and the first discovery of high energy neutrinos from astrophysical sources has yet to be established. The IceCube Observatory, even in the configuration of 22 strings, only a quarter of the final extension, is the largest operating neutrino telescope. In this work, a new analysis approach was introduced that increases the sensitivity of IceCube both in energy and sky coverage and provides new astrophysical flux limits.

The established technique to detect high energy neutrinos and reconstruct their tracks relies on the precise measurement of Cherenkov light with extended subsurface arrays of photo-multipliers. Muon neutrinos undergoing a charged current interaction inside, or in the vicinity of, the detector volume produce muons which emit Cherenkov radiation, directly and via showers of secondary particles. In IceCube, a nanosecond resolution for detecting these photons makes it possible to reconstruct the track directions. The precision is limited mostly by the scattering of light in the ice. It was shown in this work that an extended likelihood algorithm significantly improves the reconstruction performance at PeV energies. This extended probability density function for the detection time of the first photon pulse takes into account the total number of photoelectrons in the same module, instead of simply ignoring later hits as was done in track reconstructions for previous point source searches with IceCube and AMANDA. The resulting angular resolution with the IceCube 22-strings configuration is $\sim 1.3°$ for a quality selection of neutrino events with an $E^{-2}$ energy spectrum signal hypothesis.

The background of atmospheric muons, produced in extensive air showers and penetrating to the IceCube detector depth, is $10^6$ times larger than any signal expectation and thus a major challenge when performing a neutrino analysis. An established method to suppress these events is the exclusive selection of tracks which are upward going and hence must stem from neutrinos travelling through Earth. A point-like signal can then be searched for among the small remaining background flux of atmospheric neutrinos, generated also in air showers. However, since the relevant interaction cross sections of the weak force rise with energy, Earth becomes opaque for neutrinos at PeV energies. Furthermore, with IceCube located at the South Pole, the upward-only approach does not permit to study the southern hemisphere.

In this work it was shown that selection methods sensitive to energy and light distribution provide the means to reduce also the downward going muon background. It can be suppressed to a level which makes it possible to search for excesses due to neutrinos from astrophysical point sources. Selection cuts, varying with track zenith angles, were used to define a final event sample covering the region below the horizon as well as a large part of the sky above the horizon. The lower energy threshold rises from the TeV level for the up-going to PeV energies for the down-going directions. Neutrinos from the southern hemisphere, for which absorption in Earth plays no role, can reach IceCube even up to EeV energies and thus make the search sensitive to a previously uncovered regime.

After the definition of the event selection and analysis strategy, following a strict blindness procedure, the reconstructed directions of the tracks from the final sample were used to search for directional clustering of neutrinos. The grid search, covering the sky with overlapping circular bins between declinations $-50°$ and $+85°$, showed no significant excesses above fluctuations expected from the background event distribution.

A separate test was performed for a list of 28 pre-defined candidates, mostly AGN classified as blazars for which strong gamma-ray emissions have been reported. For none of these directions did the observed neutrino numbers lie above values expected from the background-only hypothesis. After accounting for systematic uncertainties, new upper limits on the neutrino fluxes from the chosen source candidates were derived. Many of these constitute the best existing neutrino bounds in the covered energy range, in particular for southern hemisphere objects such as the AGN Centaurus A and the centre of our galaxy Sgr $A^*$.

For the blazar 3C279, variable photon fluxes in different wavebands motivated a dedicated search for neutrino flares by including timing information, as opposed to the time-integrated search for steady sources. Based on available light curves, four intervals spanning a total of 25.4 days were selected as promising for neutrino emissions, but no IceCube events could be found in these periods. The first upper limit on neutrino fluxes above TeV energies from 3C279 was derived and discussed in the context of a specific model prediction.

The sample of high energy IceCube events was also used to study directional correlations between these neutrino candidates and charged cosmic rays measured by the HiRes experiment and the Pierre Auger Observatory at energies above $6 \times 10^{19}$ eV. These data were used as reference directions in a binned search. Magnetic deflection of the charged particles has to be considered but is likely to be small enough to allow in principal an identification of common source regions of neutrinos and UHECRs. Counting IceCube events within 3° angular distance of 35 cosmic ray directions revealed 60 coincidences while on average 44 were expected. This result is compatible with the background hypothesis at a level of $\sim 1\%$ probability.

The extension of IceCube point source searches to the southern sky opened a new observation window for high energy neutrino astronomy. The results from the point source search and candidate source tests obtained in the work presented here have been published in a refereed journal [$A^+$09b]. Using an energy-sensitive suppression of the atmospheric muon background from above the horizon and performing a unified point source analysis over both hemispheres has already been adopted in the IceCube collaboration as a new standard approach for future searches. A point source search on new IceCube data, taken between spring 2008 and spring 2009 with a configuration of 40 strings, has been prepared in this fashion, with the unblinding of the actual track directions to be expected for early 2010.

The inclusion of downward going events in such analyses provides the opportunity to probe possible neutrino sources at and above PeV energies. This new data helps to test models of astrophysical particle acceleration and increases the chances of finding the first cosmic neutrino signals. It should be possible to adopt the analysis technique presented here for application in other neutrino telescopes, for example Antares or the planned cubic kilometer scale detector in the Mediterranean sea. Being instruments in the northern hemisphere, they would then provide a complementary sky coverage with a reversed meaning of above and below the horizon. These and other experimental efforts can thus contribute in unique ways to neutrino astronomy and help establish it as a new window into the high energy Universe.

# Appendix A.

# Event selection cuts

Listed in the following are all event selection cuts used for the analysis presented in this work. They were applied to SMT-triggered data, taken in the 22-strings IceCube configuration between May 2007 and April 2008. Details are described in chapter 6.

## Level 1

$$\begin{array}{llll}
 & \{\ \text{NChannel} \geq 80 & & \} \\
\text{OR} & \{\ \text{NChannel} \geq 50 & \text{AND} \quad \theta \geq 50^\circ & \} \\
\text{OR} & \{\ \text{NChannel} \geq 60 & \text{AND} \quad \theta \geq 40^\circ & \} \\
\text{OR} & \{\ \text{NChannel} \geq 70 & \text{AND} \quad \theta \geq 10^\circ & \}
\end{array}$$

The zenith angle $\theta$ is based on *linefit* reconstruction. Median angular resolution, averaged over all energies for an $E^{-2}$ spectrum, is $\sim 10^\circ$ at this level. The average data rate is 23.6 Hz.

## Level 2

*No cuts applied*
Processing of SPE reconstruction.

## Level 3

$$\begin{aligned}
&\{\text{ zenith angle } \theta \geq 40^\circ \text{ }\}\\
\text{AND } &\{\text{ NChannel} \geq 20 \text{ AND } \theta < 80^\circ \text{ }\}\\
\text{AND } &\{\text{ reduced log-likelihood} \leq 9 \text{ }\}
\end{aligned}$$

The zenith angle $\theta$ is based on SPE reconstruction. Cuts were reapplied after processing of the MPE fit, with an improved median angular resolution of 2.8° at this level. The average data rate is 2.7 Hz.

## Level 4

$$\begin{aligned}
&\{\text{NHits/NCh} \geq 0.1667 \cdot (26.099315 \cdot \exp((Y{-}4.167702)^2/(2 \cdot 0.642915)))\\
&\qquad\qquad\qquad\qquad \text{AND } (X \geq -0.80 \text{ AND } X < -0.75)\}\\
\text{OR } &\{\text{NHits/NCh} \geq 0.1667 \cdot (50.172586 \cdot \exp((Y{-}4.160476)^2/(2 \cdot 0.637656)))\\
&\qquad\qquad\qquad\qquad \text{AND } (X \geq -0.75 \text{ AND } X < -0.70)\}\\
\text{OR } &\{\text{NHits/NCh} \geq 0.1667 \cdot (53.156619 \cdot \exp((Y{-}4.111670)^2/(2 \cdot 0.630833)))\\
&\qquad\qquad\qquad\qquad \text{AND } (X \geq -0.70 \text{ AND } X < -0.65)\}\\
\text{OR } &\{\text{NHits/NCh} \geq 0.1667 \cdot (63.001920 \cdot \exp((Y{-}4.059982)^2/(2 \cdot 0.596489)))\\
&\qquad\qquad\qquad\qquad \text{AND } (X \geq -0.65 \text{ AND } X < -0.60)\}\\
\text{OR } &\{\text{NHits/NCh} \geq 0.1667 \cdot (64.525712 \cdot \exp((Y{-}4.034918)^2/(2 \cdot 0.584852)))\\
&\qquad\qquad\qquad\qquad \text{AND } (X \geq -0.60 \text{ AND } X < -0.55)\}\\
\text{OR } &\{\text{NHits/NCh} \geq 0.1667 \cdot (63.524860 \cdot \exp((Y{-}3.997122)^2/(2 \cdot 0.580141)))\\
&\qquad\qquad\qquad\qquad \text{AND } (X \geq -0.55 \text{ AND } X < -0.50)\}\\
\text{OR } &\{\text{NHits/NCh} \geq 0.1667 \cdot (63.957859 \cdot \exp((Y{-}3.935059)^2/(2 \cdot 0.573148)))\\
&\qquad\qquad\qquad\qquad \text{AND } (X \geq -0.50 \text{ AND } X < -0.45)\}\\
\text{OR } &\{\text{NHits/NCh} \geq 0.1667 \cdot (59.022136 \cdot \exp((Y{-}3.850516)^2/(2 \cdot 0.615833)))\\
&\qquad\qquad\qquad\qquad \text{AND } (X \geq -0.45 \text{ AND } X < -0.40)\}\\
\text{OR } &\{\text{NHits/NCh} \geq 0.1667 \cdot (61.329891 \cdot \exp((Y{-}3.763927)^2/(2 \cdot 0.573127)))\\
&\qquad\qquad\qquad\qquad \text{AND } (X \geq -0.40 \text{ AND } X < -0.35)\}\\
\text{OR } &\{\text{NHits/NCh} \geq 0.1667 \cdot (62.652994 \cdot \exp((Y{-}3.662792)^2/(2 \cdot 0.547664)))\\
&\qquad\qquad\qquad\qquad \text{AND } (X \geq -0.35 \text{ AND } X < -0.30)\}\\
\text{OR } &\{\text{NHits/NCh} \geq 0.1667 \cdot (51.334448 \cdot \exp((Y{-}3.647328)^2/(2 \cdot 0.542361)))\\
&\qquad\qquad\qquad\qquad \text{AND } (X \geq -0.30 \text{ AND } X < -0.25)\}\\
\text{OR } &\{\text{NHits/NCh} \geq 0.1667 \cdot (34.489781 \cdot \exp((Y{-}3.675171)^2/(2 \cdot 0.565939)))\\
&\qquad\qquad\qquad\qquad \text{AND } (X \geq -0.25 \text{ AND } X < -0.20)\}\\
\text{OR } &\{\text{NHits/NCh} \geq 0.1667 \cdot (22.675467 \cdot \exp((Y{-}3.684569)^2/(2 \cdot 0.631203)))\\
&\qquad\qquad\qquad\qquad \text{AND } (X \geq -0.20 \text{ AND } X < -0.15)\}\\
\text{OR } &\{\text{NHits/NCh} \geq 0.1667 \cdot (15.888966 \cdot \exp((Y{-}3.713399)^2/(2 \cdot 0.701842)))\\
&\qquad\qquad\qquad\qquad \text{AND } (X \geq -0.15 \text{ AND } X < -0.10)\}\\
\text{OR } &\{\text{NHits/NCh} \geq 0.1667 \cdot (12.552754 \cdot \exp((Y{-}3.824859)^2/(2 \cdot 0.677800)))\\
&\qquad\qquad\qquad\qquad \text{AND } (X \geq -0.10 \text{ AND } X < -0.05)\}\\
\text{OR } &\{\text{NHits/NCh} \geq 0.1667 \cdot (11.101543 \cdot \exp((Y{-}3.847754)^2/(2 \cdot 0.686220)))\\
&\qquad\qquad\qquad\qquad \text{AND } (X \geq -0.05 \text{ AND } X < 0.00)\}
\end{aligned}$$

$X = -\cos(\theta)$ and $Y = Mue$ energy estimator
The zenith angle $\theta$ is based on MPE reconstruction with 2.8° median angular resolution at this level. The average data rate is 0.3 Hz.

## Level 5

$$
\begin{array}{llll}
\{ & & (\text{ bayes-ratio} \geq 0.0 & \text{AND } z < -0.3\ ) \\
 & \text{OR} & (\text{ bayes-ratio} \geq 100.0 \cdot z + 30.0 & \text{AND } z \geq -0.3 \text{ AND } z < 0.0\ ) \\
 & \text{OR} & (\text{ bayes-ratio} \geq 30.0 & \text{AND } z \geq 0.0\ )\ \} \\
\text{AND} & & & \\
\{ & & (\text{ NHits/NCh} \geq 22.0 & \text{AND } z < -0.4\ ) \\
 & \text{OR} & (\text{ NHits/NCh} \geq -60.0 \cdot z - 2.0 & \text{AND } z \geq -0.4 \text{ AND } z < -0.05\ ) \\
 & \text{OR} & (\text{ NHits/NCh} \geq 1.0 & \text{AND } z \geq -0.05\ )\ \} \\
\text{AND} & & & \\
\{ & & (\qquad \text{NCh } \geq 83 & \text{AND } z < -0.2\ ) \\
 & \text{OR} & (\qquad \text{NCh } \geq -240 \cdot z + 35 & \text{AND } z \geq -0.2 \text{ AND } z < -0.0\ ) \\
 & \text{OR} & (\qquad \text{NCh } \geq -9 \cdot z + 35 & \text{AND } z \geq 0.0\ )\ \} \\
\text{AND} & & & \\
\{ & & (\text{ red. log-llh} \leq -3.0 \cdot z + 7.6 & \text{AND } z < 0.0\ ) \\
 & \text{OR} & (\text{ red. log-llh} \leq 7.6 \cdot z & \text{AND } z \geq 0.0\ )\ \} \\
\text{AND} & & & \\
\{ & & (\text{ parab. } \sigma \quad \leq 1.5 & \text{AND } z < 0.0\ ) \\
 & \text{OR} & (\text{ parab. } \sigma \quad \leq 1.0 \cdot z + 1.5 & \text{AND } z \geq 0.0\ )\ \} \\
\text{AND} & & & \\
\{ & & (\qquad \text{NDir } \geq 0.0 & \text{AND } z < 0.0\ ) \\
 & \text{OR} & (\qquad \text{NDir } \geq 30.0 & \text{AND } z \geq 0.0\ )\ \}
\end{array}
$$

$z = -\cos(\theta)$
Median angular resolution is 1.3° at final level. The average data rate is $8 \times 10^{-5}$ Hz.

# List of Figures

# Bibliography

[A$^+$95] Askebjer, P.; et al. (AMANDA): Optical properties of the South Pole ice at depths between 0.8-km and 1-km. In: *Science*, volume 267:pp. 1147–1150, 1995. `arXiv:astro-ph/9412028`.

[A$^+$97a] Askebjer, P.; et al. (AMANDA): Optical properties of deep ice at the South Pole: absorption. In: *Appl. Opt.*, volume 36(18):pp. 4168–4180, 1997.

[A$^+$97b] Askebjer, P.; et al. (AMANDA): UV and optical light transmission properties in deep ice at the South Pole. In: *Geophysical Research Letters*, volume 24(11):pp. 1355–1358, 1997.

[A$^+$00] Andres, E.; et al. (AMANDA): The AMANDA neutrino telescope: Principle of operation and first results. In: *Astropart. Phys.*, volume 13:pp. 1–20, 2000. `arXiv:astro-ph/9906203`.

[A$^+$01] Ambrosio, M.; et al. (MACRO): Neutrino astronomy with the MACRO detector. In: *Astrophys. J.*, volume 546:pp. 1038–1054, 2001. `arXiv:astro-ph/0002492`.

[A$^+$04a] Abraham, J.; et al. (Pierre Auger): Properties and performance of the prototype instrument for the Pierre Auger Observatory. In: *Nucl. Instrum. Meth. A*, volume 523(1–2):pp. 50–95, 2004.

[A$^+$04b] Aharonian, F.; et al. (HEGRA): Observations of 54 Active Galactic Nuclei with the HEGRA system of Cherenkov telescopes. In: *Astron. Astrophys.*, volume 421(2):pp. 529–537, 2004.

[A$^+$04c] Ahrens, J.; et al. (AMANDA): Muon track reconstruction and data selection techniques in AMANDA. In: *Nucl. Instrum. Meth. A*, volume 524:pp. 169–194, 2004. `arXiv:astro-ph/0407044`.

[A$^+$06a] Achterberg, A.; et al. (IceCube): On the selection of AGN neutrino source candidates for a source stacking analysis with neutrino telescopes. In: *Astropart. Phys.*, volume 26:pp. 282–300, 2006. `arXiv:astro-ph/0609534`.

[A$^+$06b] Ackermann, M.; et al. (IceCube): Optical properties of deep glacial ice at the South Pole. In: *Journal of Geophysical Research D*, volume 111(13):p. 13203, 2006.

[A$^+$06c] Aggouras, G.; et al. (NESTOR): Recent results from NESTOR. In: *Nucl. Instrum. Meth. A*, volume 567:pp. 452–456, 2006.

[A$^+$06d] Aguilar, J.A.; et al. (ANTARES): First results of the instrumentation line for the deep-sea ANTARES neutrino telescope. In: *Astropart. Phys.*, volume 26:pp. 314–324, 2006. `arXiv:astro-ph/0606229`.

[A$^+$06e] Aharonian, F.; et al. (H.E.S.S.): A Low level of extragalactic background light as revealed by gamma-rays from blazars. In: *Nature*, volume 440:pp. 1018–1021, 2006. `arXiv:astro-ph/0508073`.

[A$^+$06f] Ahrens, J.; et al. (IceCube): IceCube preliminary design document, 2006. URL `http://icecube.wisc.edu/science/publications/pdd/pddwhole.php`.

[A+07a] Abraham, J.; et al. (Pierre Auger): Correlation of the highest energy cosmic rays with nearby extragalactic objects. In: *Science*, volume 318:pp. 938–943, 2007. `arXiv:0711.2256[astro-ph]`.

[A+07b] Achterberg, A.; et al. (IceCube): Five years of searches for point sources of astrophysical neutrinos with the AMANDA-II neutrino telescope. In: *Phys. Rev. D*, volume 75:p. 102001, 2007.

[A+07c] Ackermann, M.; et al.: Neutrino Triggered Target of Opportunity (NToO) test run with AMANDA-II and MAGIC. In: *Proc. of the 30th ICRC, Mérida, Yucatan, Mexico*. Universidad Nacional Autónoma de México, Mexico City, 2007. `arXiv:0709.2640[astro-ph]`.

[A+08a] Abbasi, R.; et al. (HiRes): First Observation of the Greisen-Zatsepin-Kuzmin Suppression. In: *Phys. Rev. Lett.*, volume 100:p. 101101, 2008. `arXiv:astro-ph/0703099`.

[A+08b] Abbasi, R.U.; et al. (HiRes): An Upper Limit on the Electron-Neutrino Flux from the HiRes Detector. In: *Astrophys. J.*, volume 684(2):pp. 790–793, 2008. `arXiv:0803.0554[astro-ph]`.

[A+08c] Abbasi, R.U.; et al. (HiRes): Search for Correlations between HiRes stereo events and Active Galactic Nuclei. In: *Astropart. Phys.*, volume 30:pp. 175–179, 2008. Event list: http://www.physics.rutgers.edu/~lsct/, `arXiv:0804.0382[astro-ph]`.

[A+08d] Abraham, J.; et al. (Pierre Auger): Correlation of the highest-energy cosmic rays with the positions of nearby active galactic nuclei. In: *Astropart. Phys.*, volume 29:pp. 188–204, 2008. `arXiv:0712.2843[astro-ph]`.

[A+08e] Abraham, J.; et al. (Pierre Auger): Observation of the suppression of the flux of cosmic rays above $4 \times 10^{19}$eV. In: *Phys. Rev. Lett.*, volume 101:p. 061101, 2008. `arXiv:0806.4302[astro-ph]`.

[A+08f] Abraham, J.; et al. (Pierre Auger): Upper limit on the cosmic-ray photon flux above $10^{19}$ eV using the surface detector of the Pierre Auger Observatory. In: *Astropart. Phys.*, volume 29:pp. 243–256, 2008. `arXiv:0712.1147[astro-ph]`.

[A+08g] Ackermann, M.; et al. (IceCube): Search for ultra high-energy neutrinos with AMANDA-II. In: *Astrophys. J.*, volume 675:p. 1014, 2008. `arXiv:0711.3022[astro-ph]`.

[A+08h] Aliu, E.; et al. (MAGIC): Very-High-Energy Gamma Rays from a Distant Quasar: How Transparent Is the Universe? In: *Science*, volume 320:p. 1752, 2008. `arXiv:0807.2822[astro-ph]`.

[A+09a] Abbasi, R.; et al. (IceCube): Determination of the Atmospheric neutrino flux and searches for new physics with AMANDA-II. In: *Phys. Rev. D*, volume 79:p. 102005, 2009. `arXiv:0902.0675[astro-ph]`.

[A+09b] Abbasi, R.; et al. (IceCube): Extending the search for neutrino point sources with IceCube above the horizon. In: *Phys. Rev. Lett.*, volume 103:p. 221102, 2009. `arXiv:0911.2338[astro-ph]`.

[A+09c] Abbasi, R.; et al. (IceCube): First neutrino point-source results from the 22-string IceCube detector. In: *Astrophys. J.*, volume 701:pp. L47–L51, 2009. `arXiv:0905.2253[astro-ph]`.

[A$^+$09d] Abbasi, R.; et al. (IceCube): Limits on a muon flux from neutralino annihilations in the Sun with the IceCube 22-string detector. In: *Phys. Rev. Lett.*, volume 102:p. 201302, 2009. `arXiv:0902.2460[astro-ph]`.

[A$^+$09e] Abbasi, R.; et al. (IceCube): Search for high-energy muon neutrinos from the 'naked-eye' GRB 080319B with the IceCube neutrino telescope. In: *Astrophys. J.*, volume 701:pp. 1721–1731, 2009.

[A$^+$09f] Abbasi, R.; et al. (IceCube): The IceCube data acquisition system: Signal capture, digitization, and timestamping. In: *Nucl. Instrum. Meth. A*, volume 601:p. 294, 2009.

[A$^+$09g] Abbasi, R.U.; et al. (HiRes): Measurement of the Flux of Ultra High Energy Cosmic Rays by the Stereo Technique. In: *Astropart. Phys.*, volume 32:pp. 53–60, 2009. `arXiv:0904.4500[astro-ph]`.

[A$^+$09h] Abdo, A. A.; et al. (Fermi/LAT): Fermi/large area telescope bright gamma-ray source list. In: *Astrophys. J. Suppl.*, volume 183(1):pp. 46–66, 2009.

[A$^+$09i] Abraham, J.; et al. (Pierre Auger): Limit on the diffuse flux of ultra-high energy tau neutrinos with the surface detector of the Pierre Auger Observatory. In: *Phys. Rev. D*, volume 79:p. 102001, 2009. `arXiv:0903.3385[astro-ph]`.

[A$^+$09j] Abraham, J.A.; et al. (Pierre Auger): The Fluorescence Detector of the Pierre Auger Observatory, 2009. `arXiv:0907.4282[astro-ph]`.

[A$^+$09k] Aharonian, F.; et al. (H.E.S.S.): Discovery of very high energy gamma-ray emission from Centaurus A with H.E.S.S. In: *Astrophys. J.*, volume 695(1):pp. L40–L44, 2009.

[A$^+$10a] Abbasi, R.; et al. (IceCube): Search for muon neutrinos from Gamma-Ray Bursts with the IceCube neutrino telescope. In: *Astrophys. J.*, 2010. Submitted to ApJ, `arXiv:0907.2227[astro-ph]`.

[A$^+$10b] Abbasi, R.U.; et al. (HiRes): Indications of Proton-Dominated Cosmic Ray Composition above 1.6 EeV. In: *Phys. Rev. Lett.*, volume 104:p. 161101, 2010. `arXiv:0910.4184[astro-ph]`.

[Ack06] Ackermann, M.: *Searches for signals from cosmic point-like sources of high energy neutrinos in 5 years of AMANDA-II data.* Ph.D. thesis, Humboldt-Universität zu Berlin, 2006.

[AD04] Atoyan, A.M.; Dermer, C.D.: Neutrinos and gamma-rays of hadronic origin from AGN jets. In: *New Astronomy Reviews*, volume 48(5-6):pp. 381–386, 2004. 2nd VERITAS Symposium on the Astrophysics of Extragalactic Sources.

[AJY00] Athar, H.; Jezabek, M.; Yasuda, O.: Effects of neutrino mixing on high-energy cosmic neutrino flux. In: *Phys. Rev. D*, volume 62:p. 103007, 2000. `arXiv:hep-ph/0005104`.

[AN05] Aharonian, F.; Neronov, A.: High energy gamma rays from the massive black hole in the galactic center. In: *Astrophys. J.*, volume 619:pp. 306–313, 2005. `arXiv:astro-ph/0408303`.

[AS07] Aguilar Sánchez, J.A.: Expected discovery potential and sensitivity to neutrino point-like sources of the ANTARES neutrino telescope. In: *Proc. of the 30th ICRC, Mérida, Mexico.* Universidad Nacional Autónoma de México, Mexico City, 2007.

[AZ+99] Abu-Zayyad, T.; et al. (HiRes): Status of the High Resolution Fly's Eye Detector: Operation and installation. In: *Proc. of the 26th ICRC, Salt Lake City, USA*, volume 5, p. 349. 1999.

[B+90] Babson, J.; et al.: Cosmic-ray muons in the deep ocean. In: *Phys. Rev. D*, volume 42(11):pp. 3613–3620, 1990.

[B+00] Balkanov, V.; et al.: An upper limit on the diffuse flux of high energy neutrinos obtained with the Baikal detector NT-96. In: *Astropart. Phys.*, volume 14:pp. 61–66, 2000.

[BABL09] Bazo Alba, J.L.; Bernardini, E.; Lauer, R.: Search for neutrino flares from point sources with IceCube. In: *Proc. of the 31st ICRC, Łódź, Poland.* 2009. `arXiv:0908.4209[astro-ph]`.

[BBW+05] Bramall, N.E.; Bay, R.C.; Woschnagg, K.; Rohde, R.A.; Price, P.B.: A deep high-resolution optical log of dust, ash, and stratigraphy in South Pole glacial ice. In: *Geophysical Research Letters*, volume 32:p. L21815, 2005.

[BCK02] Beacom, J.F.; Crotty, P.; Kolb, E.W.: Enhanced signal of astrophysical tau neutrinos propagating through Earth. In: *Phys. Rev. D*, volume 66(2):p. 021302, 2002.

[BDdP+08] Braun, J.; Dumm, J.; de Palma, F.; Finley, C.; Karle, A.; Montaruli, T.: Methods for point source analysis in high energy neutrino telescopes. In: *Astropart. Phys.*, volume 29:pp. 299–305, 2008. `arXiv:0801.1604[astro-ph]`.

[Bec08] Becker, J.K.: High-energy neutrinos in the context of multimessenger physics. In: *Phys. Rept.*, volume 458:pp. 173–246, 2008. `arXiv:0710.1557[astro-ph]`.

[BEH09] Bluemer, J.; Engel, R.; Hoerandel, J.R.: Cosmic Rays from the Knee to the Highest Energies. In: *Prog. Part. Nucl. Phys.*, volume 63:pp. 293–338, 2009. `arXiv:0904.0725[astro-ph]`.

[Bel78] Bell, A.R.: The acceleration of cosmic rays in shock fronts I & II. In: *Mon. Not. R. Astron. Soc.*, volume 182:p. 147 and 443, 1978.

[Ber96] Berezhko, E.G.: Maximum energy of cosmic rays accelerated by supernova shocks. In: *Astropart. Phys.*, volume 5(3-4):pp. 367–378, 1996. ISSN 0927-6505.

[Ber09] Berghaus, P.: Direct measurement of the atmospheric muon energy spectrum with IceCube. In: *Proc. of the 31st ICRC, Łódź, Poland.* 2009.

[BGL+04] Barr, G.D.; Gaisser, T.K.; Lipari, P.; Robbins, S.; Stanev, T.: A three-dimensional calculation of atmospheric neutrinos. In: *Phys. Rev. D*, volume 70(2):p. 023006, 2004. `arXiv:astro-ph/0403630`.

[BKMS02] Boyer, J.H.; Knapp, B.C.; Mannel, E.J.; Seman, M.: FADC-based DAQ for HiRes Fly's Eye. In: *Nucl. Instrum. Meth. A*, volume 482(1-2):pp. 457–474, 2002.

[BRM09] Bottcher, M.; Reimer, A.; Marscher, A.P.: Implications of the very high energy gamma-ray detection of the quasar 3C279. In: *Astrophys. J.*, volume 703(1):pp. 1168–1175, 2009.

[BS87] Biermann, P.L.; Strittmatter, P.A.: Synchrotron emission from shock waves in active galactic nuclei. In: *Astrophys. J.*, volume 322:pp. 643–649, 1987.

[BS00] Bhattacharjee, P.; Sigl, G.: Origin and propagation of extremely high-energy cosmic rays. In: *Physics Reports*, volume 327(3-4):pp. 109–247, 2000.

[C+03] Chekanov, S.; et al. (ZEUS): ZEUS next-to-leading-order QCD analysis of data on deep inelastic scattering. In: *Phys. Rev. D*, volume 67(1):p. 012007, 2003.

[CBHdlH03] Conrad, J.; Botner, O.; Hallgren, A.; de los Heros, C.P.: Including systematic uncertainties in confidence interval construction for Poisson statistics. In: *Phys. Rev. D*, volume 67:p. 012002, 2003.

[CH08] Cuoco, A.; Hannestad, S.: Ultrahigh energy neutrinos from Centaurus A and the Auger hot spot. In: *Phys. Rev. D*, volume 78(2):023007, 2008.

[Chi08] Chirkin, D.: Neutrino search with icecube, 2008. IceCube Internal Report, icecube/200807006, URL `http://internal.icecube.wisc.edu/reports/`.

[Chi09] Chirkin, D.: Measurement of the atmospheric neutrino energy spectrum with IceCube. In: *Proc. of the 31st ICRC, Łódź, Poland*. 2009.

[Cip08] Ciprini, S.: GLAST LAT detection of a possible new gamma-ray flaring blazar: PKS 1502+106. In: *The Astronomer's Telegram*, volume 1650:p. 1, 2008.

[Cow02] Cowan, G.: A survey of unfolding methods for particle physics. In: M.R.Whalley; L.Lyons, editors, *Proc. Conf. on Advanced Statistical Techniques in Particle Physics*, p. 248. Durham, 2002.

[CR04] Chirkin, D.; Rhode, W.: Muon Monte Carlo: A high-precision tool for muon propagation through matter, 2004. `arXiv:hep-ph/0407075`.

[CSS08] Cooper-Sarkar, A.; Sarkar, S.: Predictions for high energy neutrino cross-sections from the ZEUS global PDF fits. In: *JHEP*, volume 01:p. 075, 2008. `arXiv:07105.303[hep-ph]`.

[D'A95] D'Agostini, G.: A multidimensional unfolding method based on Bayes' theorem. In: *Nucl. Instrum. Meth. Phys. A*, volume 362(2-3):pp. 487–498, 1995.

[DGST05] Dolag, K.; Grasso, D.; Springel, V.; Tkachev, I.: Constrained simulations of the magnetic field in the local universe and the propagation of UHECRs. In: *JCAP*, volume 0501:p. 009, 2005. `arXiv:astro-ph/0410419`.

[DRSS01] Dutta, S.I.; Reno, M.H.; Sarcevic, I.; Seckel, D.: Propagation of muons and taus at high energies. In: *Phys. Rev. D*, volume 63:p. 094020, 2001. `arXiv:hep-ph/0012350`.

[F+09] Franckowiak, A.; et al.: Optical follow-up of high-energy neutrinos detected by IceCube. In: *Proc. of the 31st ICRC, Łódź, Poland*. 2009. `arXiv:0909.0631[astro-ph]`.

[FB09] Franke, R.; Bernardini, E. (IceCube): Neutrino triggered high-energy gamma-ray follow-up with IceCube. In: , 2009.

[FC98] Feldman, G.J.; Cousins, R.D.: Unified approach to the classical statistical analysis of small signals. In: *Phys. Rev. D*, volume 57(7):pp. 3873–3889, 1998.

[Fer49] Fermi, E.: On the origin of the cosmic radiation. In: *Phys. Rev.*, volume 75(8):pp. 1169–1174, 1949.

[Fer05] Ferenc, D.: The MAGIC gamma-ray observatory. In: *Nucl. Instrum. Meth. A*, volume 553(1-2):pp. 274–281, 2005. Proc. of the 5th International Workshop on Ring Imaging Detectors.

[FGLS94] Fletcher, R.S.; Gaisser, T.K.; Lipari, P.; Stanev, T.: Sibyll: An event generator for simulation of high energy cosmic ray cascades. In: *Phys. Rev. D*, volume 50:pp. 5710–5731, 1994.

[FGLS99] Fletcher, R.S.; Gaisser, T.K.; Lipari, P.; Stanev, T.: Air shower calculations with the new version of SIBYLL. In: *Proc. of the 26th ICRC, Salt Lake City, USA*, volume 1, p. 415. 1999.

[FLBA07] Franke, R.; Lauer, R.J.; Bernardini, E.; Ackermann, M.: Point source analysis for cosmic neutrinos beyond PeV energies with AMANDA and IceCube. In: *Proc. of the 30th ICRC, Mérida, Mexico*. Universidad Nacional Autónoma de México, Mexico City, 2007. `arXiv:0711.0353[astro-ph]`.

[FMC$^+$98] Fossati, G.; Maraschi, L.; Celotti, A.; Comastri, A.; Ghisellini, G.: A Unifying View of the Spectral Energy Distributions of Blazars. In: *Mon. Not. Roy. Astron. Soc.*, volume 299:pp. 433–448, 1998. `arXiv:astro-ph/9804103`.

[FNV01] Fiorentini, G.; Naumov, V.A.; Villante, F.L.: Atmospheric neutrino flux supported by recent muon experiments. In: *Phys. Lett. B*, volume 510:pp. 173–188, 2001. `arXiv:hep-ph/0103322`.

[Fra07] Franke, R.: A new approach to the search for point-like sources of cosmic neutrinos at PeV energies with AMANDA-II, 2007. Diplomarbeit, Humboldt-Universität zu Berlin.

[G$^+$07] Grullon, S.; et al.: Reconstruction of high energy muon events in IceCube using waveforms. In: *Proc. of the 30th ICRC, Mérida, Mexico*. Universidad Nacional Autónoma de México, Mexico City, 2007. `arXiv:0711.0353[astro-ph]`.

[G$^+$09] Gorham, P.W.; et al.: New Limits on the Ultrahigh Energy Cosmic Neutrino Flux from the ANITA Experiment. In: *Phys. Rev. Lett.*, volume 103(5):p. 051103, 2009. `arXiv:0812.2715[astro-ph]`.

[Gai90] Gaisser, T.K.: *Cosmic Rays and Particle Physics*. Cambridge University Press, Cambridge, 1990.

[Gai07] Gaisser, T.K.: Atmospheric neutrinos. In: *AIP Conf. Proc.*, volume 944:pp. 140–142, 2007. `arXiv:astro-ph/0612274`.

[GCF$^+$98] Ghisellini, G.; Celotti, A.; Fossati, G.; Maraschi, L.; Comastri, A.: A theoretical unifying scheme for gamma-ray bright blazars. In: *Mon. Not. Roy. Astron. Soc.*, volume 301:p. 451, 1998. `arXiv:astro-ph/9807317`.

[GGMR06] Gonzalez-Garcia, M.C.; Maltoni, M.; Rojo, J.: Determination of the atmospheric neutrino fluxes from atmospheric neutrino data. In: *JHEP*, volume 10:p. 075, 2006. `arXiv:hep-ph/0607324`.

[GGV03] Gelmini, G.; Gondolo, P.; Varieschi, G.: Measuring the prompt atmospheric neutrino flux with down-going muons in neutrino telescopes. In: *Phys. Rev. D*, volume 67(1):p. 017301, 2003.

[Gla60] Glashow, S.L.: Resonant scattering of antineutrinos. In: *Phys. Rev.*, volume 118(1):pp. 316–317, 1960.

[GP69] Gribov, V.N.; Pontecorvo, B.: Neutrino astronomy and lepton charge. In: *Phys. Lett. B*, volume 28:p. 493, 1969.

[GQRS96] Gandhi, R.; Quigg, C.; Reno, M.H.; Sarcevic, I.: Ultrahigh-energy neutrino interactions. In: *Astropart. Phys.*, volume 5:pp. 81–110, 1996. `arXiv:hep-ph/9512364`.

[GQRS98] Gandhi, R.; Quigg, C.; Reno, M.H.; Sarcevic, I.: Neutrino interactions at ultrahigh-energies. In: *Phys. Rev. D*, volume 58:p. 093009, 1998. `arXiv:hep-ph/9807264`.

[Gre66] Greisen, K.: End to the cosmic ray spectrum? In: *Phys. Rev. Lett.*, volume 16:pp. 748–750, 1966.

[GS64] Ginzburg, V.L.; Syrovatskii, S.I.: *The Origin of Cosmic Rays.* Pergamon, London and New York, 1964.

[H+99] Hartman, R.C.; et al.: The Third EGRET Catalog of High-Energy Gamma-Ray Sources. In: *Astrophys. J. Suppl.*, volume 123(1):pp. 79–202, 1999.

[H+09] Hague, J.D.; et al.: Correlation of the Highest Energy Cosmic Rays with Nearby Extragalactic Objects in Pierre Auger Observatory Data. In: *Proc. of the 31st ICRC, Łódź, Poland.* 2009.

[Hau04] Hauschildt, T.: *Search for cosmic point sources of high energy neutrinos with the AMANDA-II detector* . Ph.D. thesis, Humboldt-Universität zu Berlin, 2004.

[Hes12] Hess, V.F.: Über Beobachtungen der durchdringenden Strahlung bei sieben Freiballonfahrten. In: *Phys. Zeitschr.*, volume 13:p. 1084, 1912.

[HH02] Halzen, F.; Hooper, D.: High-energy neutrino astronomy: The cosmic ray connection. In: *Rept. Prog. Phys.*, volume 65:pp. 1025–1078, 2002. `arXiv:astro-ph/0204527`.

[HH03] Halzen, F.; Hooper, D.: Gamma ray astronomy with IceCube. In: *Journal of Cosmology and Astroparticle Physics*, volume 0308:p. 006, 2003.

[Hil84] Hillas, A.M.: The Origin of Ultrahigh-Energy Cosmic Rays. In: *Ann. Rev. Astron. Astrophys.*, volume 22:pp. 425–444, 1984.

[Hin04] Hinton, J.A.: The status of the HESS project. In: *New Astronomy Reviews*, volume 48(5-6):pp. 331–337, 2004. 2nd VERITAS Symposium on the Astrophysics of Extragalactic Sources.

[HKC+98] Heck, D.; Knapp, J.; Capdevielle, J.N.; Schatz, G.; Thouw, T.: CORSIKA: A Monte Carlo code to simulate extensive air showers. FZKA 6019, 1998. URL `http://www-ik.fzk.de/corsika/physics_description/corsika_phys.html`.

[HKK+07] Honda, M.; Kajita, T.; Kasahara, K.; Midorikawa, S.; Sanuki, T.: Calculation of atmospheric neutrino flux using the interaction model calibrated with atmospheric muon data. In: *Phys. Rev. D*, volume 75:p. 043006, 2007. `arXiv:astro-ph/0611418`.

[Hoe04] Hoerandel, J.R.: Models of the knee in the energy spectrum of cosmic rays. In: *Astropart. Phys.*, volume 21:pp. 241–265, 2004. `arXiv:astro-ph/0402356`.

[HRH09] Harris, G.L.H.; Rejkuba, M.; Harris, W.E.: The distance to NGC 5128 (Centaurus A), 2009. `arXiv:0911.3180[astro-ph]`.

[HRR03] Haungs, A.; Rebel, H.; Roth, M.: Energy spectrum and mass composition of high-energy cosmic rays. In: *Reports on Progress in Physics*, volume 66(7):pp. 1145–1206, 2003.

[HS98] Halzen, F.; Saltzberg, D.: Tau neutrino appearance with a 1000 Megaparsec baseline. In: *Phys. Rev. Lett.*, volume 81(20):pp. 4305–4308, 1998.

[Ish09] Ishihara, A.: Study of very bright cosmic-ray induced muon bundle signatures measured by the IceCube detector. In: *Proc. of the 31st ICRC, Łódź, Poland.* 2009.

[J+94] James, F.; et al.: Minuit. CERN Program Library entry D506, 1994. URL `http://lcgapp.cern.ch/project/cls/work-packages/mathlibs/minuit/`.

[Jac96] Jackson, J.D.: *Classical Electrodynamics.* Wiley, New York, USA, 1996.

[Jam89] James, D.E., editor: *The Encyclopedia of Solid Earth Geophysics.* Van Nostrand Reinhold, New York, 1989. Parameters of the Preliminary Reference Earth Model are given by Adam Dziewonski in "Earth Structure, Global".

[JR05] Japaridze, G.; Ribordy, M.: Realistic arrival time distribution from an isotropic light source, 2005. `arXiv:astro-ph/0506136`.

[K$^+$06] Kravchenko, I.; et al.: RICE limits on the diffuse ultrahigh energy neutrino flux. In: *Phys. Rev. D*, volume 73(8):p. 082002, 2006. `arXiv:astro-ph/0601148`.

[K$^+$07] Kiryluk, J.; et al.: IceCube performance with artificial light sources: The road to cascade analyses. In: *Proc. of the 30th ICRC, Mérida, Yucatan, Mexico.* Universidad Nacional Autónoma de México, Mexico City, 2007. `arXiv:0711.0353[astro-ph]`.

[KA03] Kowalski, M.; Askhat, G.: High energy neutrino generator for neutrino telescopes. In: *Proc. of the 28th ICRC, Tsukba, Japan.* 2003.

[KE86] Kazanas, D.; Ellison, D.C.: The central engine of quasars and active galactic nuclei Hadronic interactions of shock-accelerated relativistic protons. In: *Astrophys. J.*, volume 304:pp. 178–187, 1986.

[Kir99] Kirk, J.T.O.: Multiple scattering of a photon flux: Implications for the integral average cosine of the underwater light field. In: *Appl. Opt.*, volume 38(15):pp. 3134–3140, 1999.

[KOT09] Kachelriess, M.; Ostapchenko, S.; Tomas, R.: High energy radiation from Centaurus A. In: *New Journal of Physics*, volume 11(6), 2009.

[KST06] Kachelriess, M.; Serpico, P.D.; Teshima, M.: The Galactic magnetic field as spectrograph for ultra-high energy cosmic rays. In: *Astropart. Phys.*, volume 26:pp. 378–386, 2006. `arXiv:astro-ph/0510444`.

[KW05] Kashti, T.; Waxman, E.: Flavoring astrophysical neutrinos: Flavor ratios depend on energy. In: *Phys. Rev. Lett.*, volume 95:p. 181101, 2005. `arXiv:astro-ph/0507599`.

[L$^+$07] Lundberg, J.; et al.: Light tracking for glaciers and oceans: Scattering and absorption in heterogeneous media with photonics. In: *Nucl. Instrum. Meth. A*, volume 581:pp. 619–631, 2007. `arXiv:astro-ph/0702108`.

[L$^+$08] Larionov, V.M.; et al.: Results of WEBT, VLBA and RXTE monitoring of 3C 279 during 2006-2007. In: *Astron. Astrophys.*, volume 492:pp. 389–400, 2008.

[LC83] Lagage, P.O.; Cesarsky, C.J.: Cosmic-ray shock acceleration in the presence of self-excited waves. In: *Astron. Astrophys.*, volume 118:p. 223, 1983.

[LHK$^+$97] Lai, H.L.; Huston, J.; Kuhlmann, S.; Olness, F.; Owens, J.; Soper, D.; Tung, W.K.; Weerts, H.: Improved parton distributions from global analysis of recent deep inelastic scattering and inclusive jet data. In: *Phys. Rev. D*, volume 55(3):pp. 1280–1296, 1997.

[LM00] Learned, J.G.; Mannheim, K.: High-energy neutrino astrophysics. In: *Ann. Rev. Nucl. Part. Sci.*, volume 50(1):pp. 679–749, 2000.

[LP95] Learned, J.G.; P., Sandip: Detecting nu-tau oscillations at PeV energies. In: *Astropart. Phys.*, volume 3(3):pp. 267–274, 1995.

[LS00] Lunardini, C.; Smirnov, A.Y.: The minimum width condition for neutrino conversion in matter. In: *Nucl. Phys. B*, volume 583:pp. 260–290, 2000. `arXiv:hep-ph/0002152`.

[M$^+$00] Mereghetti, S.; et al. (AGILE): The AGILE gamma-ray satellite. In: Giovannelli, F.; Mannocchi, G., editors, *Frontier objects in astrophysics and particle physics, Vulcano Workshop*, p. 531. Italian Physical Society, 2000.

[M$^+$08] Migneco, E.; et al.: Recent achievements of the NEMO project. In: *Nucl. Instrum. Meth. A*, volume 588:pp. 111–118, 2008.

[Mah09] Mahlstedt, J.: Multi-messenger studies of neutrinos observed by icecube and charged cosmic rays at highest energies, 2009. Summer student report, URL `http://www.ifh.de/summerstudents/talks/2009/reports/Mahlstedt.pdf`.

[Man97] Mannheim, K.: AGN models: High-energy emission, 1997. `arXiv:astro-ph/9703184`.

[Mar08] Marelli, M.: Fermi LAT detection of a possible new gamma-ray flaring blazar: PKS 1454-354. In: *The Astronomer's Telegram*, volume 1701:p. 1, 2008.

[McD04] McDonald, A.B.: Solar neutrino measurements. In: *New J. Phys.*, volume 6:p. 121, 2004. `arXiv:astro-ph/0406253`.

[Mir07] Mirabel, I.F.: Gamma-ray binaries. In: *Astrophys. Space Sci.*, volume 309:pp. 267–270, 2007. `arXiv:astro-ph/0610707`.

[MNS62] Maki, Z.; Nakagawa, M.; Sakata, S.: Remarks on the unified model of elementary particles. In: *Prog. Theor. Phys.*, volume 28:pp. 870–880, 1962.

[Mon99] Montaruli, T. (NEMO): Capabilities of an underwater detector as a neutrino telescope and for the neutrino oscillation search. In: , 1999. `arXiv:hep-ex/9905019`.

[MP01] Mücke, A.; Protheroe, R.J.: A proton synchrotron blazar model for flaring in Markarian 501. In: *Astropart. Phys.*, volume 15:pp. 121–136, 2001. `arXiv:astro-ph/0004052`.

[MPE$^+$03] Mücke, A.; Protheroe, R.J.; Engel, R.; Rachen, J.P.; Stanev, T.: BL Lac objects in the synchrotron proton blazar model. In: *Astropart. Phys.*, volume 18:pp. 593–613, 2003. `arXiv:astro-ph/0206164`.

[MSS$^+$04] McDonald, A.B.; Spiering, C.; Schönert, S.; Kearns, E.T.; Kajita, T.: Astrophysical neutrino telescopes. In: *Rev. Sci. Instrum.*, volume 75:pp. 293–316, 2004. `arXiv:astro-ph/0311343`.

[N$^+$07] Nandikotkur, G.; et al.: Does the Blazar gamma-ray spectrum harden with increasing flux? Analysis of 9 years of EGRET data. In: *Astrophys. J.*, volume 657(2):pp. 706–724, 2007.

[Neu03] Neunhöffer, T.: *Die Entwicklung eines neuen Verfahrens zur Suche nach kosmischen Neutrino-Punktquellen mit dem AMANDA-Neutrinoteleskop.* Ph.D. thesis, Johannes Gutenberg Universität, Mainz, 2003.

[Neu06] Neunhöffer, T.: Estimating the angular resolution of tracks in neutrino telescopes based on a likelihood analysis. In: *Astropart. Phys.*, volume 25(3):pp. 220–225, 2006.

[NK06] Neunhöffer, T.; Köpke, L.: Searching for localized cosmic particle sources with an unbinned maximum likelihood approach. In: *Nucl. Instrum. Meth. A*, volume 558(2):pp. 561–568, 2006.

[NMB93] Nellen, L.; Mannheim, K.; Biermann, P.L.: Neutrino production through hadronic cascades in AGN accretion disks. In: *Phys. Rev. D*, volume 47(12):pp. 5270–5274, 1993.

[NS02] Neronov, A.Y.; Semikoz, D.V.: Which blazars are neutrino loud? In: *Phys. Rev. D*, volume 66(12):p. 123003, 2002.

[NSAK02] Neronov, A.; Semikoz, D.; Aharonian, F.; Kalashev, O.: Large-scale extragalactic jets powered by very-high-energy gamma rays. In: *Phys. Rev. Lett.*, volume 89(5):p. 051101, 2002.

[P$^+$02] Pumplin, J.; et al.: New generation of parton distributions with uncertainties from global QCD analysis. In: *JHEP*, volume 07:p. 012, 2002. `arXiv:hep-ph/0201195`.

[Pan96] Pandel, D.: Bestimmung von Wasser- und Detektorparametern und Rekonstruktion von Myonen bis 100 TeV mit dem Baikal-Neutrinoteleskop NT-72, 1996. Diplomarbeit, Humboldt-Universität zu Berlin, URL `http://www-zeuthen.desy.de/nuastro/publications/diploma/`.

[PDR03] Protheroe, R.J.; Donea, A.C.; Reimer, A.: TeV gamma rays and cosmic rays from the nucleus of M87, a mis-aligned BL Lac object. In: *Astropart. Phys.*, volume 19:pp. 559–568, 2003. `arXiv:astro-ph/0210249`.

[Pet09] Petrovic, J.: Multimessenger search for point sources: Ultra-high energy cosmic rays and neutrinos, 2009. `arXiv:0908.1235[astro-ph]`.

[PG95] Padovani, P.; Giommi, P.: The Connection between X-ray- and Radio-Selected BL Lacertae Objects. In: *Astrophys. J.*, volume 444:p. 567, 1995. `arXiv:astro-ph/9412073`.

[Poi37] Poisson, S.D.: Recherches sur la probabilité des jugements en matière criminelle et matière civile. In: *Bachelier*, volume 55, 1837.

[PWC00] Price, P.B.; Woschnagg, K.; Chirkin, D.: Age vs depth of glacial ice at South Pole. In: *Geophysical Research Letters*, volume 27(14), 2000.

[RC01] Rhode, W.; Chirkin, D.: Muon Monte Carlo: a new high-precision tool for tracking of muons in medium. In: *Proc. of the 27th ICRC, Hamburg, Germany*, p. 1017. 2001.

[Rei09] Reimer, A.: Hadron-initiated emission processes in blazar jets. In: *Int. J. Mod. Phys. D*, volume 18(10):pp. 1511–1515, 2009.

[RMM07] Ritz, S.; Michelson, P.; Meegan, C., editors: *Proceedings of 1st GLAST Symposium.* AIP, New York, 2007.

[S$^+$09] Spurio, M.; et al. (ANTARES): ANTARES neutrino telescope: status, first results and sensitivity for the diffuse neutrino flux. In: *Int. J. Mod. Phys. D*, volume 18(10):pp. 1615–1619, 2009. `arXiv:0904.3836[astro-ph]`.

[SDSS91] Stecker, F.W.; Done, C.; Salamon, M.H.; Sommers, P.: High-energy neutrinos from active galactic nuclei. In: *Phys. Rev. Lett.*, volume 66(21):pp. 2697–2700, 1991.

[SL04] Schwanke, U.; Lohse, T.: Calculation of upper limits and measurement errors for small signals, 2004. URL `http://www-hess.physik.hu-berlin.de/public/limits.pdf`.

[Sta04] Stanev, T.: *High energy cosmic rays.* Springer, Berlin, 2004.

[Ste05] Stecker, F.W.: Note on high-energy neutrinos from active galactic nuclei cores. In: *Phys. Rev. D*, volume 72(10):p. 107301, 2005.

[STV08] Schwetz, T.; Tortola, M.A.; Valle, J.W.F.: Three-flavour neutrino oscillation update. In: *New J. Phys.*, volume 10:p. 113011, 2008. `arXiv:hep-ph/08082016`.

[T$^+$01] Tavani, M.; et al. (AGILE): Science with AGILE. In: Ritz, Steven; Gehrels, Neil; Shrader, Chris R., editors, *GAMMA 2001: Gamma-Ray Astrophysics 2001*, volume 587, pp. 729–738. AIP, 2001.

[TDK$^+$09] Tilav, S.; Desiati, P.; Kuwabara, T.; Rocco, D.; Rothmaier, F.; Simmons, M.; Wissing, H.: Atmospheric variations as observed by IceCube. In: *Proc. of the 31st ICRC, Łódź, Poland*. 2009.

[Thr09] Thrane, E.: Search for astrophysical neutrino point sources at Super-Kamiokande. In: *Astrophys. J.*, volume 704(1):pp. 503–512, 2009. `arXiv:0907.1594[astro-ph]`.

[TS09] Takami, H.; Sato, K.: Does galactic magnetic field disturb the correlation of the highest energy cosmic rays with their sources?, 2009. `arXiv:0909.1532[astro-ph]`.

[UP95] Urry, C.M.; Padovani, P.: Unified schemes for radio-loud Active Galactic Nuclei. In: *Publ. Astron. Soc. Pac.*, volume 107:p. 803, 1995. `arXiv:astro-ph/9506063`.

[VCV06] Véron-Cetty, M.-P.; Véron, P.: A catalogue of quasars and active nuclei: 12th edition. In: *Astron. Astrophys.*, volume 455(2):pp. 773–777, 2006.

[Voi08] Voigt, B.: *Sensitivity of the IceCube Detector for ultra-high energy electron-neutrino events*. Ph.D. thesis, Humboldt-Universität zu Berlin, 2008.

[Vol80] Volkova, L.V.: Energy spectra and angular distributions of atmospheric neutrinos. In: *Sov. J. Nucl. Phys.*, volume 31:pp. 784–790, 1980.

[W$^+$02] Weekes, T.C.; et al.: VERITAS: the Very Energetic Radiation Imaging Telescope Array System. In: *Astropart. Phys.*, volume 17(2):pp. 221–243, 2002.

[Wie95] Wiebusch, C.H.: *The detection of faint light in deep underwater neutrino telescopes*. Ph.D. thesis, RWTH Aachen, 1995.

[Wie09] Wiebusch, C.: Physics capabilities of the IceCube DeepCore Detector. In: *Proc. of the 31st ICRC, Łódź, Poland*. 2009. `arXiv:0907.2263[astro-ph]`.

[ZB02] Zier, C.; Biermann, P.L.: Binary black holes and tori in AGN II. Can stellar winds constitute a dusty torus? In: *Astron. Astrophys.*, volume 396:pp. 91–108, 2002. `arXiv:astro-ph/0203359`.

[ZC07] Zornoza, J.D.; Chirkin, D.: Muon energy reconstruction and atmospheric neutrino spectrum unfolding with the IceCube detector. In: *Proc. of the 30th ICRC, Mérida, Mexico*. Universidad Nacional Autónoma de México, Mexico City, 2007. `arXiv:0711.0353[astro-ph]`.

[ZK66] Zatsepin, G.T.; Kuzmin, V.A.: Upper limit of the spectrum of cosmic rays. In: *JETP Lett.*, volume 4:pp. 78–80, 1966.

# Danksagung

In erster Linie gilt mein Dank Dr. Elisa Bernardini für ihre Betreuung meiner Promotion. Seit unserem ersten Kontakt hat sie mich ermutigt, auf Neutrinojagd zu gehen, und mich dabei gefördert, meine Arbeit zu dem vorliegenden Ergebnis zu führen.

Ich möchte Prof. Dr. Hermann Kolanoski für seine hilfreiche Unterstützung und für die Begutachtung dieser Dissertation danken. Mein herzlicher Dank geht auch an Prof. Dr. Thomas K. Gaisser für die Übernahme des Gutachtens.

Bei Dr. Christian Spiering bedanke ich mich für die freundschaftliche Arbeitsatmosphäre und viele konkrete Hilfestellungen. Dr. Stefan Schlenstedt danke ich für wertvolle Kommentare und seine ansteckende Offenheit.

Mein spezieller Dank gilt Dr. Martin Tluczykont, ein exzellenter Lehrer bei meinem Einstieg in die Astroteilchenphysik. Er und die anderen *Smarties* Robert Franke, Konstancja Satalecka, José Luis Bazo Alba, Sirin Odrowski und Dr. Pratik Majumdar waren Garant für eine vergnügliche wie produktive Zusammenarbeit in der Nachwuchsgruppe. Auch Jörn Mahlstedt danke ich für seine exzellente Mitarbeit als Sommerstudent. Dr. Markus Ackermann möchte ich für die ursprüngliche Idee zum Thema dieser Dissertation danken.

Ausgesprochen dankbar bin ich Patrick, Gareth und Robert F. für adventliches Korrekturlesen. Mein Dank gilt vielen Mitgliedern der IceCube-Kollaboration hinsichtlich der lebendigen und motivierenden Kollaborationstreffen. Auch allen noch nicht genannten Kollegen, besonders Marek, Sebastian B., Stefan K., Bernhard, Oxana, Julien, Ralf, Mike, Rolf, Martin P., Jens, Lotfi, Andreas, Eike, Heike, Adam, Martin B., Achim, Thomas, Anna F., Anna M., Tilo, Fabian, Delia, Sebastian P., ..., danke ich von Herzen für die unvergessliche Zeit in Zeuthen, Berlin und auf Reisen, für tiefgehende wie verrückte Diskussionen, für Programmiertipps, Feierabendaktivitäten und viel leckeren Kuchen.

Ich möchte insbesondere auch meinen Nicht-Physiker-Freunden, gerade einigen der Gen, danken, die mir wiederholt durch interessiertes Fragen und Zuhören meine eigene Begeisterung für die Astroteilchenphysik neu bewusst gemacht haben.

Zuletzt gilt mein Dank meiner Familie und besonders meinen Eltern für den liebevollen und fortwährenden Rückhalt.

# Selbständigkeitserklärung

Hiermit erkläre ich, die vorliegende Arbeit selbständig und nur unter Verwendung der angegebenen Literatur und Hilfsmittel erstellt zu haben.

Berlin, den 15.01.2010

Robert J. Lauer